Modeling, and Classical and Advanced Control of a Solid Rocket Motor Thrust Vector Control System

by

Jackson H. Jung

Submitted to the Department of Electrical Engineering and Computer Science
in partial fulfillment of the requirements for the degrees of

Master of Science

and

Bachelor of Science

at the

MASSACHUSETTS INSTITUTE OF TECHNOLOGY

June 1993

Author .....
Department of Electrical Engineering and Computer Science
December 15, 1992

Certified by .....
George C. Verghese
Professor of Electrical Engineering
Thesis Supervisor

Certified by .....
Joseph A. Dworak
Manager, Control Sensors and Electronics, The Aerospace Corporation
Thesis Supervisor

Accepted by ....
Leonard A. Gould
Chairman, Departmental Committee on Graduate Students

Modeling, and Classical and Advanced Control of a Solid Rocket Motor Thrust Vector Control System

by

Jackson H. Jung

Submitted to the Department of Electrical Engineering and Computer Science
on December 15, 1992, in partial fulfillment of the
requirements for the degrees of
Master of Science
and
Bachelor of Science

Abstract

This thesis is a study of the modeling and design of a solid rocket motor Thrust Vector Control (TVC) system. The TVC system is an electrohydraulic servomechanism which gimbals the nozzle at the end of a solid rocket motor in order to steer the vehicle. The thesis is really a composite of three related TVC topics: (1) The construction of a math model and simulation for the TVC system. The simulation is benchmarked against actual test data from hardware at Edwards Air Force Base, CA. The complex eighth-order nonlinear model of the hydraulics and external system torques closely predicts the behavior of the hardware in most cases. (2) The development of appropriate linearizing approximations to facilitate classical control analysis. Transfer functions are derived, and Bode analysis of the current controller design is presented. The linearized inner or pressure feedback loop has approximately 9 dB of gain margin and 50 degrees of phase margin. The linearized outer or position loop has approximately 7 dB of gain margin and 48 degrees of phase margin. Because some significant nonlinearities are neglected in the linearization, the linearized model has about 7 Hz more bandwidth than the nonlinear model. (3) The design of a nonlinear controller using *feedback linearization* and pole placement techniques. The nonlinear controller offers improved performance at the cost of increased complexity. It is more efficient in reaching its final state than is the classical controller. However, it does not handle the highly nonlinear external torques well. Small steady state errors can result unless the controller is provided with additional information about the external torques.

Thesis Supervisor: George C. Verghese

Title: Professor of Electrical Engineering

Acknowledgments

The author wishes to thank Joe Dworak for his patience and support, as well as Tom Kazangey, Marilyn Hansen, Ray Skrinska, and Roger Thelander, all of The Aerospace Corporation. Thanks also to Prof. George Verghese of MIT. This thesis is long overdue, and I am sure all of you were starting to wonder.

Contents

List of Figures

Chapter 1

Introduction

This thesis is a study of the modeling and design of a solid rocket motor Thrust Vector Control (TVC) system. The TVC system is an electrohydraulic servomechanism which gimbals the nozzle at the end of a solid rocket motor in order to steer the vehicle. The thesis is really a composite of three related TVC topics: (1) The construction of a math model and simulation for the TVC system is the subject of the second chapter. The simulation is benchmarked against actual test data from hardware at Edwards Air Force Base, CA. The nonlinear simulation was implemented both on an IBM compatible DOS personal computer using ACSL [48], and on a VMS Digital VAX using MATRIX-X [49]. (2) The development of appropriate linearizing approximations to facilitate classical controller design is the topic of the third chapter. Transfer functions are derived, and Bode analysis of the current controller design is presented. The linear analysis was performed on an X-Windows SUN Workstation using Matlab [50].(3) The design of a nonlinear controller using feedback linearization and pole placement techniques is shown in the fourth chapter. The nonlinear controller has the potential for offering improved performance at the cost of increased complexity. Results comparing the performance of the classical and nonlinear controllers are presented.

The thesis is divided into three main chapters, one for each topic. Within each chapter are sections discussing the modeling of the major components of the TVC system: nozzle torques, piston movement and pressure, fluid flow, supply pressure,

servovalve, and controller. The nonlinear math models of the second chapter contain the most detail. The models used in the analysis of the present classical controller, and in the development of the nonlinear controller are somewhat simplified.

Chapter 2

The Titan IV SRMU TVC System

The Titan IV Solid Rocket Motor Upgrade (SRMU) Thrust Vector Control (TVC) system is a dual electrohydraulic servomechanism which pivots the exhaust nozzle at the end of the SRMU in order to steer the vehicle [9, 13, 19, 12, 18]. See Figure 2-1. As shown in Figure 2-2, two actuators placed 90 degrees apart extend and retract hydraulically in order to point the exhaust in the desired direction. The actuators are placed along the tilt and rock directions. Nozzle gimbal commands are issued along the pitch and yaw directions; the coordinate transformation is performed by the control electronics. Four sensors, or Nozzle Position Transducers (NPT), placed around the nozzle measure the gimbal angle and provide feedback to the control electronics, or Loop Closure Unit (LCU). For increased sensitivity, gimbal angle measurement along a single axis requires the participation of two NPT's. As depicted in Figure 2-3, the nozzle sits and pivots on a compliant ring known as flexseal, and two 154 horsepower turbine/pump assemblies pressurize the hydraulic fluid.

The hydraulic circuit is depicted in Figure 2-4. The flow of pressurized fluid to each of the actuators is determined by an electrical current controlled servovalve. The polarity of the servovalve current determines which side of the piston the flow enters, thus controlling the extension and retraction of the actuator. The magnitude of the servovalve current determines the magnitude of the hydraulic flow. The current is input to three torque motors which position three hydraulic jet deflectors in order to position the servovalve spool, which is the hydraulic gate to the actuator chambers.

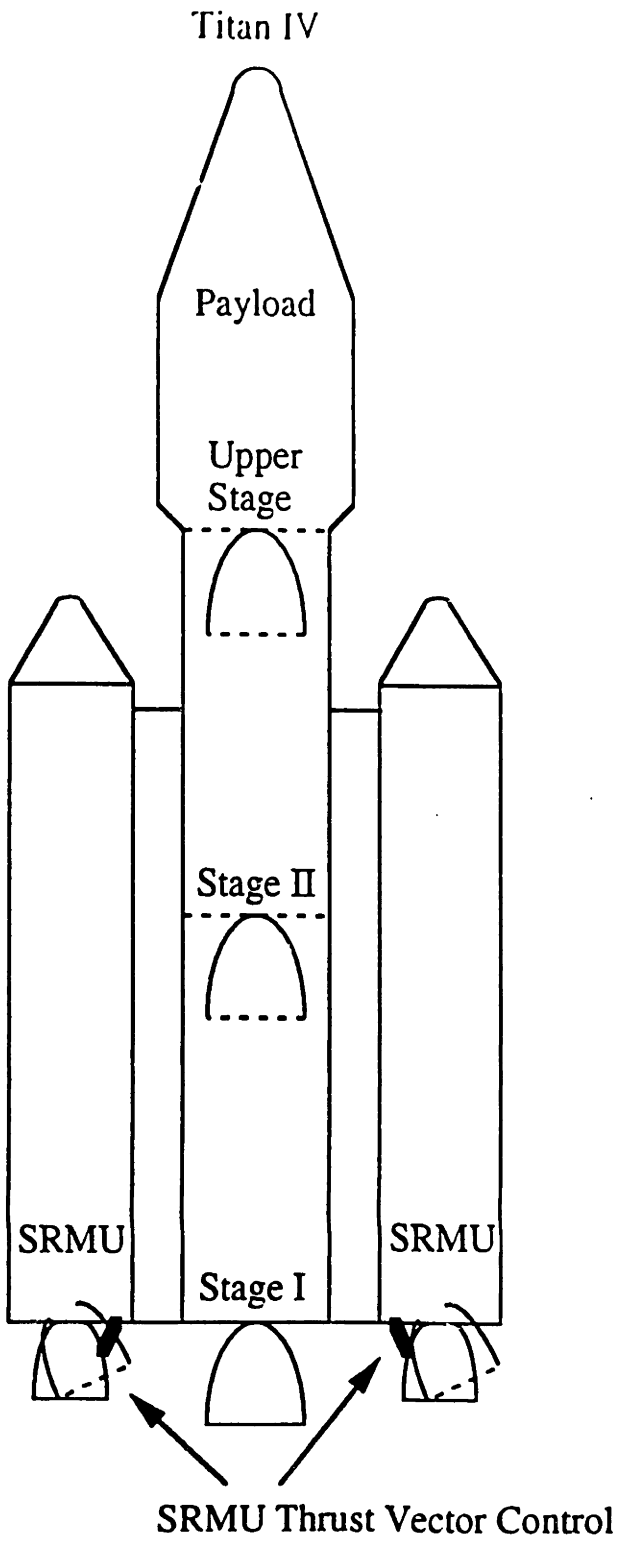

Figure 2-1: Titan IV Includes Core Vehicle with Two Upgraded Solid Rocket Motors (SRMU). Figure is Not Drawn to Scale.

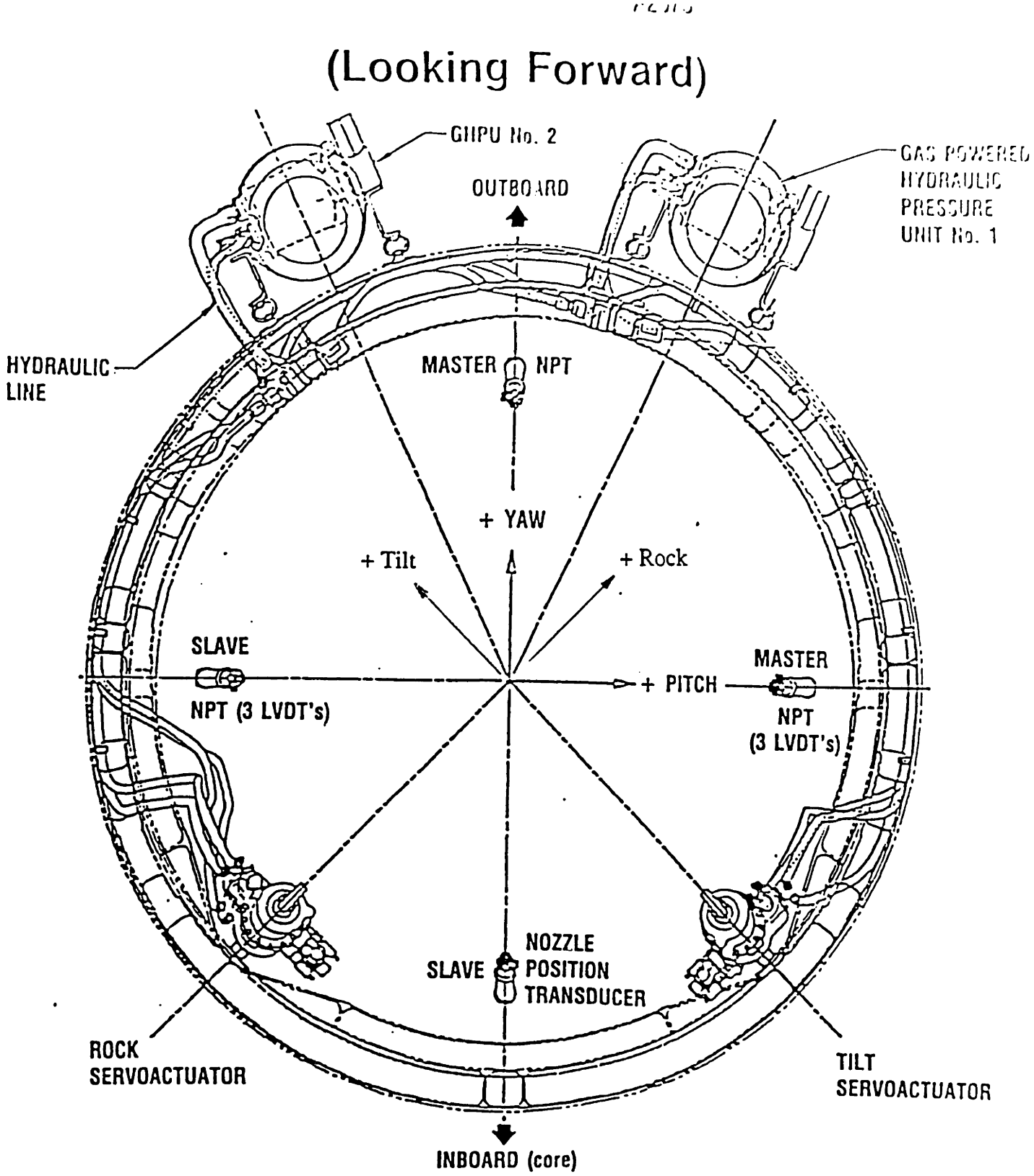

Figure 2-2: The Electrohydraulic Thrust Vector Control System (TVC) Includes Two Actuators Along the Tilt and Rock Directions.

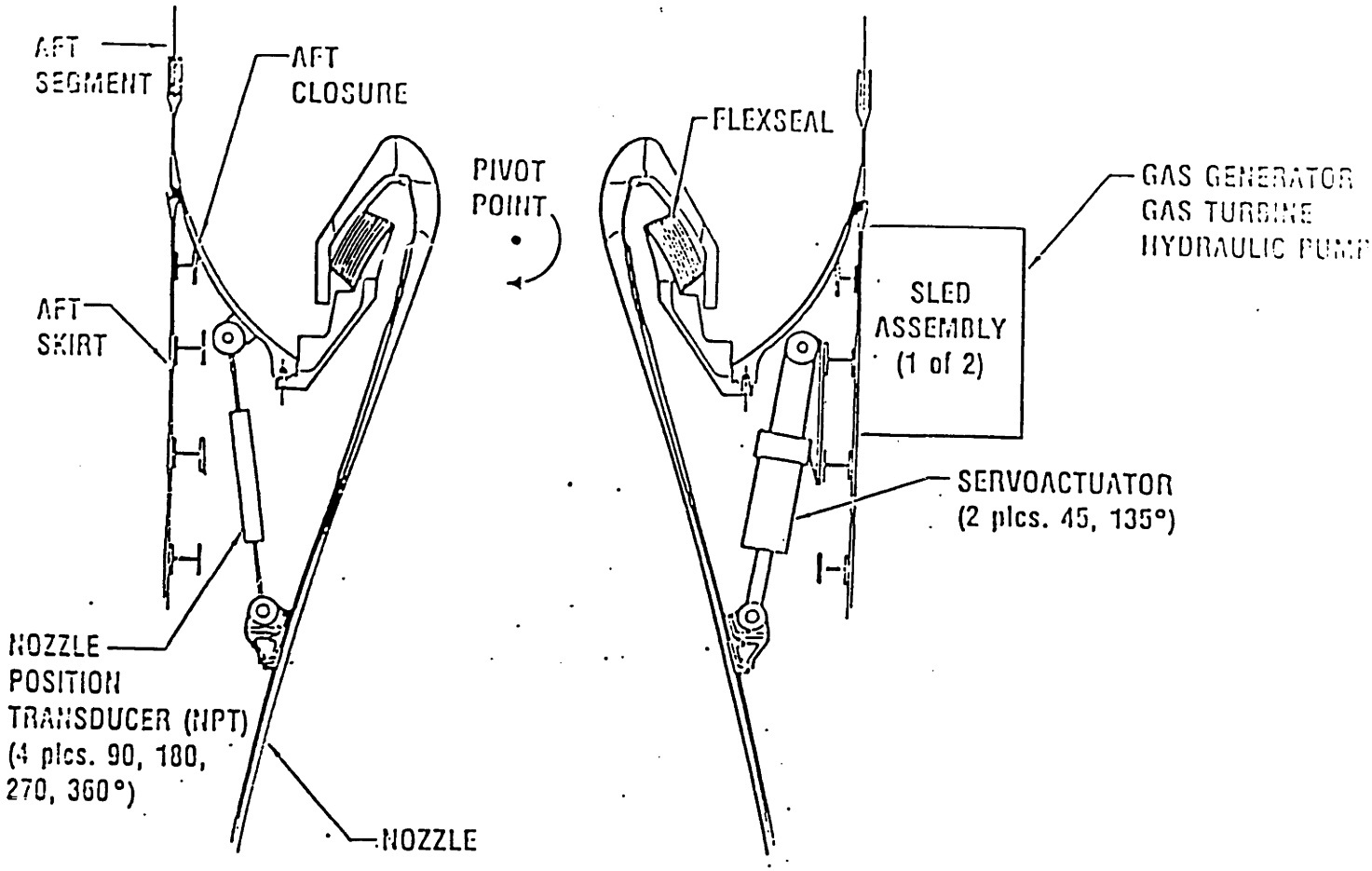

Figure 2-3: The Nozzle Sits and Pivots on a Compliant Ring Known As Flexseal. Two 154 Horsepower Turbine/Pump Assemblies Pressurize the Hydraulic Fluid.

A single torque motor/jet deflector combination can position the servovalve spool if necessary, but with degraded performance. Other examples of redundancy include three differential pressure transducers per actuator, three linear variable differential transformers (LVDT) per nozzle position transducer (NPT), and a pressure selector valve which allows one of the hydraulic pumps to power both actuators should the other fail.

From a control systems perspective, a single axis of the TVC system can be represented in a block diagram form as shown in Figure 2-5. The servovalve controls the flow of fluid to the actuator which positions the nozzle. Actuator differential pressure and nozzle angle are fed back to the analog electronic controller, or Loop Closure Unit (LCU), which includes compensation for low frequency system resonances.

This chapter describes the construction of a nonlinear model.

2.1 Nozzle Torques

The TVC system must counteract the following nozzle torques: internal aerotorque, external aerotorque, heat shield torque, and flexseal torque. The TVC system must accelerate the nozzle inertia quickly with minimal overshoot and a fast settling time.

$$T_a - \sum_{k=1}^{4} T_k = J\ddot{\theta} \tag{2.1}$$

T_1 = Internal Aerotorque

T_2 = External Aerotorque

T_3 = Heat Shield Torque

T_4 = Flexseal Torque

T_a = Hydraulic Actuator Torque

J = Nozzle Inertia

θ = Nozzle Angle

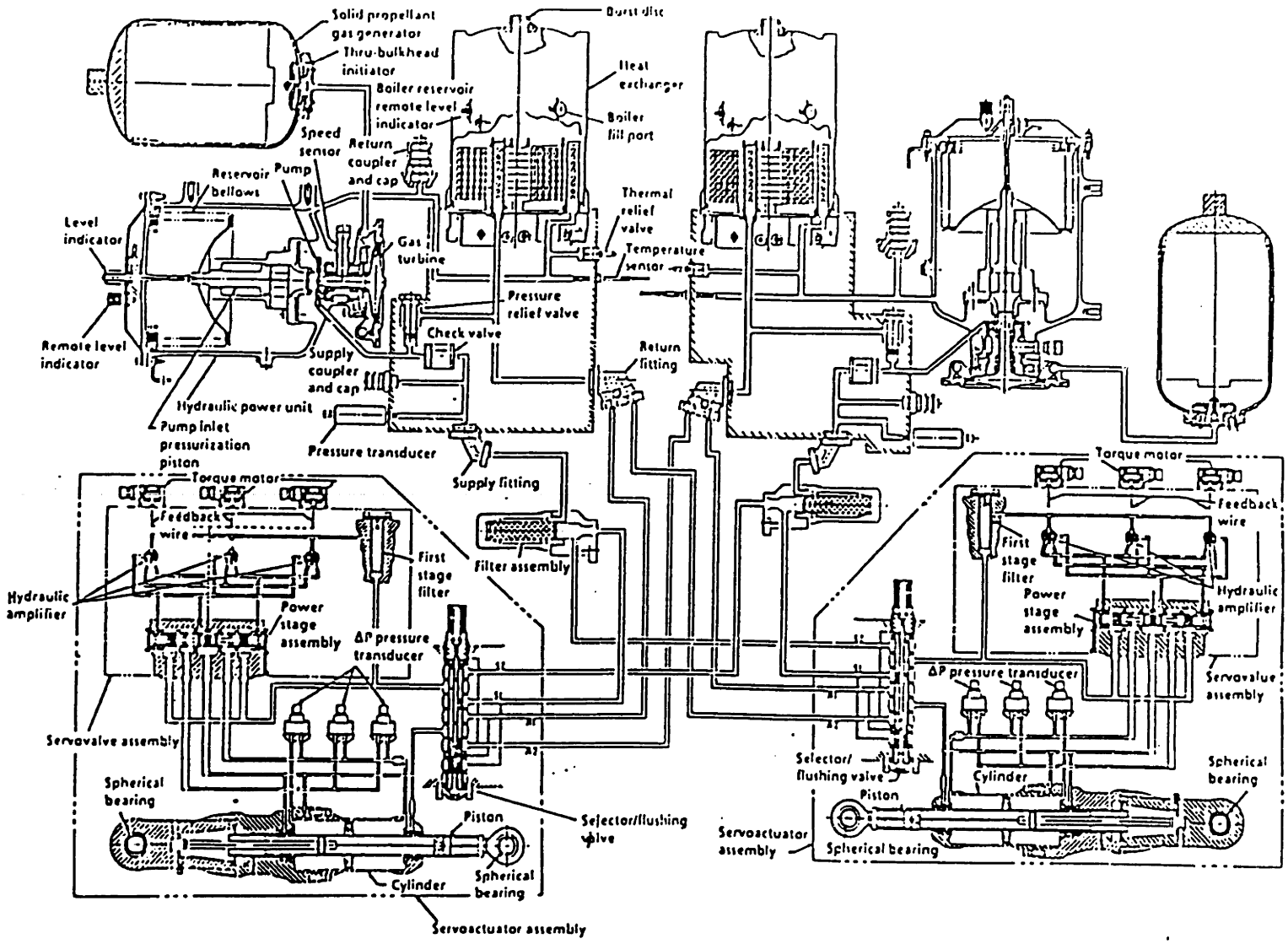

Figure 2-4: Schematic Diagram of TVC Hydraulic Circuit. Courtesy Moog Inc. [13]

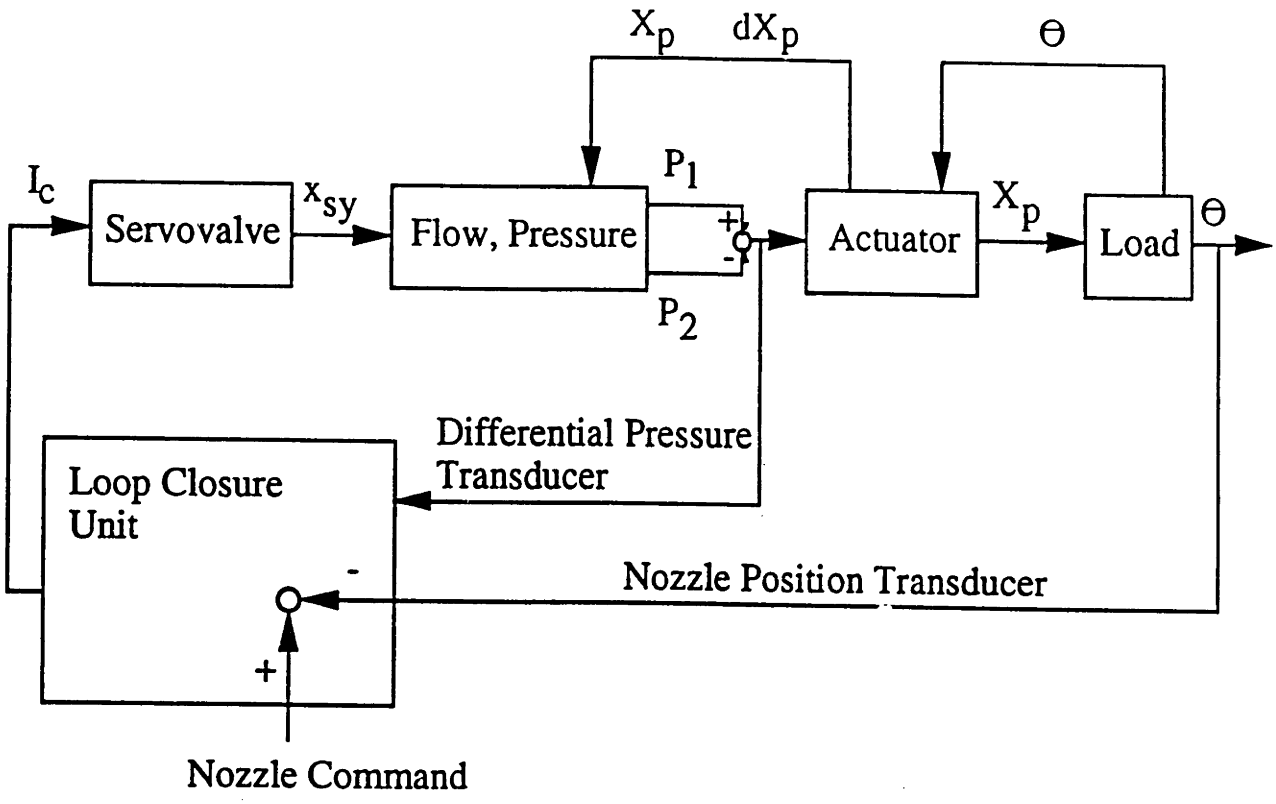

Figure 2-5: Block Diagram Representation of Single Axis of the TVC System

2.1.1 Internal Aerotorque

The internal aerotorque is the torque upon the nozzle due to exhaust flow turning. Its expected profile as a function of time is shown in Figure 2-6 [45, 9, 42]. During the first 56 seconds after ignition, the internal aerotorque is expected to change from approximately 183,300 in · lbs per degree of nozzle angle to about -38,000 in · lbs per degree of nozzle angle. In other words, the internal aerotorque is expected to start out as a centering torque opposing large nozzle gimbal angles, and then become an outward torque encouraging large nozzle gimbal angles. After 120 seconds, the internal aerotorque is expected to become negligible.

At ignition, various transient forces can be generated which will increase the internal aerotorque. One of these is due to asymmetric flow separation, which exists until the nozzle chamber to ambient pressure ratio rises to a value for which the nozzle flows full. The phenomenon is not well understood, but extremely large nozzle torques can be generated, and a considerable amount of engineering effort is involved in mitigating its effects. Early estimates of nozzle torque due to asymmetric flow separation were as high as 8 million in · lbs [23]. These estimates generated serious concerns about the ability of the nozzle structure to survive [21]. At present, for the SRMU, a peak moment of 3.6 million in · lbs from flow separation is believed possible [5]. Figure 2-7 shows that if it occurs, it is expected to be some randomly directed triangular torque pulse occurring 100 milliseconds (ms) after ignition, and lasting 100 ms.

2.1.2 External Aerotorque

The external aerotorque is the torque upon the nozzle of earth's atmosphere rushing by the vehicle [45, 9, 42]. While it is a function of many variables, for TVC modeling purposes, it is approximated as shown in Figure 2-8. The moment can be as high as 2.3 million in · lbs or as low as 52,000 in · lbs. It shifts between two boundaries of the nozzle angle versus nozzle moment plane, as a function of motor action time. The upper boundary is reached at 56 seconds. The external aerotorque characteristic

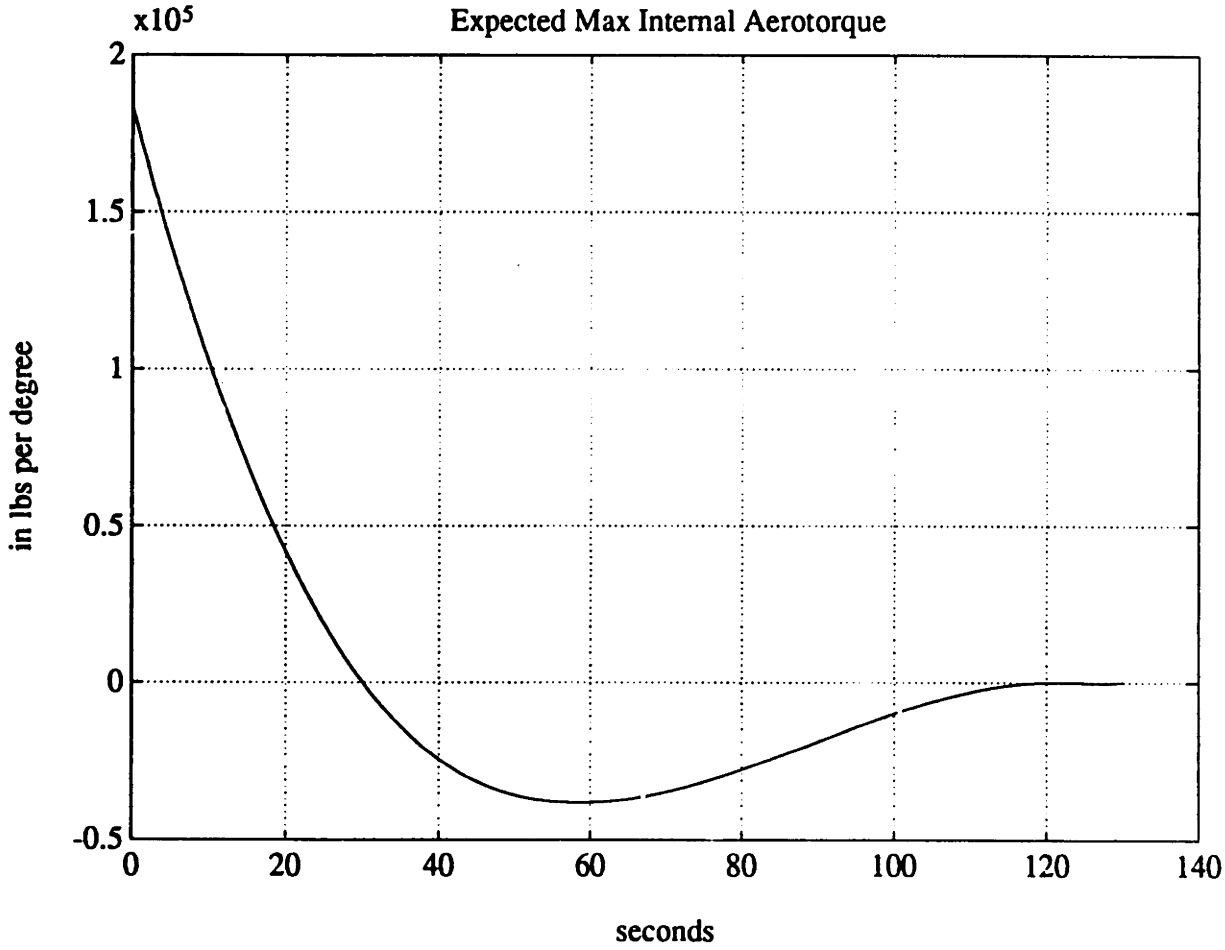

Figure 2-6: Expected Profile of Internal Aerotorque as a Function of Time [45, 9, 42]

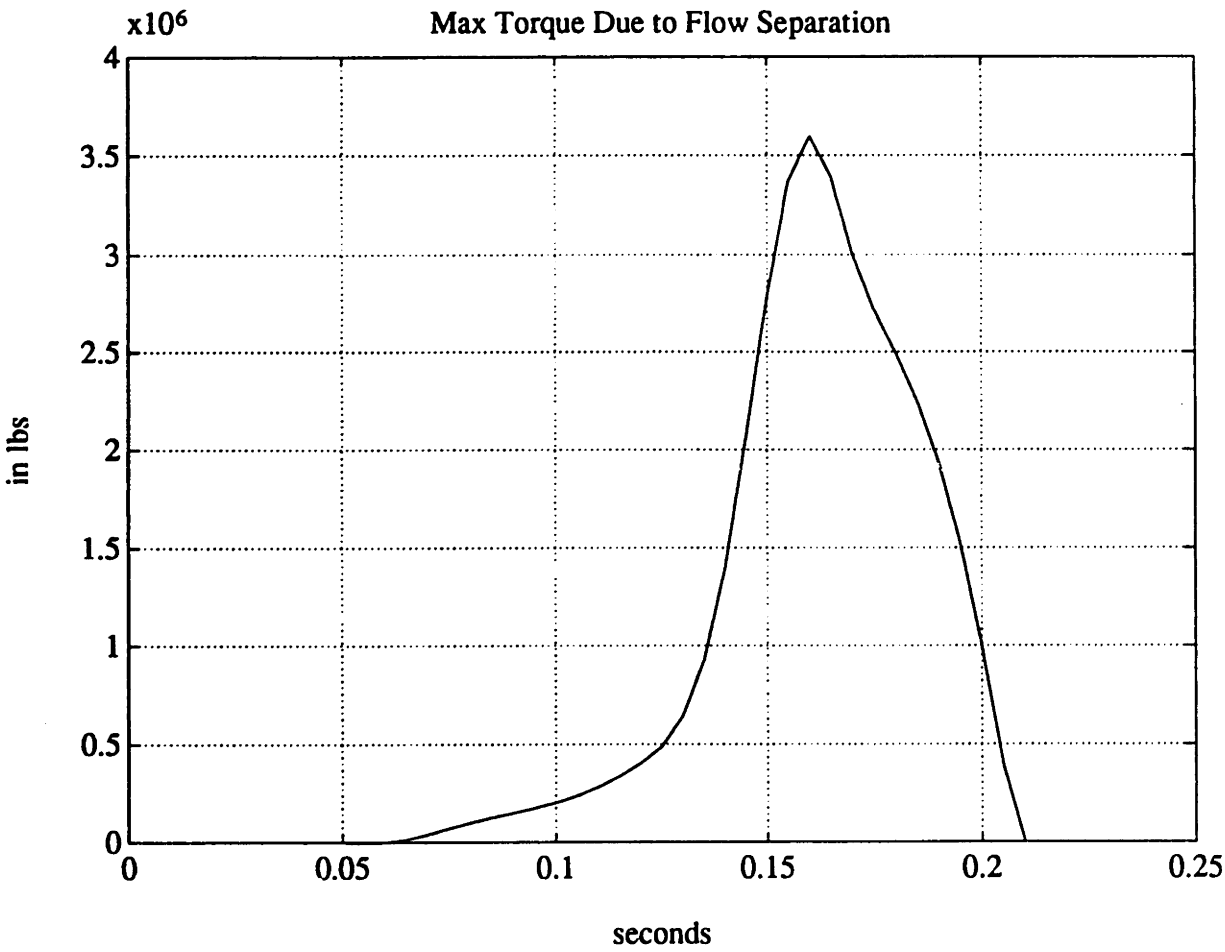

Figure 2-7: Triangular Torque Pulse Which Can Be Generated By Asymmetric Exhaust Flow Separation at Ignition [5]

begins at the lower boundary and returns there after 126 seconds. Note the external aerotorque is centering if the nozzle gimbal angle is positive, but is outward if the nozzle gimbal angle is negative. This imbalance is due to the aerodynamic shielding effect of the core vehicle between the two SRMU's.

2.1.3 Heat Shield Torque

The heat shield torque is created by a pressure differential between the areas separated by the shield. Figure 2-9 shows the torque reaching its peak of 119,600 in · lbs per degree of nozzle angle at 56 seconds of motor action time [29].

2.1.4 Flexseal Torque

The nozzle sits and pivots on a compliant ring known as flexseal. The flexseal torque includes a spring rate and a Dahl solid friction component [6]. The solid friction torque can reach a maximum of T_c in · lbs, and is a function of nozzle rate. It is described by the following first order nonlinear differential equation:

$$\frac{dT_h}{dt} = \frac{d\theta}{dt}\sigma\alpha_1(1 - \alpha_2\frac{T_h}{T_c})^2 \tag{2.2}$$

where:

$$\begin{aligned} \theta &= \text{Nozzle Angle} \\ T_h &= \text{Dahl Solid Friction Torque Component} \\ \sigma &= \text{Maximum Rate of Change} \\ T_c &= \text{Maximum Torque} \\ \alpha_2 &= \text{SIGN}(\tfrac{d\theta}{dt}) \\ \alpha_1 &= \text{SIGN}(1 - \alpha_2\tfrac{T_h}{T_c}) \end{aligned}$$

The total flexseal torque is described by the following equation, where K_s is the spring rate.

$$T_4 = T_h + K_s\theta \tag{2.3}$$

The flexseal spring rate decreases under the pressure of the rocket exhaust flow [44].

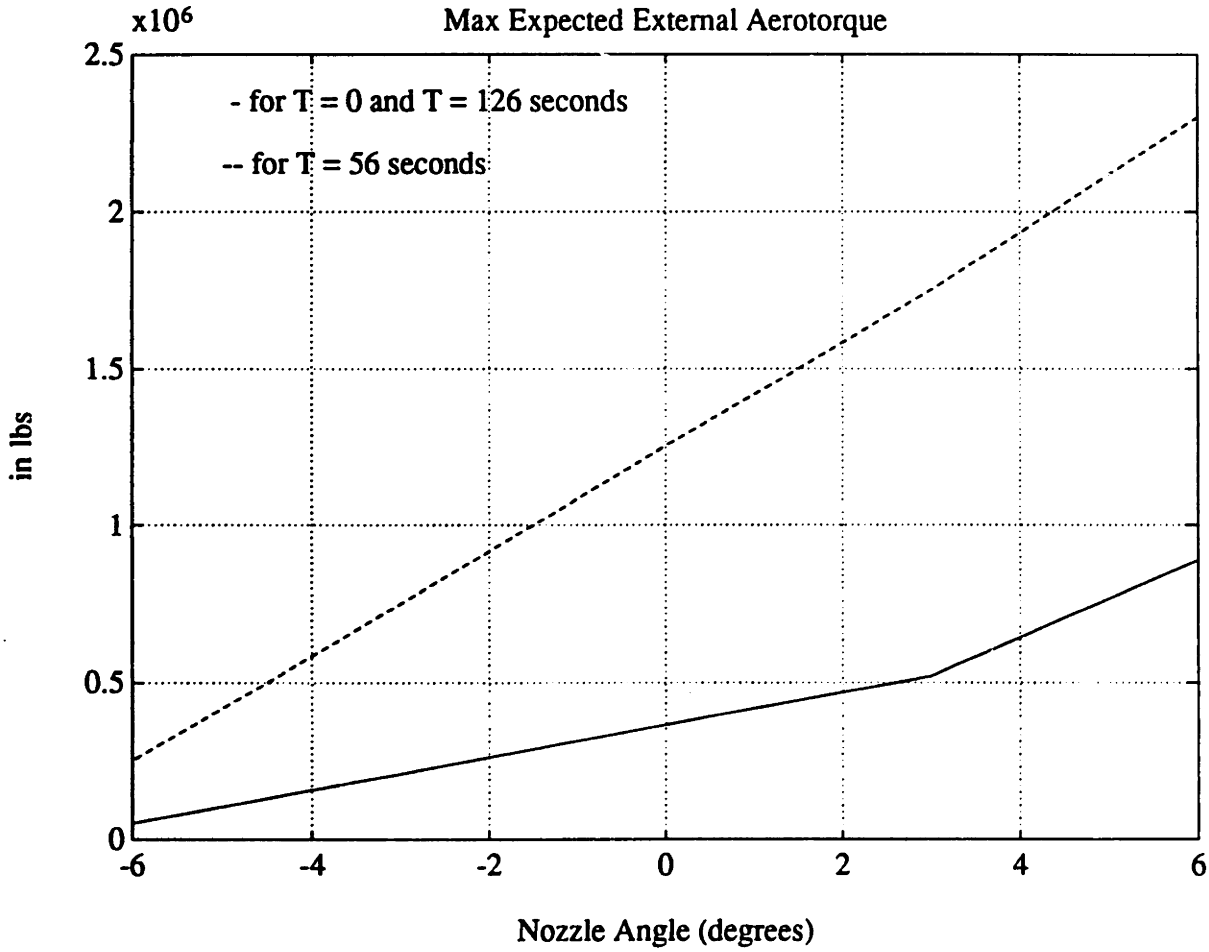

Figure 2-8: Expected Profile of External Aerotorque as a Function of Time [45, 9, 42]

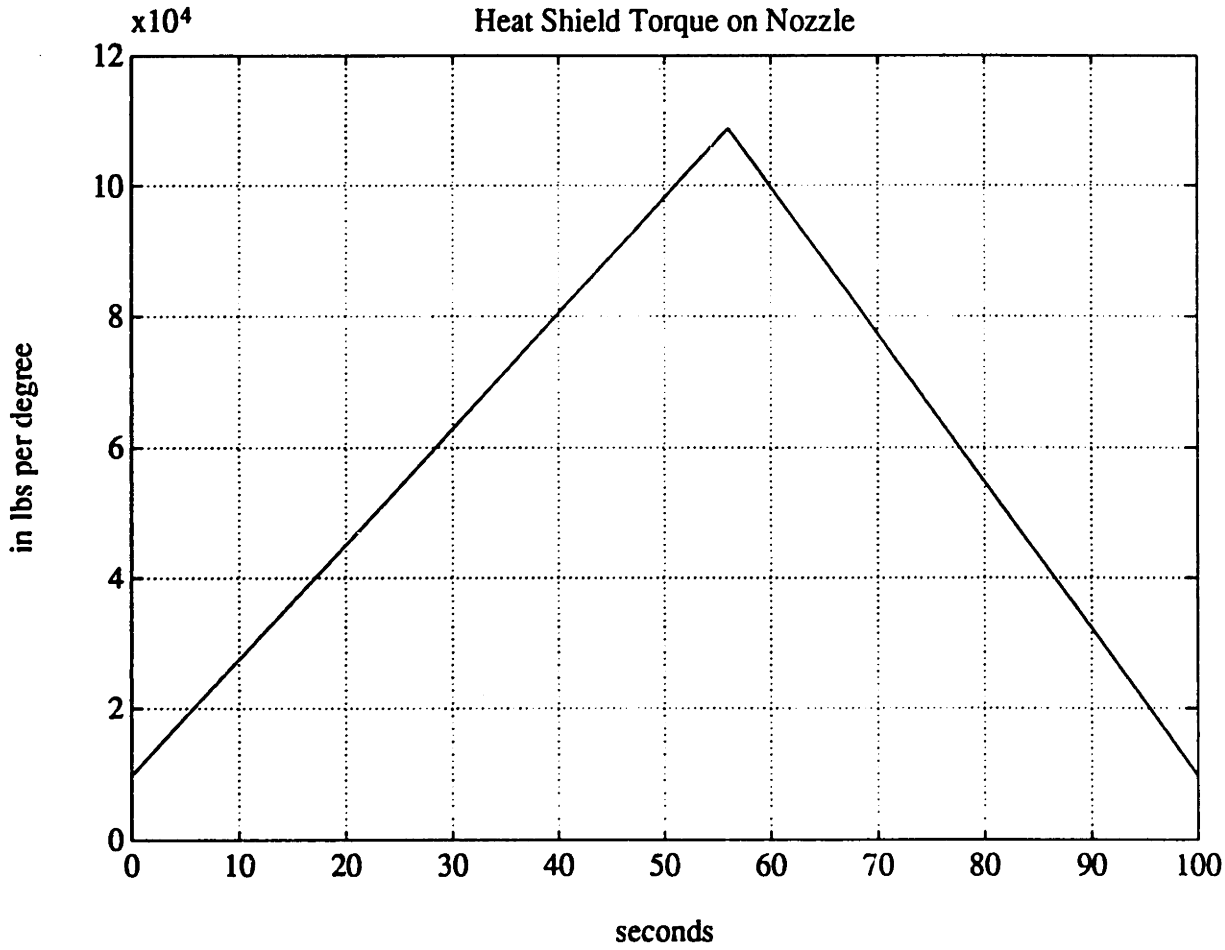

Figure 2-9: Expected Profile of Heat Shield Torque as a Function of Time [29]

The unpressurized flexseal spring rate can be as high as 309,000 in · lbs per degree of nozzle angle. The nominal pressurized flexseal spring rate is approximately 195,000 in · lbs per degree. The pressurized flexseal spring rate can be as low as 128,000 in · lbs per degree.

The flexseal torque in response to step and sinusoidal motion of the nozzle is shown in Figures 2-10 through 2-12. Figure 2-10 is actual measured sinusoidal data at an amplitude of 6.14 degrees and a frequency of 1.64 Hz [40, 38]. The test was conducted under pressurized conditions on a preliminary development and characterization unit. Figure 2-11 is the simulated torque under the same conditions using the Dahl model. Figure 2-12 shows the simulated flexseal torque for nozzle steps from 0 degree to 0.3 degree and then back to 0 degree under nominal pressurized conditions.

Prior to the acceptance of the Dahl model, a variable damping coefficient, combined with a coulomb friction parameter T_{cf}, *was* used to describe the friction portion of the flexseal torque [28]. The model indicated that for commanded nozzle deflections of greater than 1.2 degrees, a constant damping coefficient, BV3 in · lbs seconds per degree nozzle angle, was to be used.

$$B_{flx} = \texttt{BV3} \tag{2.4}$$

For commanded nozzle deflections less than 1.2 degrees, the damping coefficient was to be calculated on the basis of the following equation:

$$B_{flx} = \frac{\texttt{BV1} \cdot |\dot{\theta}|}{\dot{\theta}^2 + \texttt{BV2}} \tag{2.5}$$

where:

$$\begin{aligned} \texttt{BV1} &= 28,000 \text{ in} \cdot \text{lbs} \\ \texttt{BV2} &= 1.2 \text{ deg}^2 \text{ per sec}^2 \\ \texttt{BV3} &= 12,000 \text{ in} \cdot \text{lbs seconds per degree} \\ T_{cf} &= 4000 \text{ in} \cdot \text{lbs} \end{aligned}$$

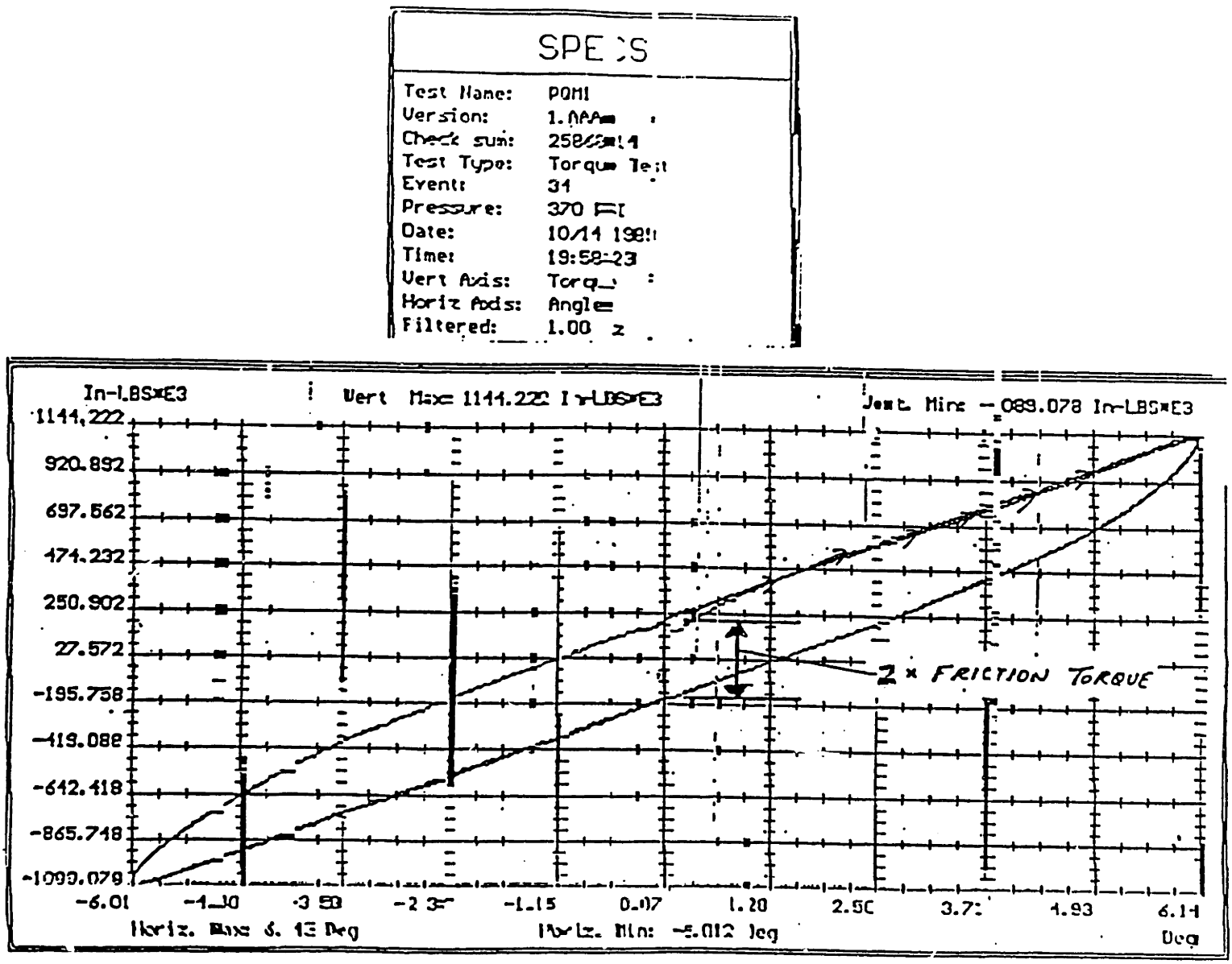

Figure 2-10: Measured Flexseal Torque in Response to Sinusoidal Nozzle Motion at an Amplitude of 6.14 Degrees and a Frequency of 1.64 Hz [40, 38]

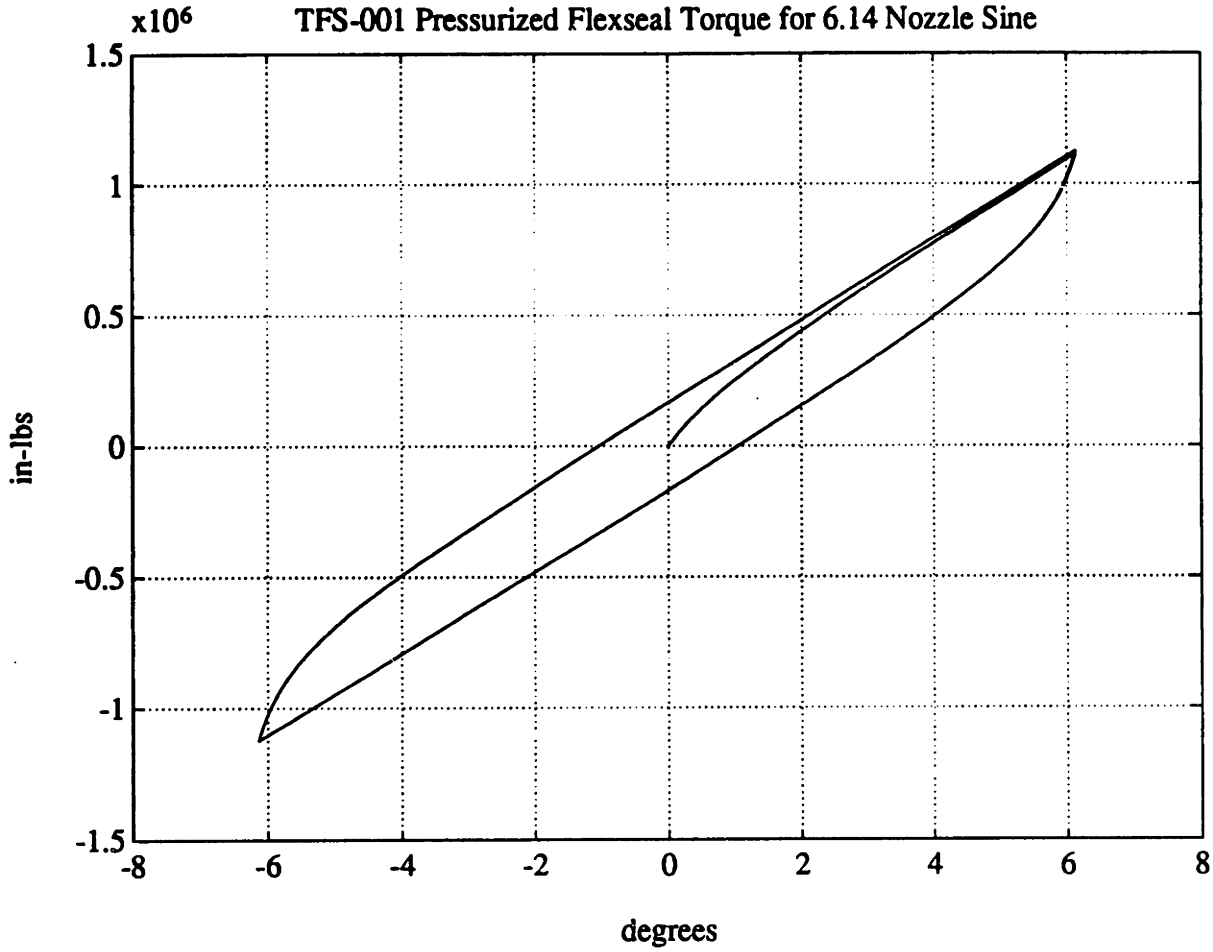

Figure 2-11: Simulated Flexseal Torque in Response to Sinusoidal Nozzle Motion at an Amplitude of 6.14 Degrees and a Frequency of 1.64 Hz.

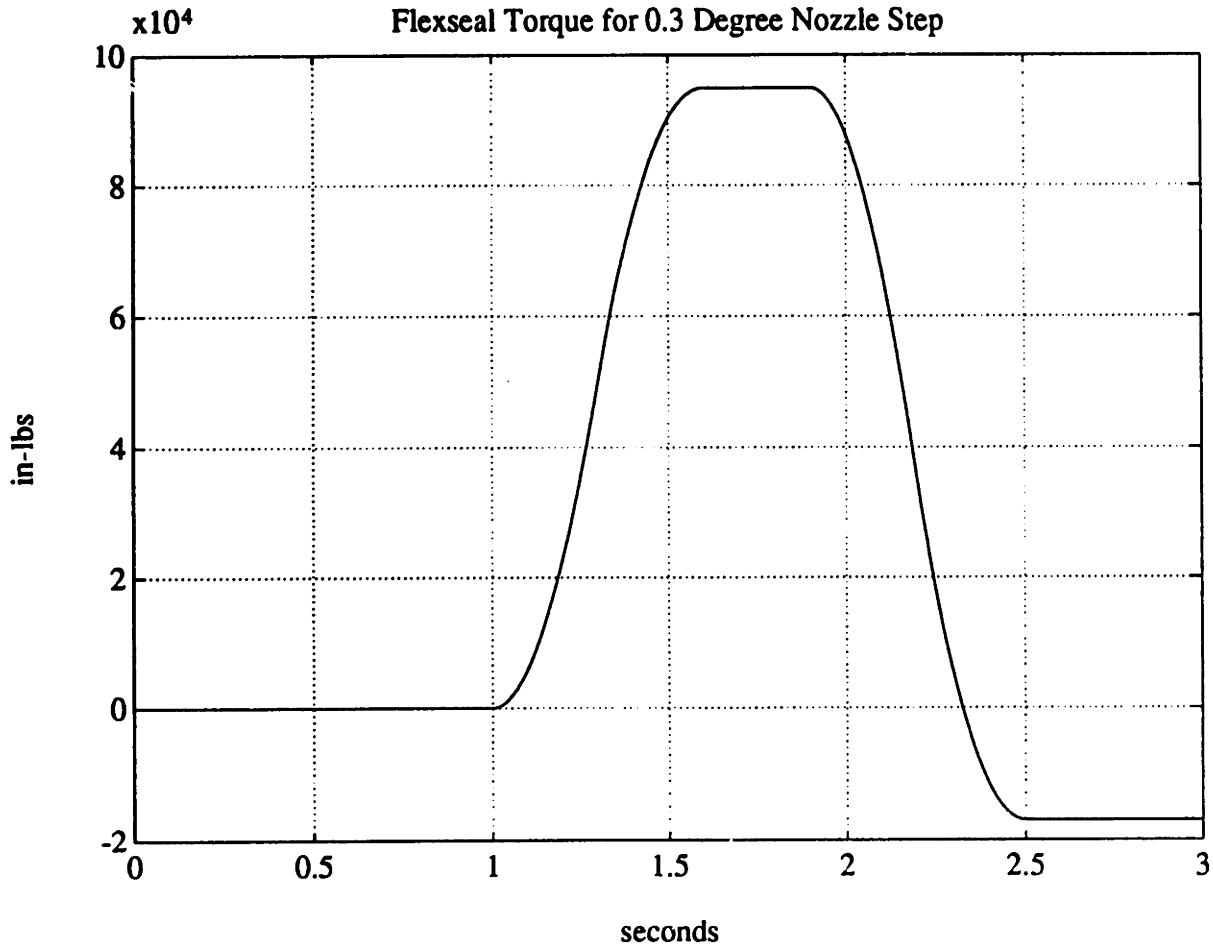

Figure 2-12: Simulated Flexseal Torque in Response to 0.3 Degree Nozzle Steps. [6]

Thus the total flexseal torque *was* described by the following:

$$T_4 = B_{flx}\dot{\theta} + T_{cf} + K_s\theta \tag{2.6}$$

Figures 2-13 and 2-14 compares the performance of the two models for a 6.14 degree sinusoid and a 0.3 degree step under nominal pressurized conditions. The figures indicate that the solid friction characteristic is not very well predicted by the variable damping coefficient/coulomb friction model.

2.1.5 Hydraulic Actuator Torque

The hydraulic actuator torque is transmitted to the nozzle through a series of compliant structures. The compliance parameters include the nozzle stiffness at the actuator attachment point K_1, the rocket aft skirt stiffness K_3, and the actuator rod stiffness K_4. Figure 2-15 illustrates these parameters. If the mass of the piston can be neglected, then the torque is proportional to the displacement of the compliant structures.

$$-K_3X_3 = K_4(X_4 - X_1) = K_1(X_1 - L\theta) = \frac{T_a}{L} \tag{2.7}$$

where:

K_1 = Nozzle Stiffness

K_3 = Aft Skirt Stiffness

K_4 = Actuator Rod Stiffness

L = Effective Moment Arm Length

Note that the nozzle stiffness and the actuator rod stiffness are in series, and can be combined into a single stiffness term K_c. The standard formula for K_c is well known, but it can be easily derived from Equation 2.7.

$$K_1K_4(X_4 - X_1) + K_4K_1(X_1 - L\theta) = (K_1 + K_4)\frac{T_a}{L}$$

$$\frac{K_1K_4}{K_1 + K_4}(X_4 - L\theta) = K_c(X_4 - L\theta) = \frac{T_a}{L} \tag{2.8}$$

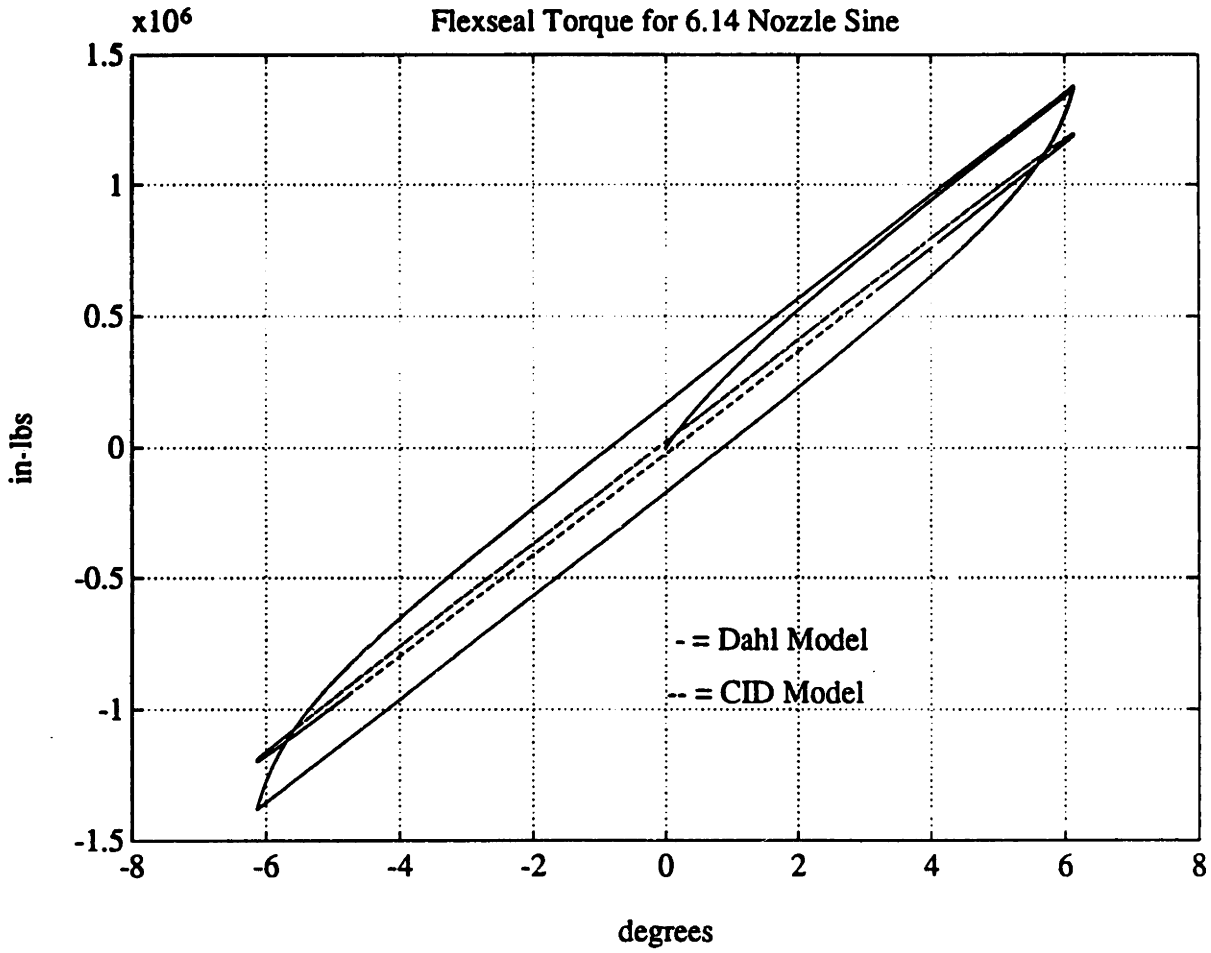

Figure 2-13: Comparison of Flexseal Torque Predictions Using Dahl Solid Friction Model and Variable Damping Coefficients for 6.14 Degree Sinusoidal Nozzle Motion at 1.64 Hz

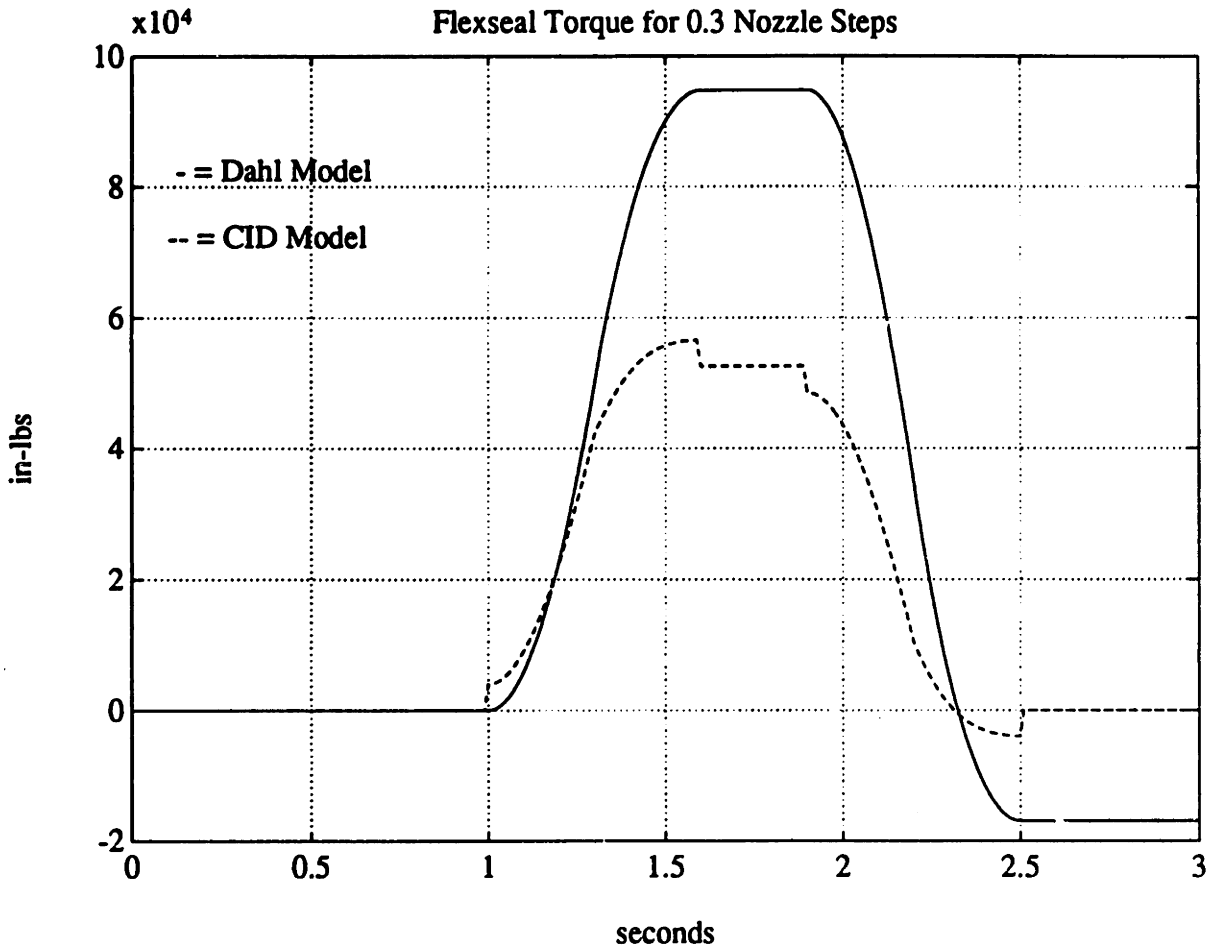

Figure 2-14: Comparison of Flexseal Torque Predictions Using Dahl Solid Friction Model and Variable Damping Coefficients for 0.3 Degree Nozzle Steps

Combining Equations 2.7 and 2.8 yields the following:

$$-K_c K_3 X_3 + K_3 K_c (X_4 - L\theta) = (K_c + K_3)\frac{T_a}{L}$$

$$\frac{K_c K_3}{K_c + K_3}[(X_4 - X_3) - L\theta] = \frac{T_a}{L}$$

$$\frac{K_1 K_4 K_3}{K_1 + K_4 + K_3}[(X_4 - X_3) - L\theta] = \frac{T_a}{L} \tag{2.9}$$

Note that the amount of actuator extension is $(X_4 - X_3)$ which is equivalent to the actuator piston position X_p. Also note that all the stiffnesses now appear in a single series term which can be called the combined compliance, K_e. Thus, the equation used to describe the hydraulic actuator torque is:

$$T_a = L\frac{K_1 K_4 K_3}{K_1 + K_4 + K_3}(X_p - L\theta) = LK_e(X_p - L\theta) \tag{2.10}$$

The geometry of the system is such that the pivot point is not stationary and the effective moment arm length is not constant. Both vary as the shape of the flexseal changes under different nozzle conditions. Figure 2-16 illustrates the geometry. The actuator aft skirt attachment point is a radial distance of ATY, and an axial distance of ATX from the pivot point. The actuator nozzle attachment point is a radial distance of ARY, and an axial distance of ARX from the pivot point. The effective moment arm length is calculated as follows:

$$L = Z_{m1}\cos(\alpha_{m2} + \alpha_{m1} - \frac{\pi}{2}) \tag{2.11}$$

$$Z_{m1} = \sqrt{\mathtt{ARX}^2 + \mathtt{ARY}^2} \tag{2.12}$$

$$\alpha_{m1} = \arctan(\frac{\mathtt{ARX}}{\mathtt{ARY}}) \tag{2.13}$$

$$\alpha_{m1} = \arctan(\frac{\mathtt{ARX} - \mathtt{ATX}}{\mathtt{ATY} - \mathtt{ARY}}) \tag{2.14}$$

For zero motor pressure (SRMU not firing) and zero nozzle angle, for example [28]:

$$\begin{aligned} \texttt{ATY} &= 54.5 \text{ in} \\ \texttt{ATX} &= 0.7 \\ \texttt{ARY} &= 46.11 \\ \texttt{ARX} &= 51.38 \end{aligned}$$

For this particular case, $L = 53.883$ in. [13] indicates a maximum $L = 54.435$ in, a minimum $L = 52.910$ in, and an average $L = 53.82$ in.

2.2 Piston Movement and Pressure

A second order differential equation for piston position can be constructed based on the simplified representation of the TVC servo arrangement depicted in Figure 2-17. K_e is the combined compliance derived in the previous section.

$$M_p \frac{d^2 X_p}{dt^2} = A_p(P_1 - P_2) - K_e(X_p - L\theta) - B_{fa}\frac{dX_p}{dt} - F_{ca} \tag{2.15}$$

where:

$$\begin{aligned} A_p &= \text{Piston Facial Area} \\ B_{fa} &= \text{Piston Viscous Damping Coefficient} \\ F_{ca} &= \text{Piston Coulomb Friction} \\ M_p &= \text{Mass of Piston} \\ P_1 &= \text{Pressure in Actuator Chamber 1} \\ P_2 &= \text{Pressure in Actuator Chamber 2} \end{aligned}$$

The actuator chamber pressures are determined by the fluid bulk modulus and the volume of fluid in the chamber. The bulk modulus is slightly decreased by a 2% air entrainment factor. The fluid volumes are based upon the total actuator linear displacement XTS, and the piston facial area A_p. The actuator volume is increased by an additional 10% to account for the volume of the hydraulic lines.

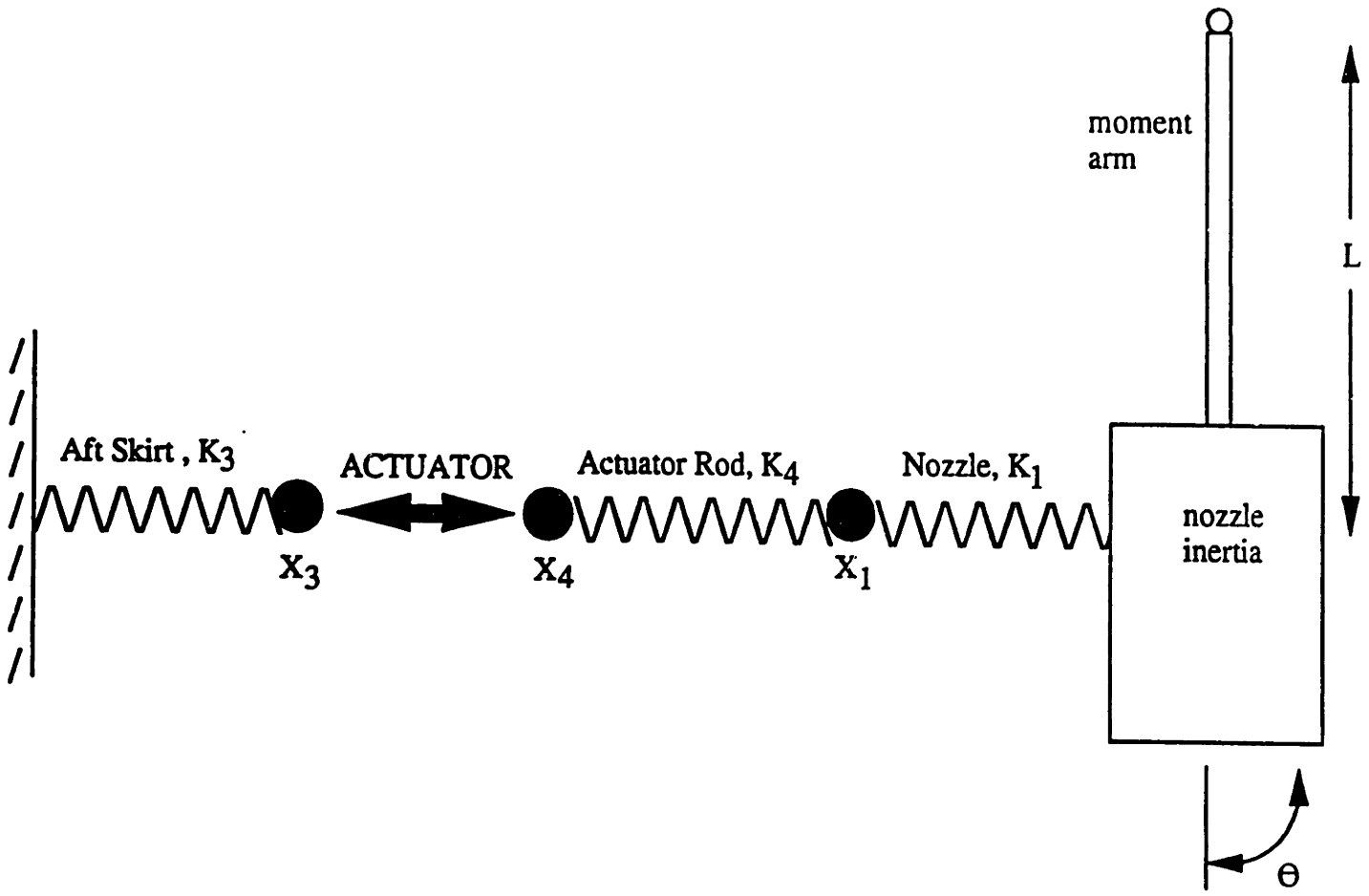

Figure 2-15: The Hydraulic Actuator Torque is Transmitted to the Nozzle Through a Series of Compliant Structures

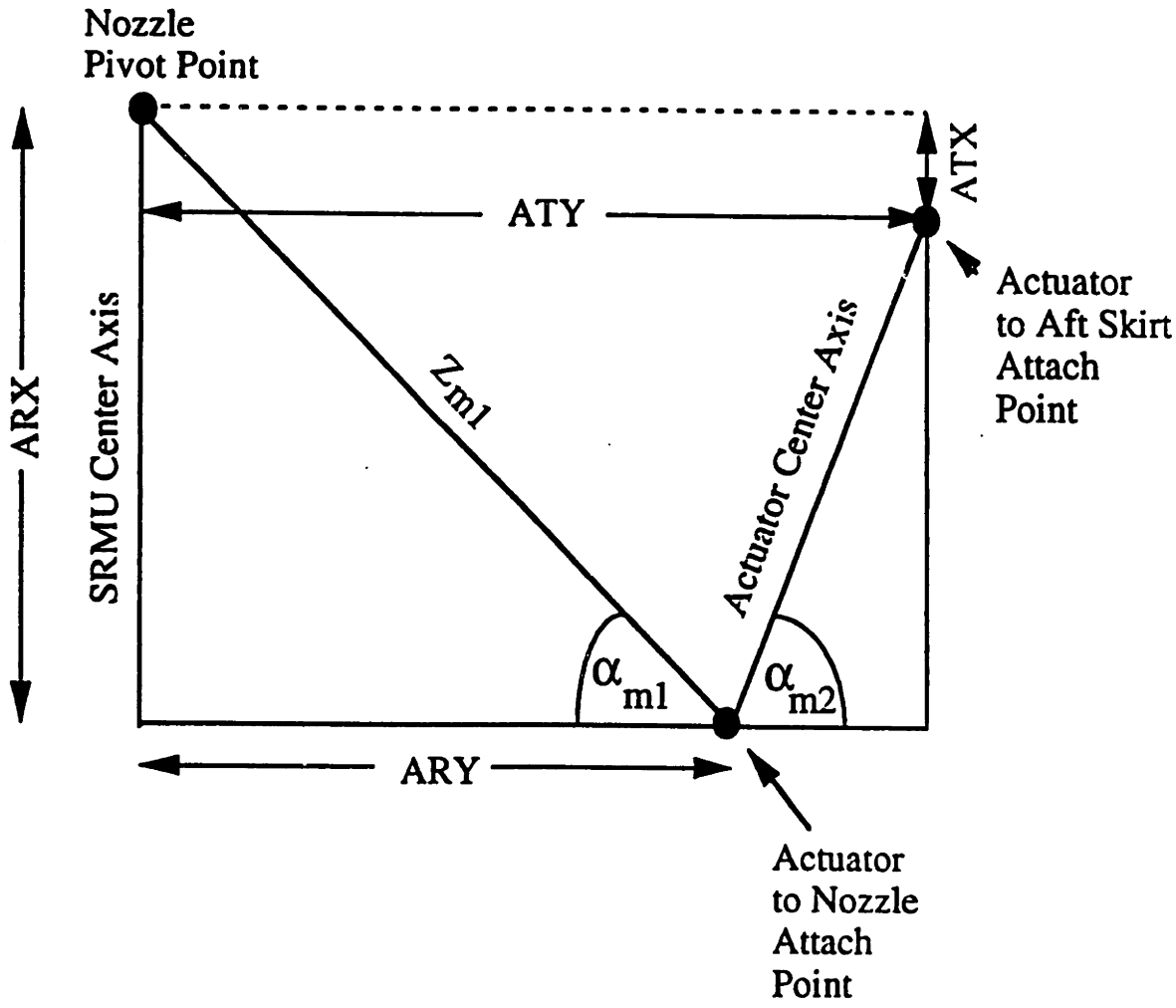

Figure 2-16: Nozzle Control System Attach Point Geometry

$$\frac{dP_1}{dt} = \frac{\mathtt{AE} \cdot \beta_e}{V_1(X_p)}[Q_1 - C_{em}P_1 - C_{im}(P_1 - P_2) - A_p\frac{dX_p}{dt}] \tag{2.16}$$

$$\frac{dP_2}{dt} = \frac{\mathtt{AE} \cdot \beta_e}{V_2(X_p)}[-Q_2 - C_{em}P_2 + C_{im}(P_1 - P_2) + A_p\frac{dX_p}{dt}] \tag{2.17}$$

$$V_1(X_p) = A_p(\frac{1.1 \cdot \mathtt{XTS}}{2} + X_p) \tag{2.18}$$

$$V_2(X_p) = A_p(\frac{1.1 \cdot \mathtt{XTS}}{2} - X_p) \tag{2.19}$$

where:

$\mathtt{AE}$	=	2% Air Entrainment Factor
β_e	=	Fluid Bulk Modulus
C_{em}	=	Actuator External Leakage Coefficient
C_{im}	=	Actuator Internal Leakage Coefficient
Q_1	=	Fluid Flow into Chamber 1
Q_2	=	Fluid Flow out of Chamber 2
$V_1(X_p)$	=	Volume of Actuator Chamber 1
$V_2(X_p)$	=	Volume of Actuator Chamber 2

2.3 Fluid Flow

The flow of fluid through the servovalve to and from the actuator is described by the equation for flow through an orifice, which is derived from the Navier-Stokes equations on the basis of incompressible flow [33, 41, 32, 14].

$$Q = \mathtt{CO} \cdot \mathtt{WS} \cdot x_{sv}\sqrt{2(P_{HO} - P_{LO})} \tag{2.20}$$

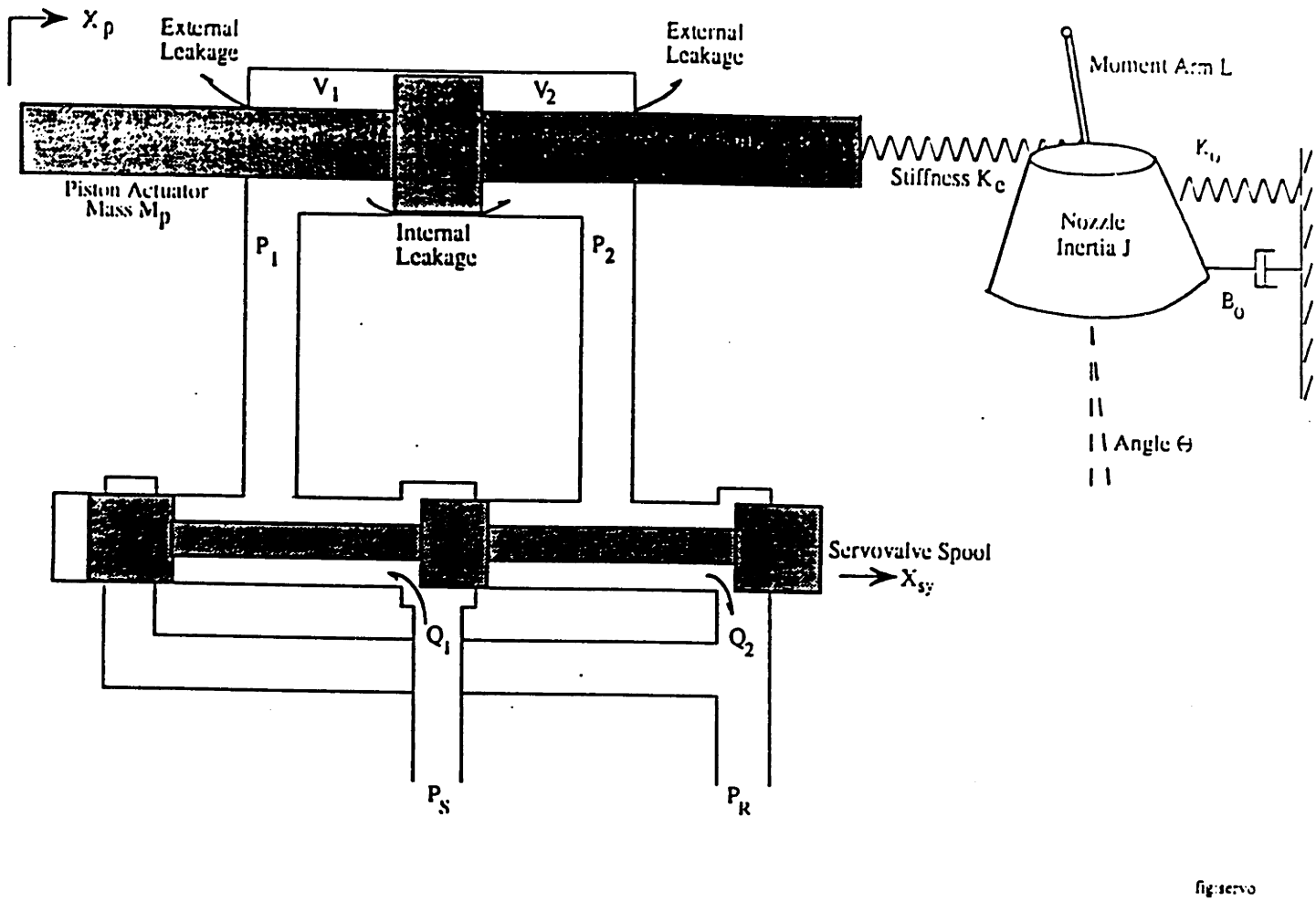

Figure 2-17: Simplified Representation of TVC Servo Arrangement

where:

Q = Either Flow from Servovalve to Actuator or Vice Versa

$\mathtt{CO}$ = $C_d\sqrt{\frac{1}{\rho}}$

C_d = Discharge Coefficient

ρ = Fluid Mass Density

$\mathtt{WS}$ = Area Gradient

x_{sy} = Valve Spool Displacement

P_{HO} = High Pressure Side of Flow

P_{LO} = Low Pressure Side of Flow

If flow from the hydraulic supply, through the servovalve, to chamber 1 of the actuator is being described, then P_{HO} is the supply pressure, and P_{LO} is the pressure in chamber 1. There is also flow from chamber 2 of the actuator, through the servovalve, to the hydraulic reservoir. Equation 2.20 also describes this, with P_{HO} being the pressure in chamber 2, and P_{LO} being the pressure in the hydraulic reservoir. In the alternative situation, the servovalve spool has opened in the other direction, and x_{sy} is negative. In this case, Equation 2.20 describes the flow from the hydraulic supply, through the servovalve, to chamber 2 of the actuator; P_{HO} is the supply pressure, and P_{LO} is the pressure in chamber 2. In addition, there is flow from chamber 1 of the actuator, through the servovalve, to the hydraulic reservoir. Equation 2.20 also describes this, with P_{HO} being the pressure in chamber 1, and P_{LO} being the pressure in the hydraulic reservoir. Thus, a description of the flows in a servoactuation system generally requires four different forms of Equation 2.20. See [33].

To account for pressure losses in the hydraulic lines and in the servovalve, Equation 2.20 must be modified [19]. Both types of losses have an apparent effect on the supply pressure. Line losses vary quadratically with flow:

$$P_{HO} = P_H - \mathtt{RF} \cdot Q^2 \tag{2.21}$$

where:

P_H = Pressure at Beginning of Line of Flow

RF = Line Loss Coefficient

Substituting Equation 2.21 in Equation 2.20 and solving for Q yields the following:

$$Q = \frac{\mathtt{CO} \cdot \mathtt{WS} \cdot x_{sy}\sqrt{2(P_H - P_{LO})}}{\sqrt{1 + 2 \cdot \mathtt{RF}(\mathtt{CO} \cdot \mathtt{WS} \cdot x_{sy})^2}} \tag{2.22}$$

Valve losses are measured with the servovalve fully open and expressed in the orifice equation as a proportional loss.

$$Q_m = \mathtt{FQ} \cdot \mathtt{CO} \cdot \mathtt{WS} \cdot \mathtt{XSL}\sqrt{2(P_H - P_{LO})} \tag{2.23}$$

where:

Q_m = Measured Volumetric Flow Rate

FQ = Valve Loss Ratio

XSL = Maximum Valve Spool Displacement

For convenience sake, the valve losses can be expressed with a quadratic loss coefficient analogous to RF. The following trial equation can be written:

$$Q_m = \mathtt{CO} \cdot \mathtt{WS} \cdot \mathtt{XSL}\sqrt{2(P_H - \mathtt{RV} \cdot Q_m^2 - P_{LO})} \tag{2.24}$$

where:

RV = Valve loss coefficient to be solved for

Solving for Q_m just as in Equation 2.22 yields the following:

$$Q_m = \frac{\mathtt{CO} \cdot \mathtt{WS} \cdot \mathtt{XSL}\sqrt{2(P_H - P_{LO})}}{\sqrt{1 + 2 \cdot \mathtt{RV}(\mathtt{CO} \cdot \mathtt{WS} \cdot \mathtt{XSL})^2}} \tag{2.25}$$

Setting Equation 2.25 equal to Equation 2.23 and solving for RV yields the following:

$$\mathtt{RV} = \frac{\frac{1}{\mathtt{FQ}^2} - 1}{(\mathtt{CO} \cdot \mathtt{WS} \cdot \mathtt{XSL})^2} \tag{2.26}$$

RF and RV can be combined into a single loss coefficient:

$$\mathtt{RCW} = 2(\mathtt{RF} + \mathtt{RV})(\mathtt{CO} \cdot \mathtt{WS})^2 \tag{2.27}$$

Analogous with the formulation of Equation 2.22 and Equation 2.25, Equation 2.20 with valve and line losses becomes [19]:

$$Q = \frac{\mathtt{CO} \cdot \mathtt{WS} \cdot x_{sy}\sqrt{2(P_H - P_{LO})}}{\sqrt{1 + \mathtt{RCW} \cdot x_{sy}^2}} \tag{2.28}$$

A description of the actuator flows in the hydraulic TVC system requires four different forms of Equation 2.28.

2.4 Supply Pressure

Hydraulic power for the flight TVC configuration is provided by a warm gas driven turbine-centrifugal pump for each piston actuator. See Figure 2-4. Each pump has its own heat exchanger and gas generator. Redundant supply and return lines allow one of the Hydraulic Power Units (HPU) to feed both actuators should the other fail. The pressure selector valves manage the HPU redundancy automatically.

Figure 2-18 depicts the supply pressure characteristic as a function of flow demand. Each HPU is capable of roughly 154 hydraulic horsepower or 1 million psi-cis (pounds per square inch - psi) (cubic inches per second - cis) [45]. A pressure relief valve near the pump output is designed to regulate the pressure at no greater than a nominal $P_o = 3200$ psi. The relief valve is a two-stage pilot operated unit which is capable of bleeding up to 577 cis of flow. Under worst case conditions, the relief valve may allow 3580 psi of pressure to build [10]. For modeling purposes however, it is assumed to be an ideal, instantaneous regulating device. If flow output is less than QOG = 396 cis, the supply pressure remains constant. If flow output exceeds QOG, then the supply pressure varies linearly with supply flow.

The variation of supply pressure with flow introduces another modification to

Equations 2.20 and 2.28 for supply flow. If the slope of the supply flow versus supply pressure curve is SPQ, and this slope is constant up to a flow QG and a pressure PG, then [19]:

$$Q = K_p \cdot \mathtt{CO} \cdot \mathtt{WS} \cdot x_{sy}\sqrt{2[\mathtt{SPQ}(Q + Q_+ - \mathtt{QG}) + \mathtt{PG} - P_{LO}]} \tag{2.29}$$

$$K_p = \frac{1}{\sqrt{1 + \mathtt{RCW} \cdot x_{sy}^2}} \tag{2.30}$$

Q_+ is any additional flow required from the pump, such as jet deflector pilot stage flows. Solving for Q in Equation 2.29 yields a quadratic equation in Q.

$$Q^2 + BQ + C = 0 \tag{2.31}$$

Therefore, the supply flow is as follows:

$$Q = \frac{-B + \sqrt{B^2 - 4C}}{2} \tag{2.32}$$

$$B = -2(K_p \cdot \mathtt{CO} \cdot \mathtt{WS} \cdot x_{sy})^2 \cdot \mathtt{SPQ} \tag{2.33}$$

$$C = -2(K_p \cdot \mathtt{CO} \cdot \mathtt{WS} \cdot x_{sy})^2 \cdot [\mathtt{SPQ}(Q_+ - \mathtt{QG}) + \mathtt{PG} - P_{LO}] \tag{2.34}$$

2.5 Servovalve

The servovalve controlling the flow into the actuator is a two-stage single inlet jet deflector type unit [8]. See Figure 2-19. In the first-stage, three redundant deflector jet hydraulic amplifiers are mechanically controlled by three torque motors, as shown in Figure 2-20. Figure 2-21 illustrates the output of the deflector jet amplifiers driving a second-stage sliding spool, the hydraulic gate to the actuator. Three cantilever springs feed back spool position as a torque on the motor armatures.

The fluidic amplifier consists of a disc with a "stick man" shape cutout which forms a single pressure jet and two receiver ports. A movable deflector sits across the "arms" of the "stick man." The jet of fluid from the pressure nozzle normally impinges directly between the two receiver ports, resulting in equal pressure from

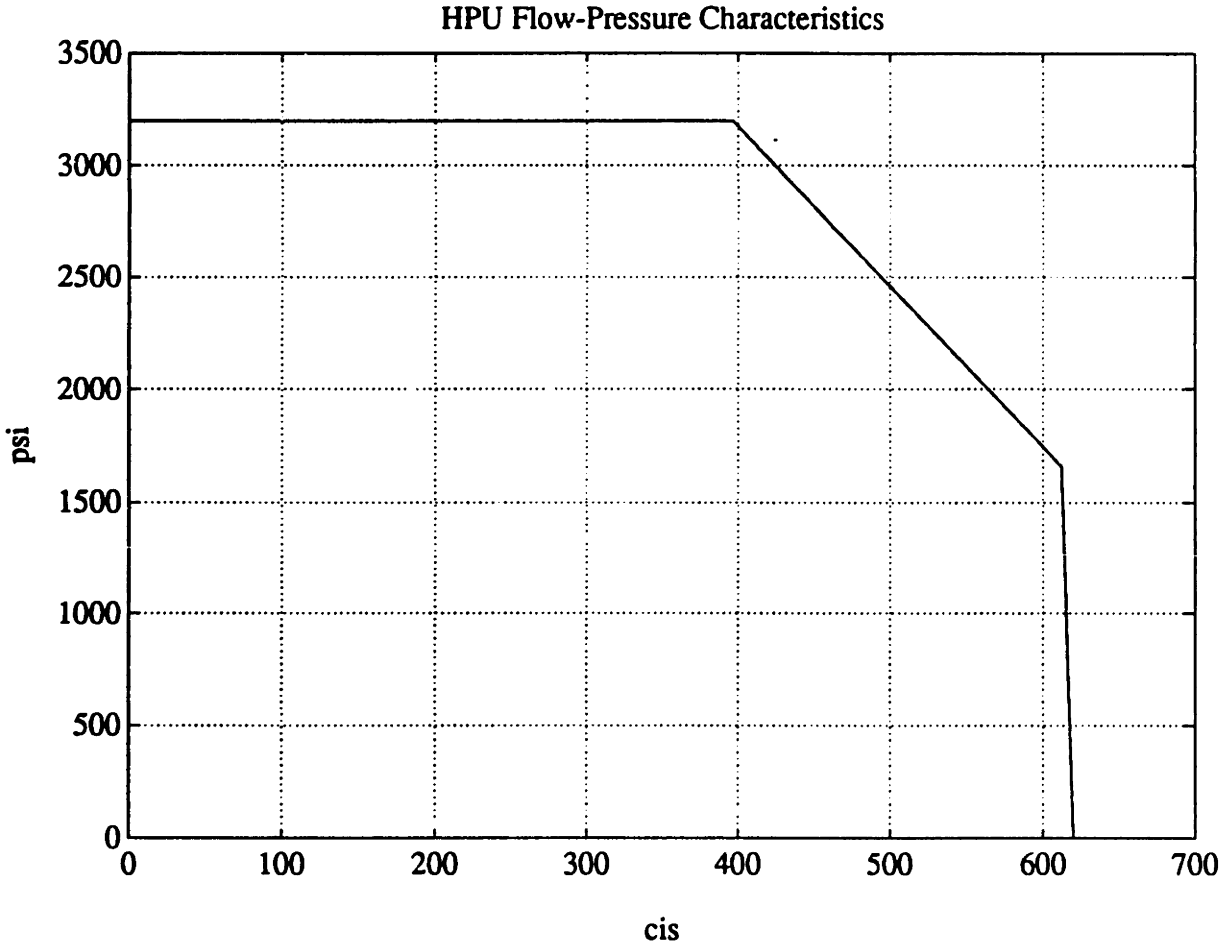

Figure 2-18: Approximate Flow-Pressure Characteristics of Hydraulic Power Unit (HPU) [45]

both. Moving the deflector to one side changes the presure balance, thus affecting the position of the spool.

A block diagram of the math model [45] of the servovalve is shown in Figure 2-22. The input current drives the three torque motor/fluidic amplifiers. The first-stage flow is described by the following first-order differential equation:

$$\frac{dQ_a}{dt} = \frac{I_c' K_q - Q_a}{\tau} \tag{2.35}$$

$$|Q_a| \leq Q_{sl}$$

where:

I_c' = Effective Input Current Due to Feedback Spring

K_q = First Stage Flow Gain

τ = First Stage Time Constant

Q_{sl} = First Stage Flow Limit

The "stick man" shape is not a perfect amplifier; a small flow threshold of $Q_{st} = 0.004$ cis exists to the spool. The fluidic amplifier flow is integrated and divided by the spool drive area $A_1 = 0.3608$ in^2 to obtain spool position. The feedback spring has the effect of increasing spool drive fluid pressure on the spool (as does the mass of the spool), due to increased resistance to motion. Increased fluid pressures at the same flow rate is approximately equivalent to decreased flow rates at the same pressure. For simplicity, in order to avoid a second-order model just for the motion of the spool, the latter is how the pressure effect of the spring is modeled. Thus the motion of the spool is described by a first-order differential equation:

$$\frac{dx_{sy}}{dt} = \frac{\mathtt{NTM} \cdot Q_a' - Q_{xo} x_{sy}}{A_1} \tag{2.36}$$

$$|x_{sy}| \leq \mathtt{XSL}$$

where:

A_1 = Spool Drive Area

NTM = Number of Torque Motors

Q'_a = First Stage Flow Minus Threshold

Q_{xo} = Pressure Coefficient

XSL = Maximum Valve Spool Displacement

x_{sy} = Servovalve Spool Position

Torque never enters explicitly into the equations either, so there is not a second-order model for just the fluidic amplifiers. The purpose of the feedback spring is to offset some of the torque from the torque motors. The offsetting of torque from the torque motors is effectively equivalent to a decrease in current:

$$I'_c = I_c - K_{vl} x_{sy} \tag{2.37}$$

where:

K_{vl} = Valve Feedback Gain

I_c = Servovalve Input Current

2.6 Flight Loop Closure Unit and Interim Loop Closure Unit

The analog electronic Flight Loop Closure Unit (FLCU) receives nozzle vectoring commands along the pitch and yaw axes and translates them into appropriate tilt and rock actuator servovalve currents. The FLCU receives nozzle position feedback from the nozzle position transducers (NPT) and actuator pressure feedback from the actuator differential pressure transducers. The output of the pressure transducers is differentiated by a high pass filter to provide nozzle rate feedback. The effect of this inner loop compensation is essentially an overall closed loop system with increased damping and bandwidth. This is referred to as dynamic pressure feedback (DPF) [15, 41].

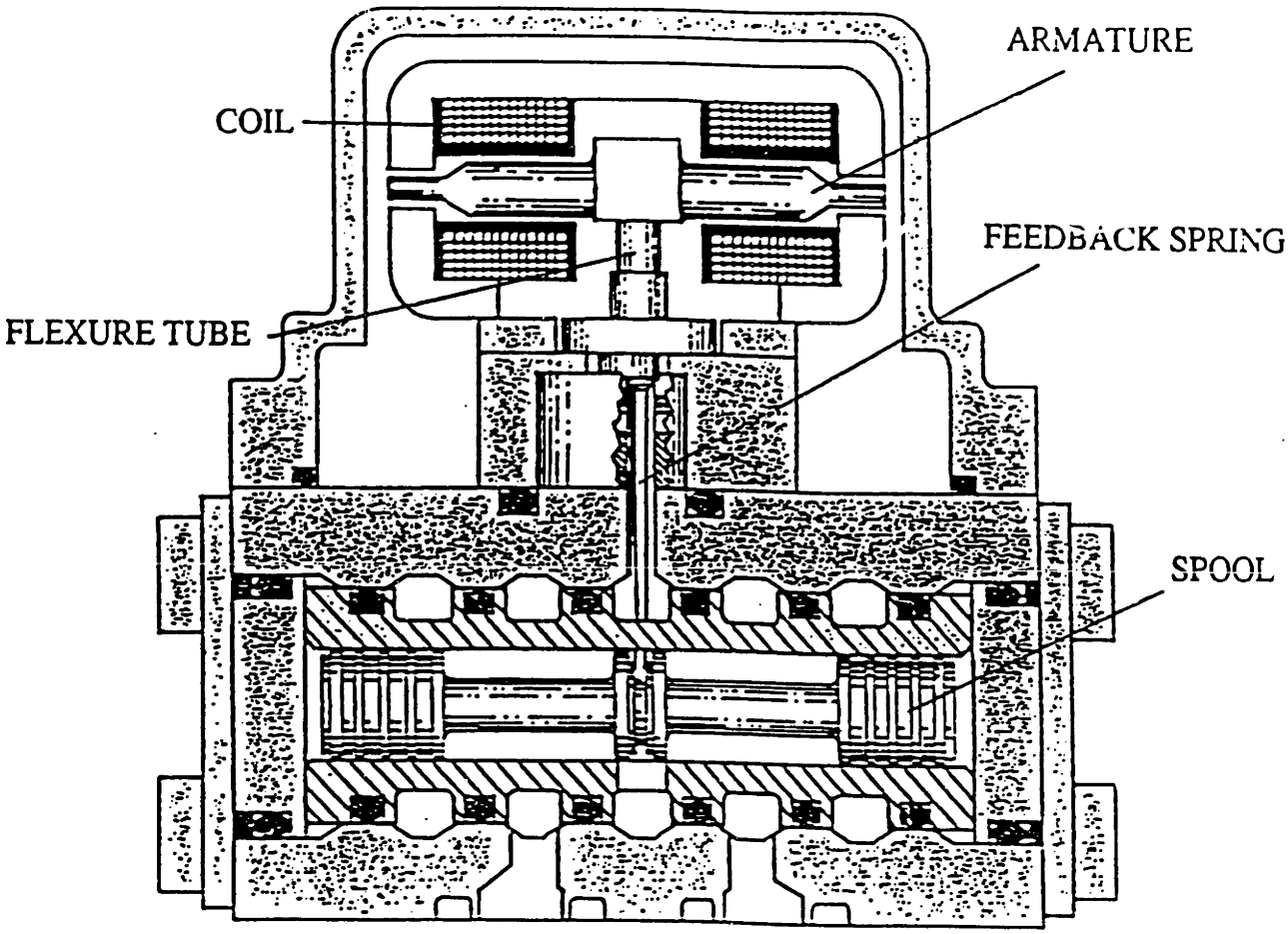

Figure 2-19: Cross Section of Jet Deflector Servovalve with a Single Torque Motor/ Hydraulic Amplifier Assembly. Courtesy Moog Inc. [8]

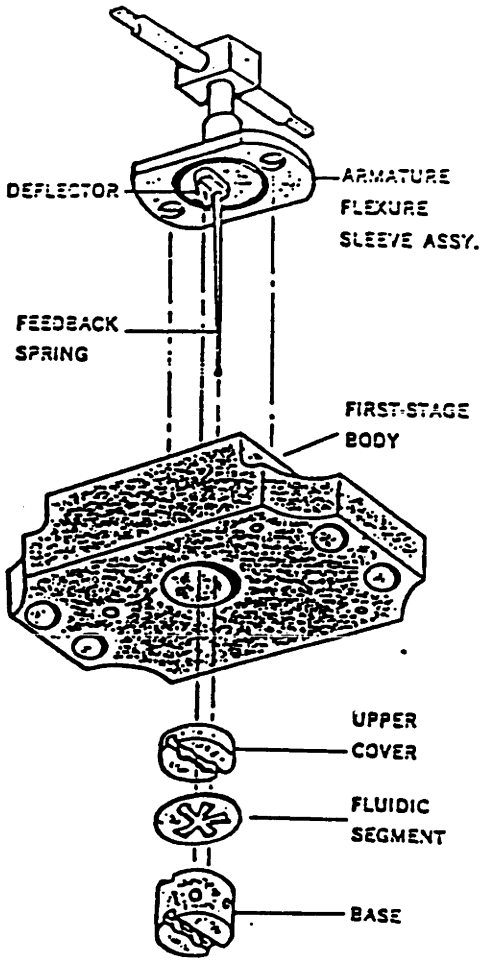

Figure 2-20: First Stage of Jet Deflector Servovalve Showing A Single Torque Motor and Hydraulic Amplifier. Courtesy Moog Inc. [8]

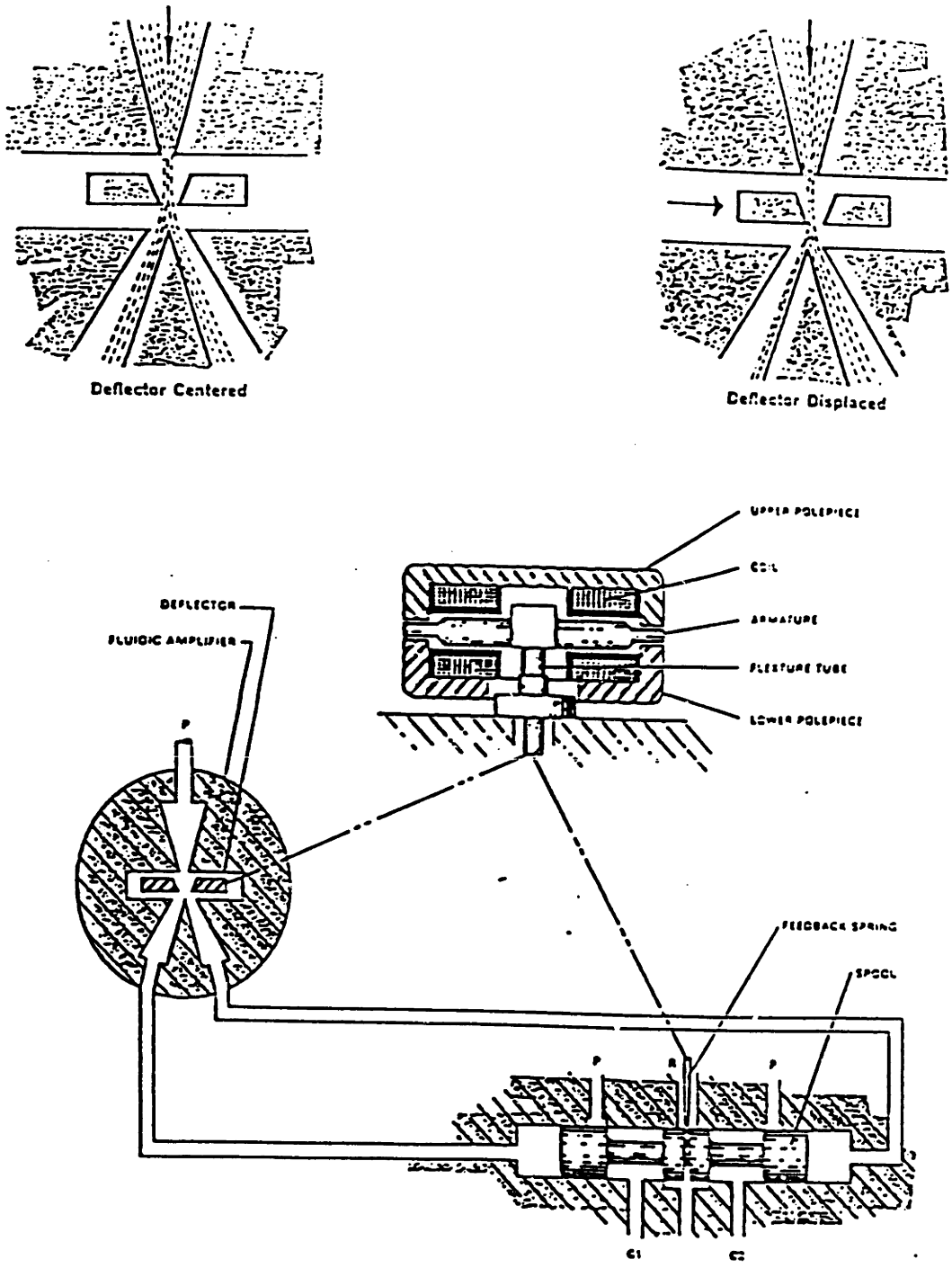

Figure 2-21: Schematic Diagram of Jet Deflector Servovalve Illustrating the Function of a Single Jet Deflector in Positioning the Servovalve Spool. Courtesy Moog Inc. [8]

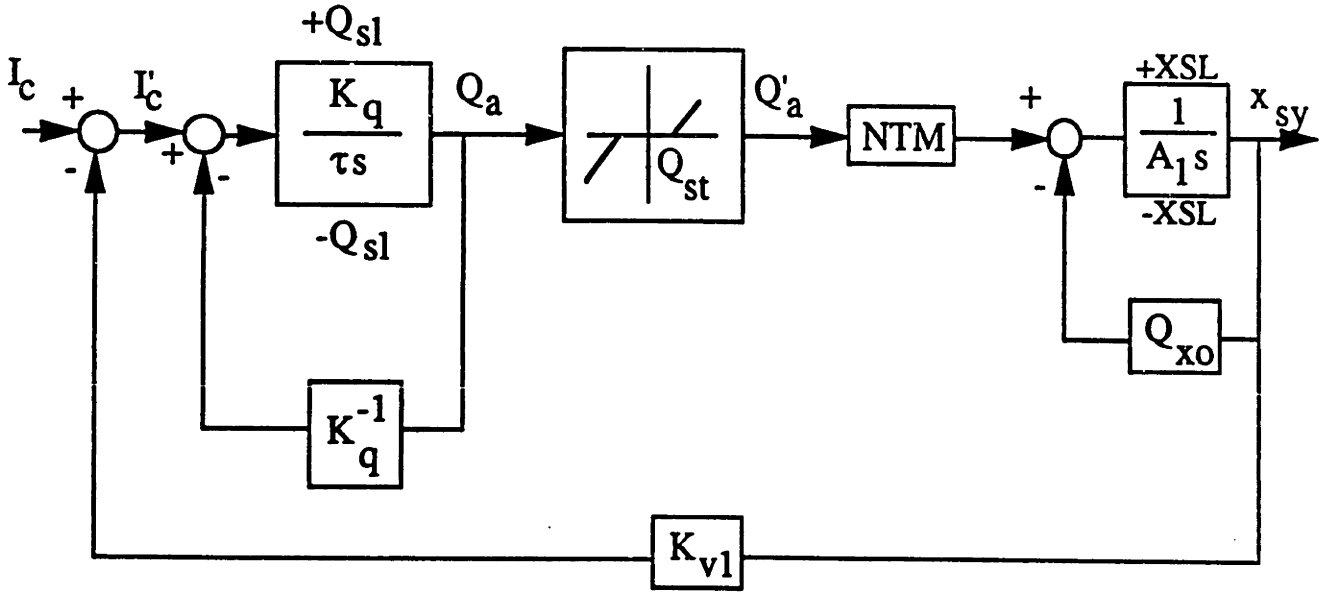

Figure 2-22: Block Diagram of Math Model [45] of TVC System Jet Deflector Servovalves

For development and initial testing purposes, an Interim Loop Closure Unit (ILCU) without DPF is used [2, 16]. A block diagram for the TVC system with appropriate filters and compensation in the ILCU is shown in Figure 2-23. The linearized TVC hydraulic hardware transfer functions are derived in the next chapter. Compensation includes a second order notch filter in the forward path and a second order lead filter in the feedback path. The notch is intended to cancel the nozzle assembly natural frequency, and is located at 8.64 Hz. The notch numerator has a damping ratio of 0.05, and the notch denominator has a damping ratio of 0.6. The frequency response of the notch filter is shown in Figure 2-24. The lead zero is at 7 Hz, and the lead pole is at 30 Hz. The lead numerator has a damping ratio of 0.05, and the lead denominator has a damping ratio of 0.6. The frequency response of the lead is shown in Figure 2-25. A feedback information demodulation filter is also included in the loop. The demodulation filter is a second order low pass filter with poles at 120 Hz and a damping ratio of 0.6. The frequency response of the demodulation filter is shown in Figure 2-26.

The frequency response of the linearized TVC system open position loop with ILCU is shown in Figure 2-27. The uncompensated open loop curve, without the notch and lead filters, is also shown. Note that the notch is not very effective in concealing the underdamped nozzle assembly mode. Approximately 7 dB of gain margin, and 60 degrees of phase margin result. The frequency response of the linearized TVC system closed position loop with ILCU is shown in Figure 2-28.

2.7 Model Performance with Interim Loop Closure Unit

Figures 2-30 through 2-35 show the correlation between measured data from Preliminary Qualification Motor (PQM-1) Pathfinder Phase III tests [43, 27] and simulated results using nonlinear hydraulic equations [22, 20]. These tests consisted of a series of TVC vectoring excercises using the idle (not firing) SRMU on the test stand at Phillips Laboratory, Edwards Air Force Base, September 5-6, 1990. The test config-

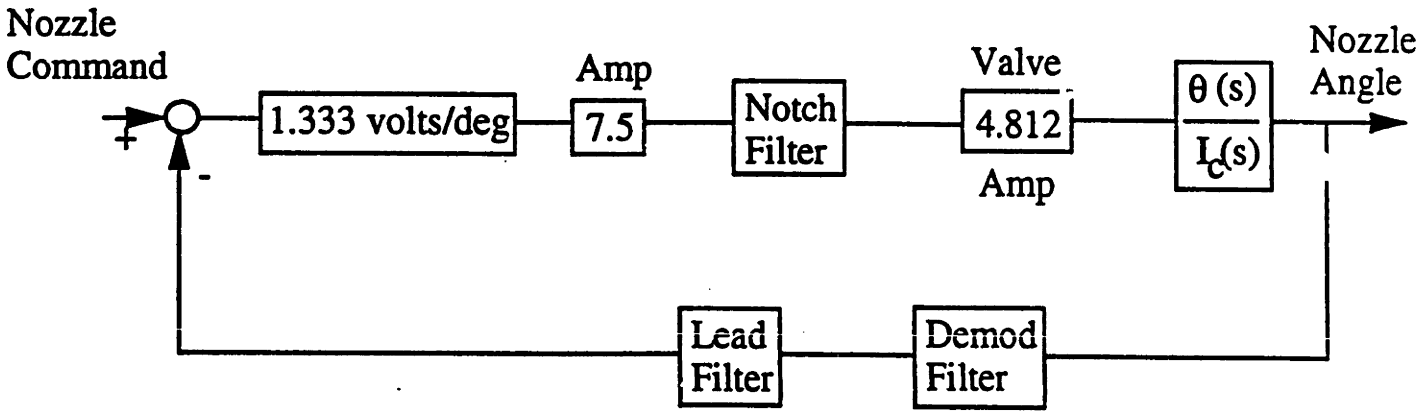

Figure 2-23: Block Diagram of TVC System with ILCU [2].

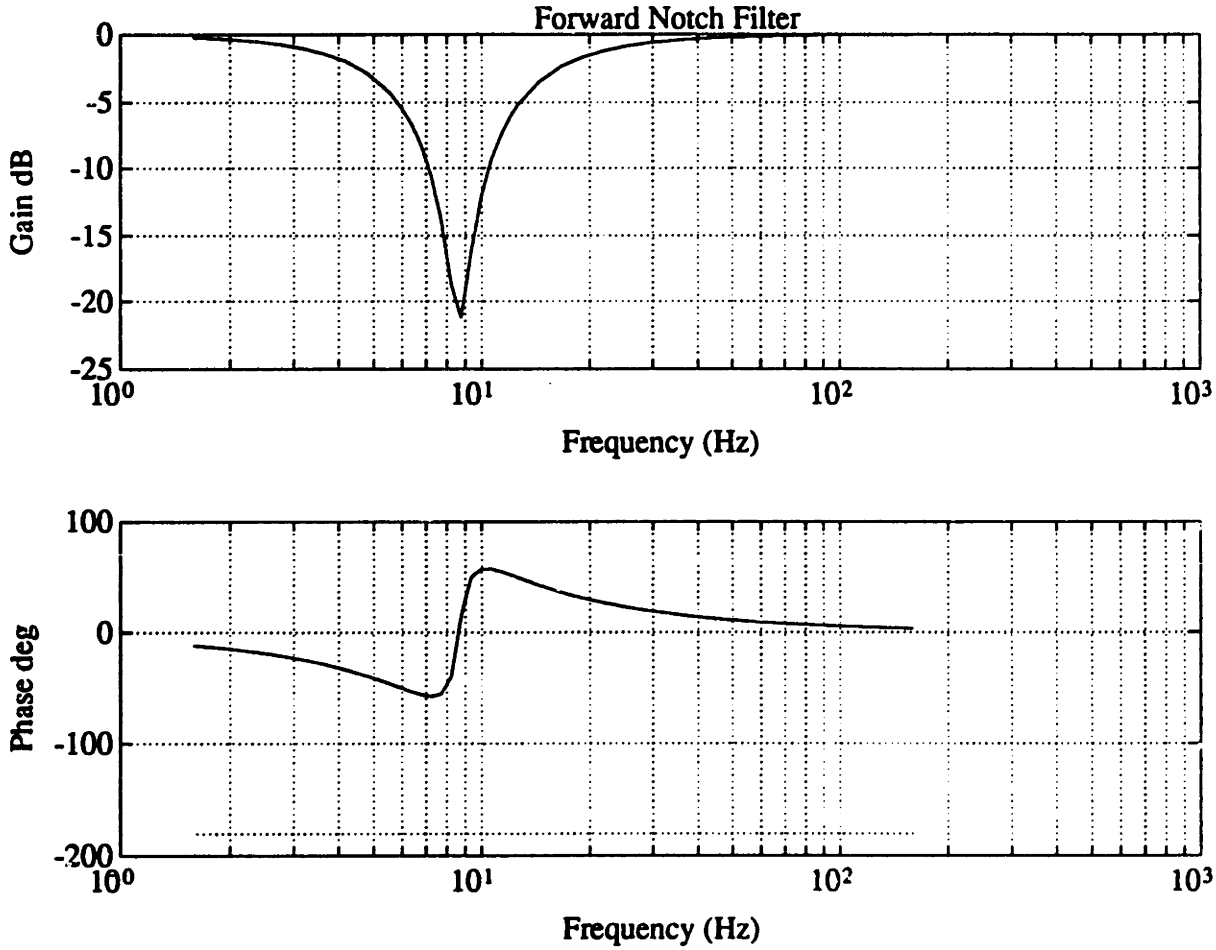

Figure 2-24: Frequency Response of Notch Filter in ILCU [2]

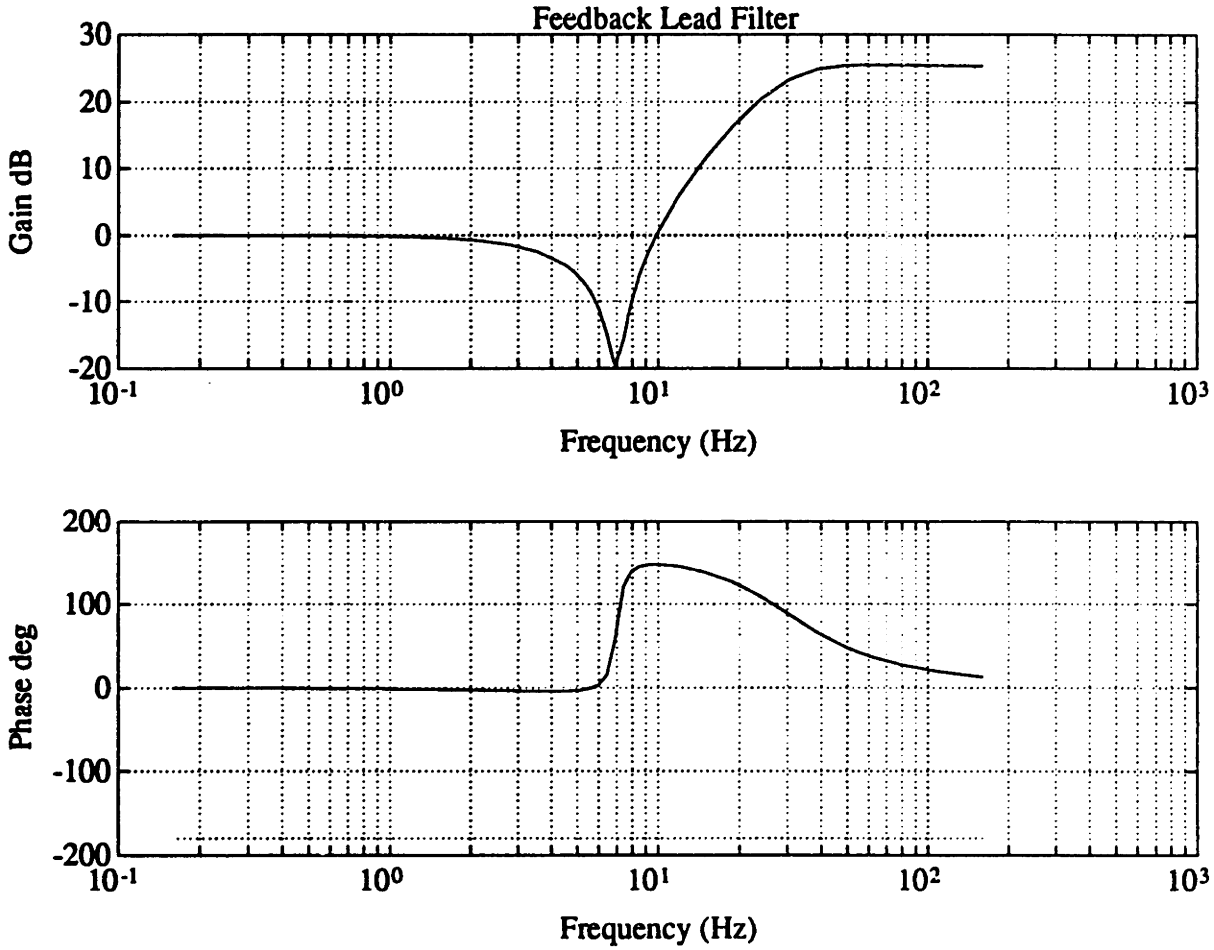

Figure 2-25: Frequency Response of Lead Filter in ILCU [2]

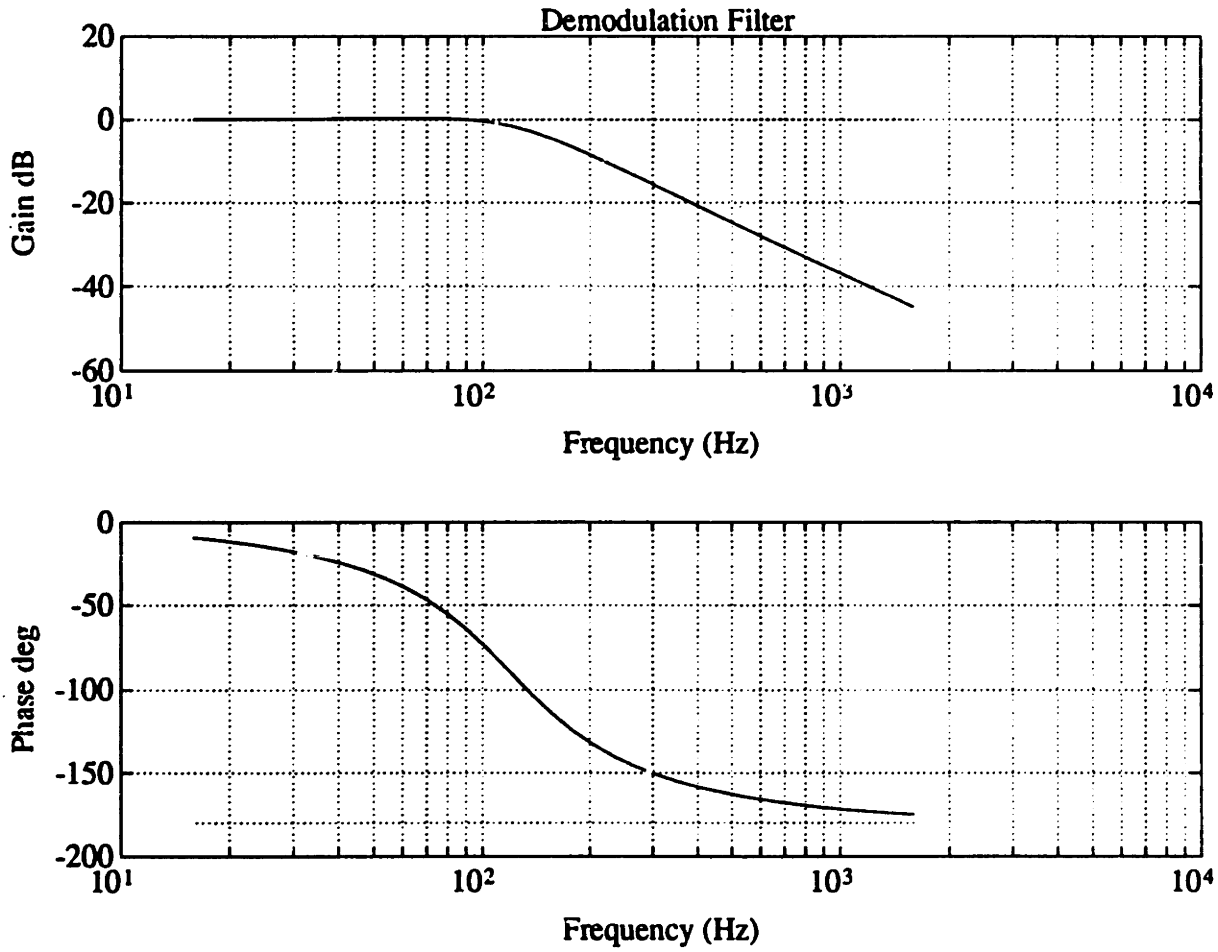

Figure 2-26: Frequency Response of Feedback Information Demodulation Filter [2]

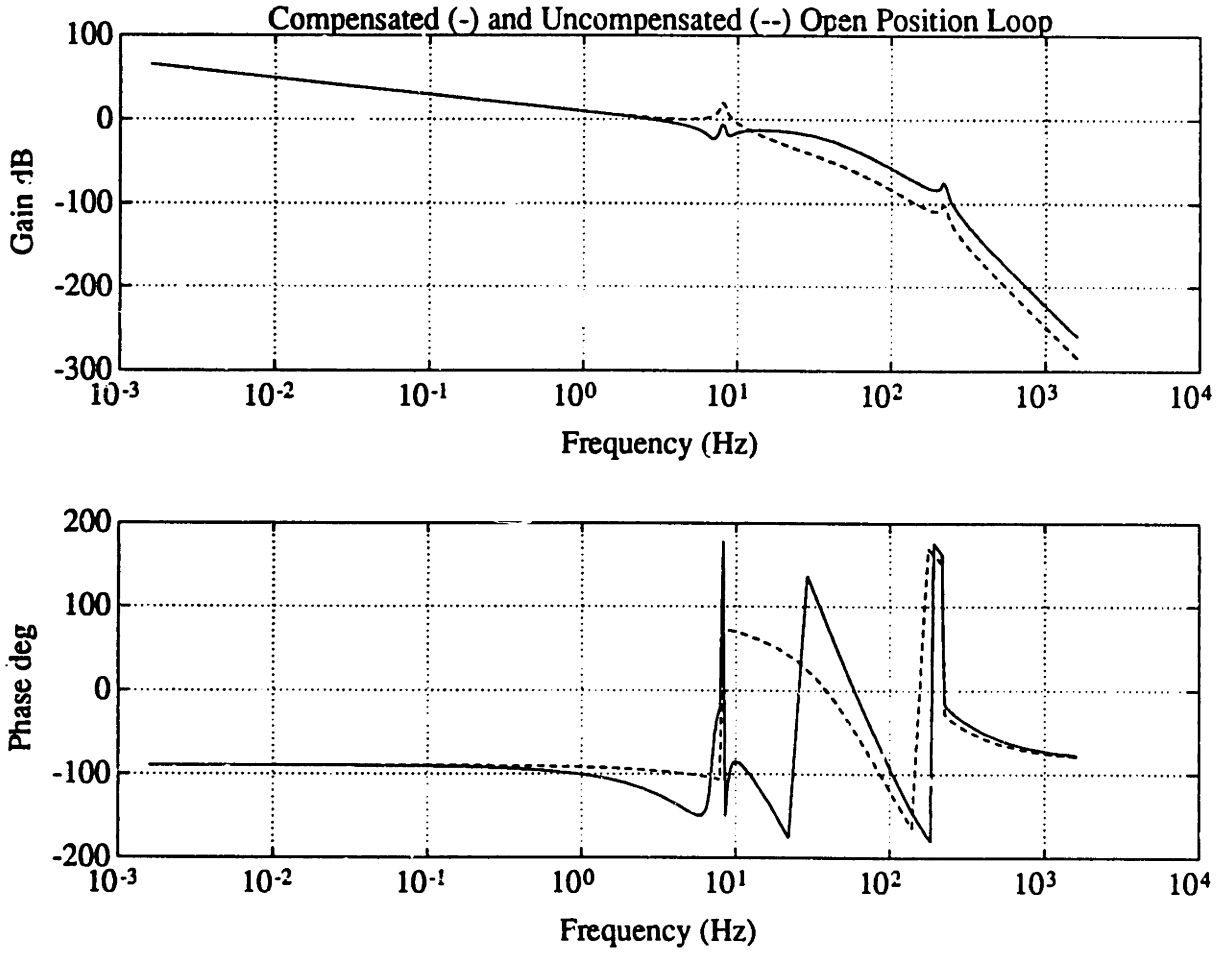

Figure 2-27: Frequency Response of Linearized TVC Open Position Loop with and without ILCU Lead and Notch Compensation

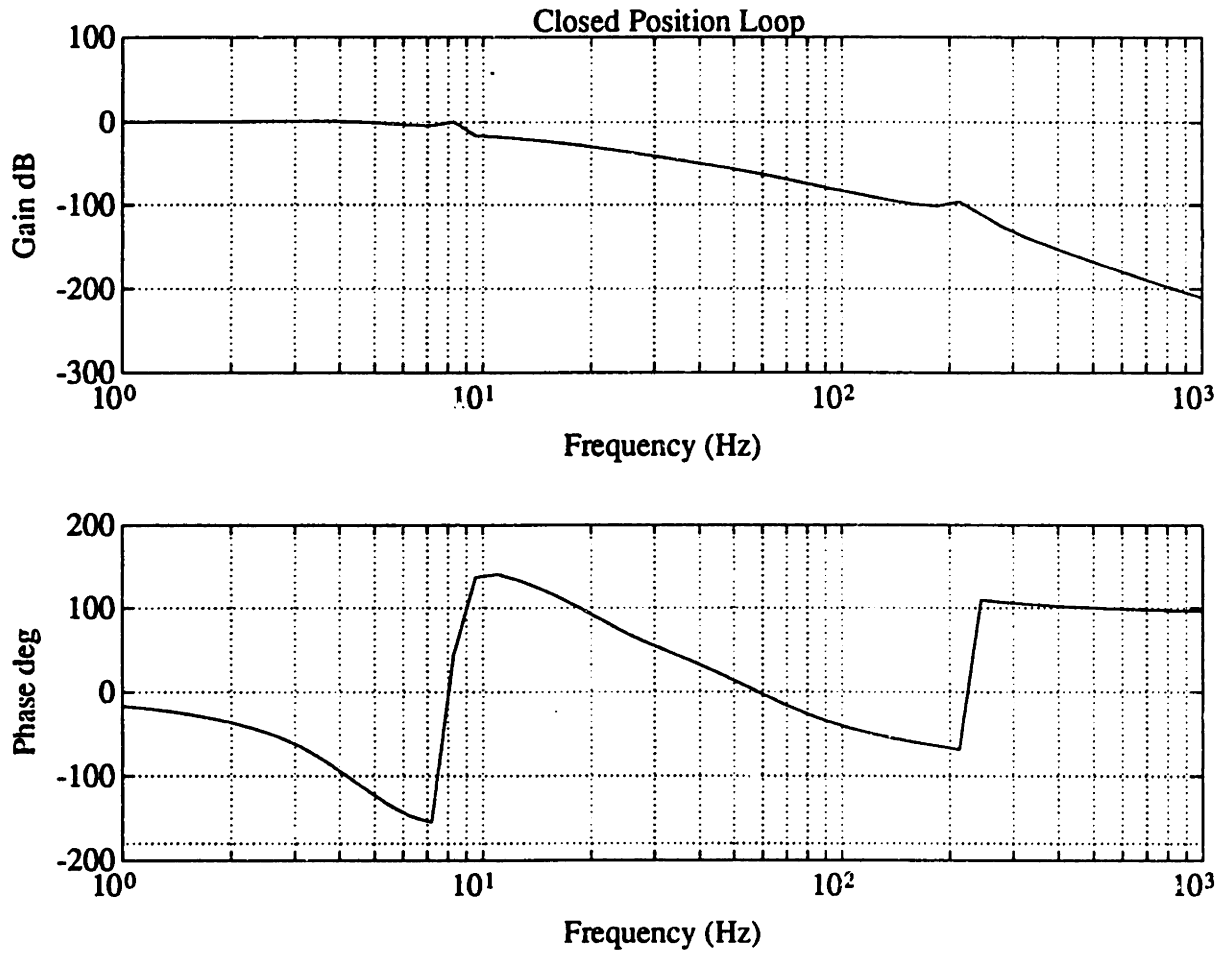

Figure 2-28. Frequency Response of Linearized Closed TVC Position Loop with ILCU Filters and Compensation

uration included: (1) the ILCU; (2) a nozzle with a 227,233 in · lbs · sec^2 moment of inertia [17, 44]; and (3) the decreased flow capacity of the Electric Hydraulic Power Unit (EHPU), which is functionally equivalent to the Ground Hydraulic Unit (GHU). The supply pressure characteristics as a function of flow demand for each GHU is depicted in Figure 2-29. A maximum of only QOG' = 135 cis is available at P_o [26, 16]. Because of the shortage of flow capacity, an accumulator has been added to the ground supply system. An accumulator is the hydraulic equivalent of an electric capacitor. No model of the accumulator/GHU supply system has been developed to date, and it is believed that the dynamic characteristics of the accumulator have affected the test results slightly. For the torque equations, the best match with measured data was obtained assuming the maximum value of unpressurized flexseal stiffness, $K_s = 309,000$ in · lbs per degree, and the maximum value for the combined compliance for the test configuration, $K_c = 388,000$ lbs per in [44].

Figures 2-30 through 2-32 depict TVC response to one-half Hz and one Hz sine waves in the tilt direction. Three system variables are plotted: nozzle position, actuator pressure, and servovalve current. The model is quite good, but there is a slight offset in Pathfinder current levels, shown in Figure 2-32. The large current indicated by the Pathfinder data at zero nozzle velocity is probably due to a bias in the data acquisition system.

Figures 2-33 through 2-35 depict TVC response to a one-half Hz square wave in the tilt direction. Again the correlation is quite good except the simulated tilt position in Figure 2-33 starts to lag just slightly behind the Pathfinder tilt position after a short slew.

2.8 Flight System Performance Requirements

The TVC design is required to meet the following requirements as of May 2, 1990 [28]. For step responses of less than 1.5 degrees, the performance must be consistent with the frequency response criteria defined by a bounded region of the Bode plot shown in Figure 2-36. For step responses larger than 1.5 degrees, the TVC system

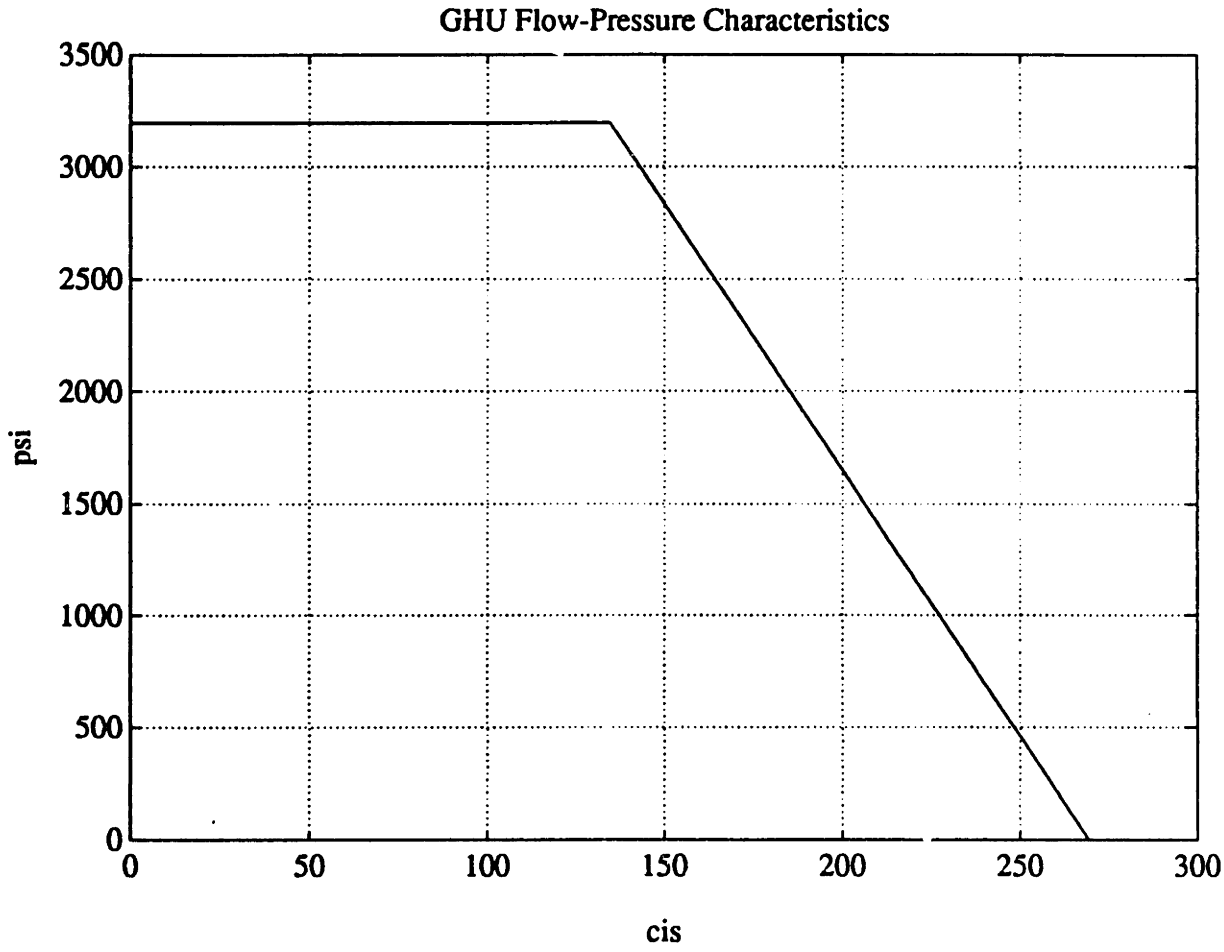

Figure 2-29: Approximate Flow-Pressure Characteristics of Ground Hydraulic Unit (GHU) Without Accumulator [26, 16]

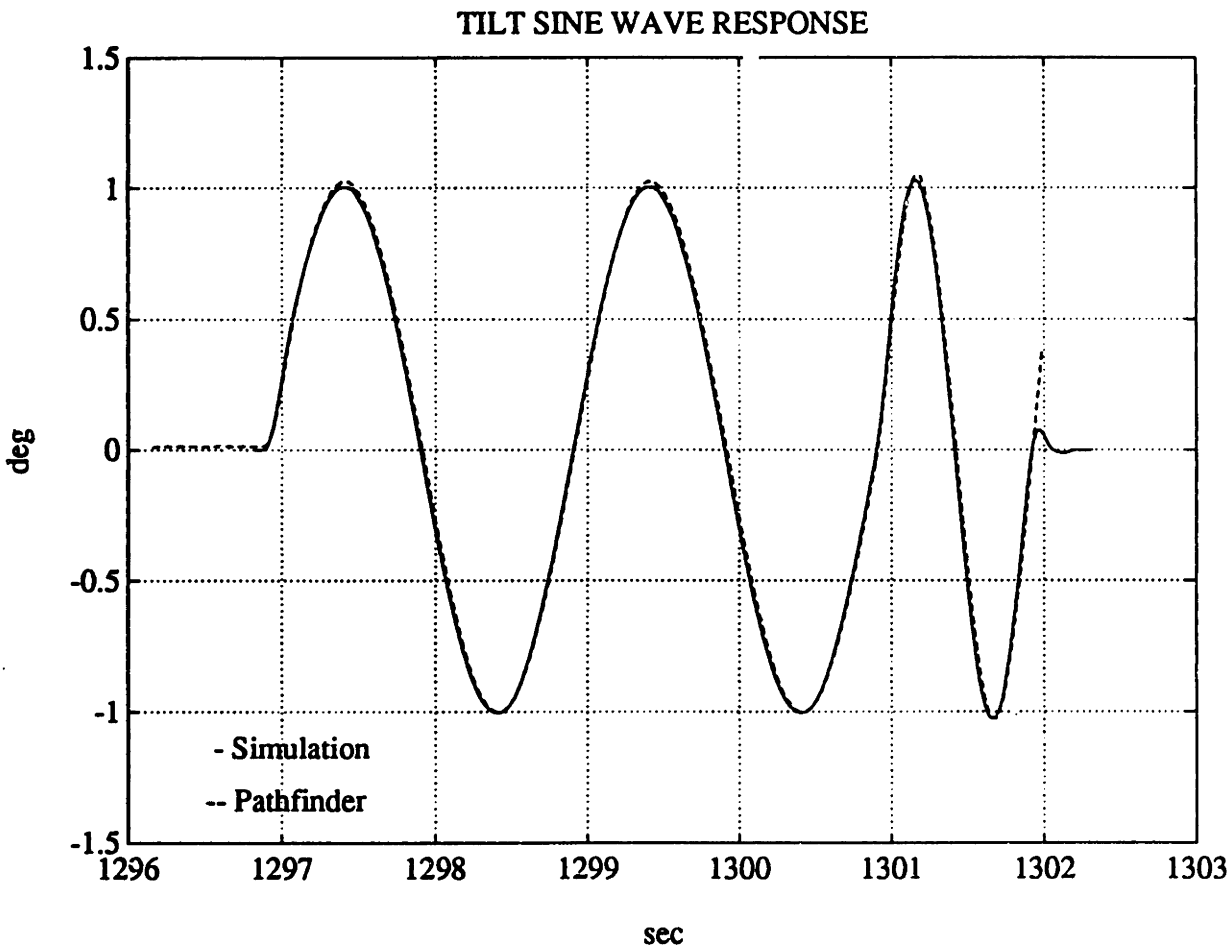

Figure 2-30: Comparison of Simulated [22, 20] and Measured [43] Nozzle Position in Response to One-Half and One Hz Sine Waves in the Tilt Direction Using the ILCU.

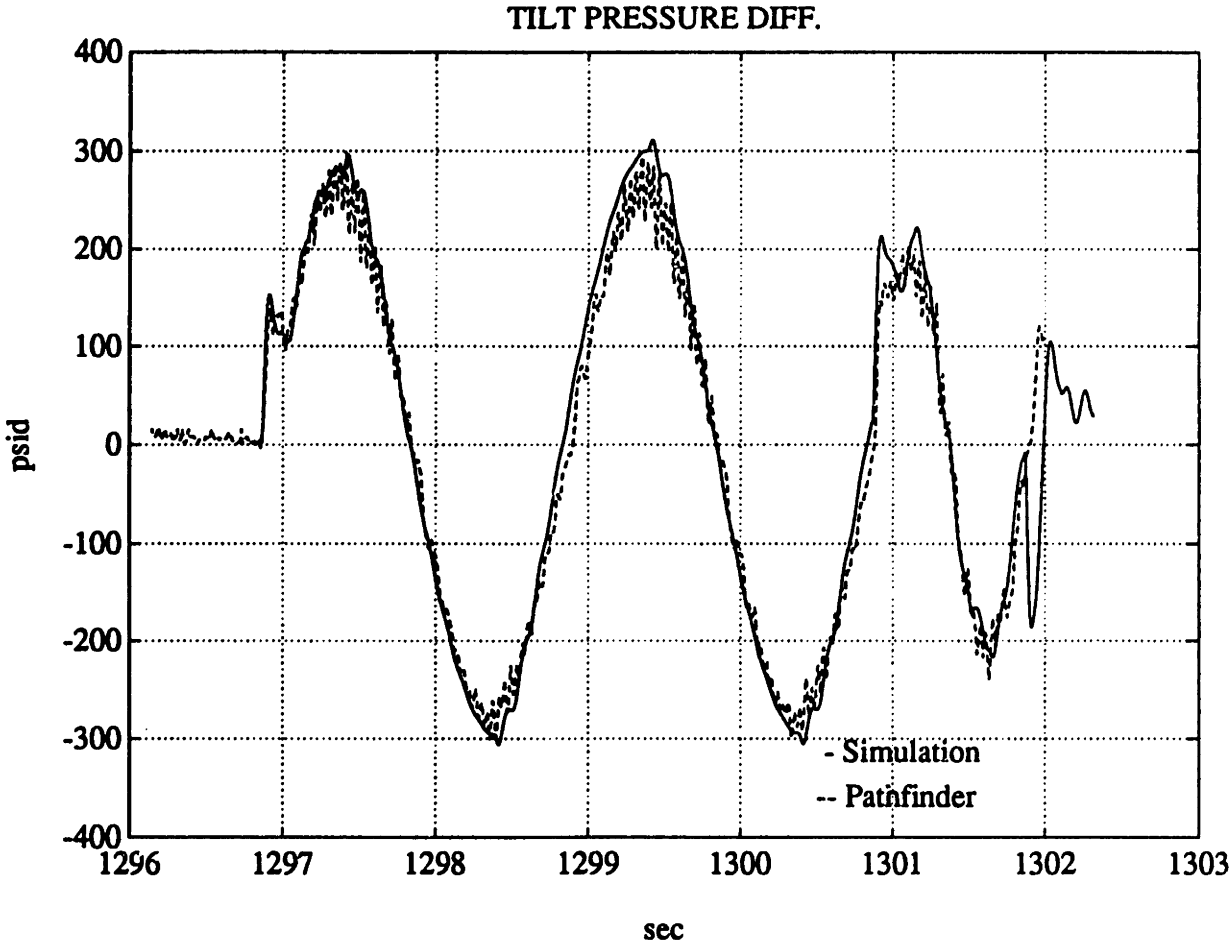

Figure 2-31: Comparison of Simulated [22, 20] and Measured [43] Actuator Differential Pressure in Response to One-Half and One Hz Sine Waves in the Tilt Direction Using the ILCU.

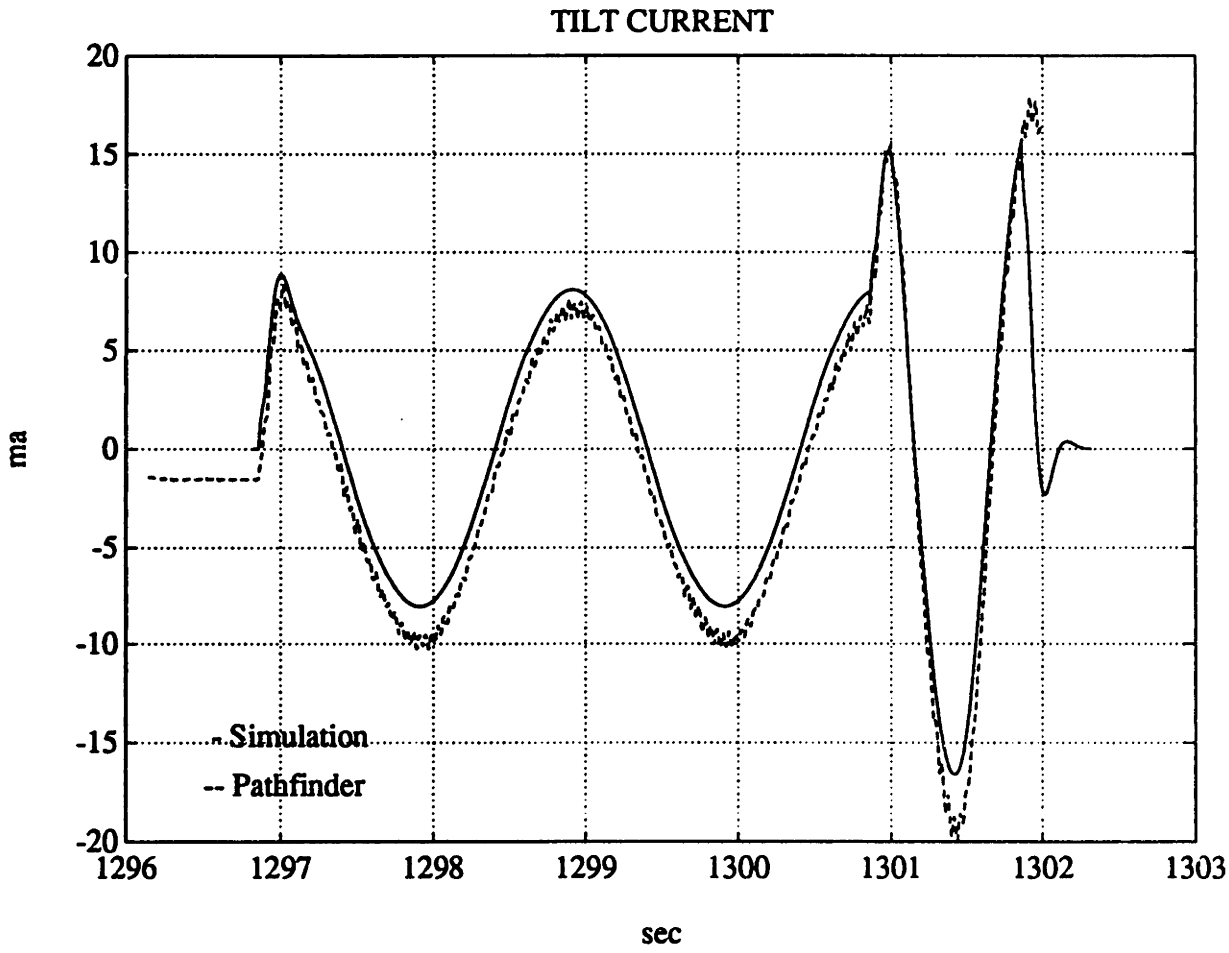

Figure 2-32: Comparison of Simulated [22, 20] and Measured [43] Servovalve Current in Response to One-Half and One Hz Sine Waves in the Tilt Direction Using the ILCU.

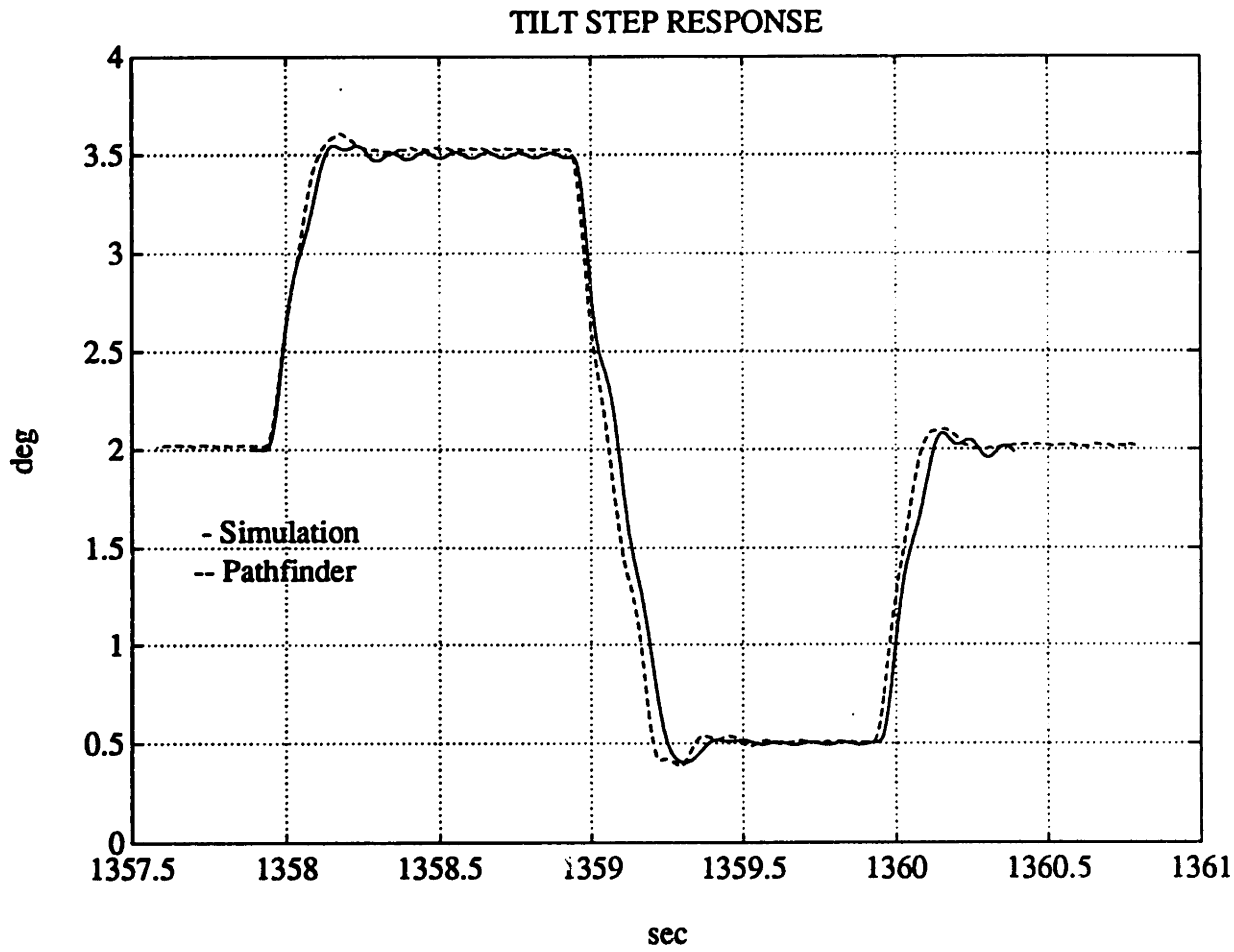

Figure 2-33: Comparison of Simulated [22, 20] and Measured [43] Nozzle Position Response to One-Half Hz Square Wave in the Tilt Direction Using the ILCU.

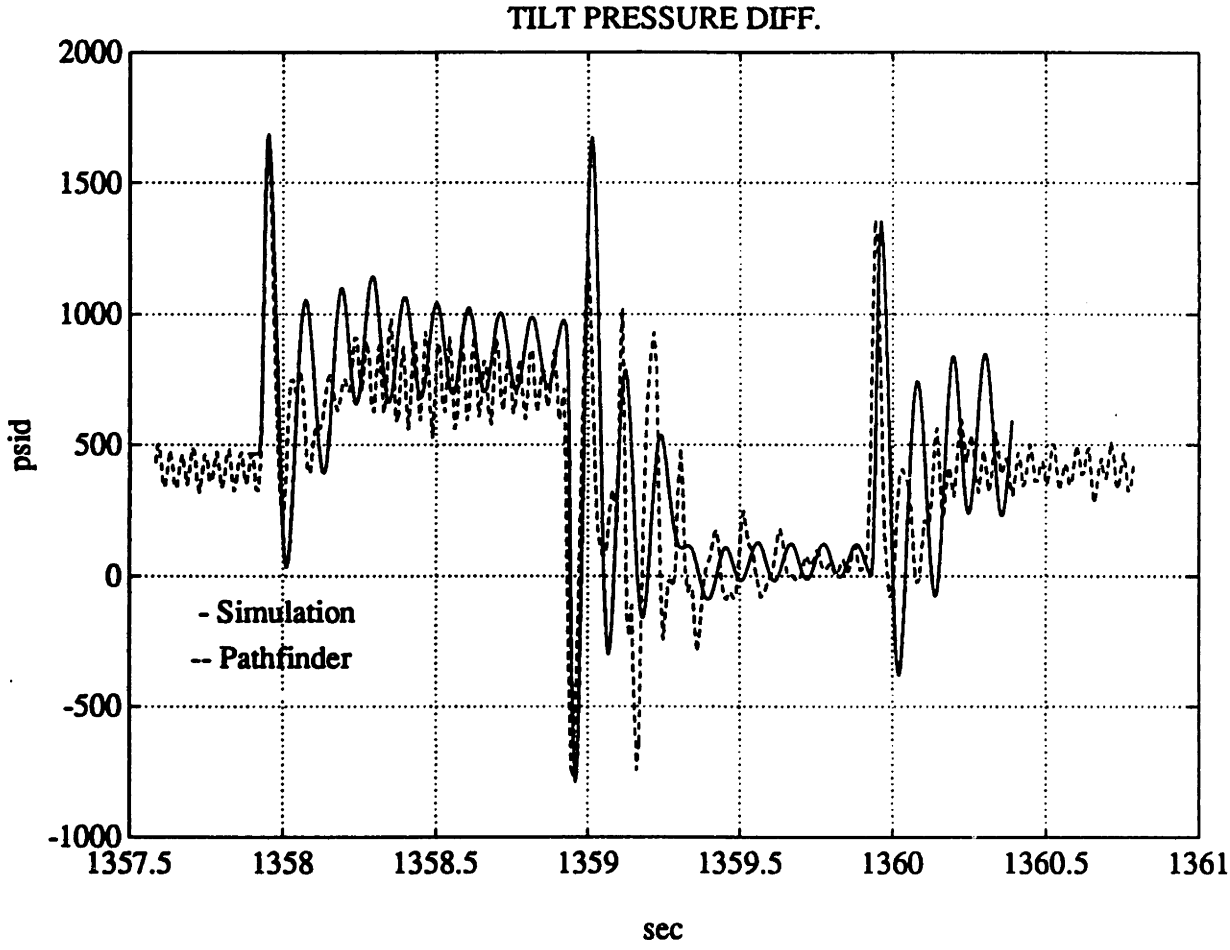

Figure 2-34: Comparison of Simulated [22, 20] and Measured [43] Actuator Differential Pressure in Response to One-Half Hz Square Wave in the Tilt Direction Using the ILCU.

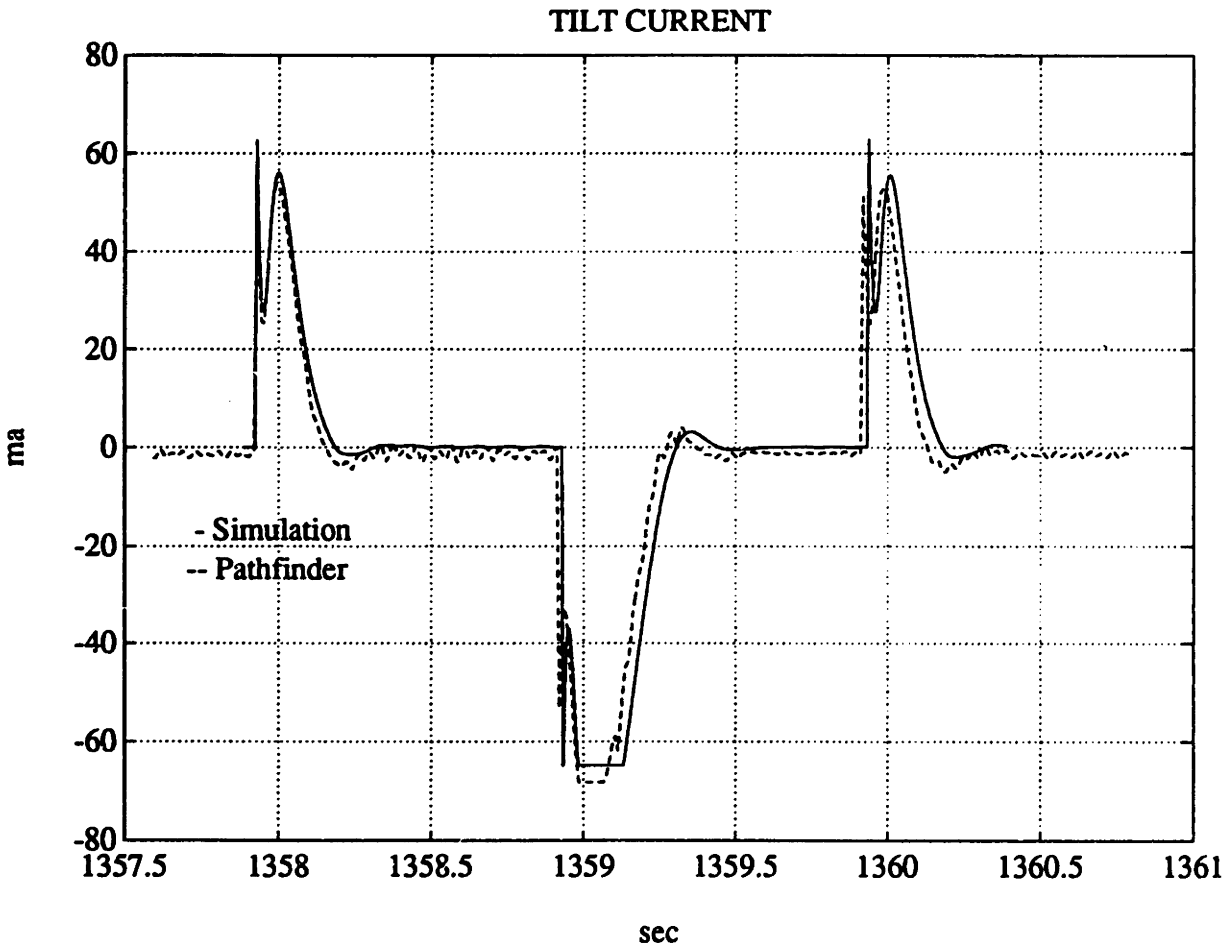

Figure 2-35: Comparison of Simulated [22, 20] and Measured [43] Servovalve Current in Response to One-Half Hz Square Wave in the Tilt Direction Using the ILCU.

must reach ten percent of the commanded deflection in 100 ms. It must vector from ten to ninety percent of the commanded deflection at an average rate no less than 7.5 degrees per second. And it must vector from ninety to ninety-nine percent of the commanded deflection in 150 ms. Overshoot must be within the bounds shown in Figure 2-37. The response must settle to with ±2% of the final angle 0.2 seconds after reaching ninety percent of the commanded deflection. The overall position accuracy needs to be ±0.23 degrees.

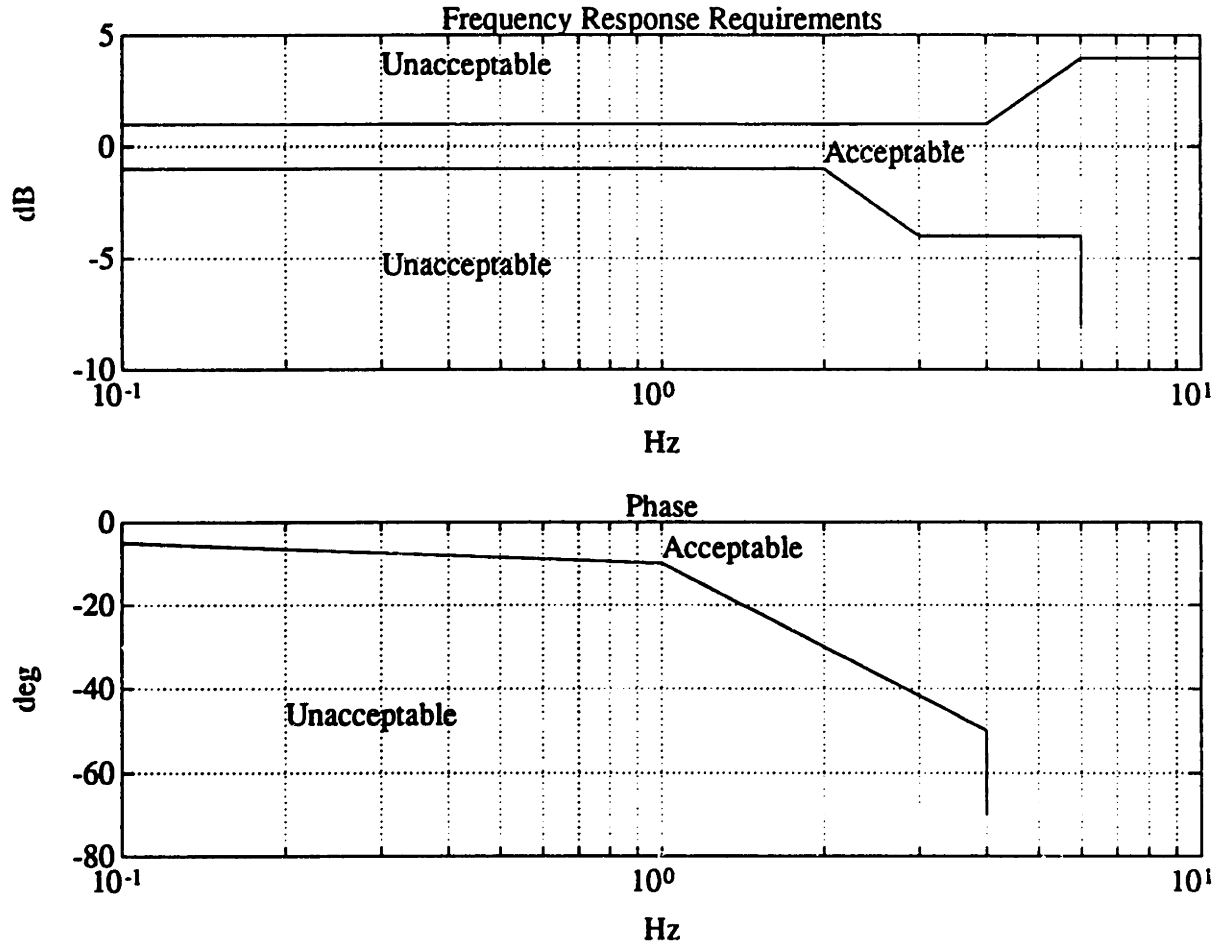

Figure 2-36: Acceptable Frequency Response Regions for the TVC System [28]

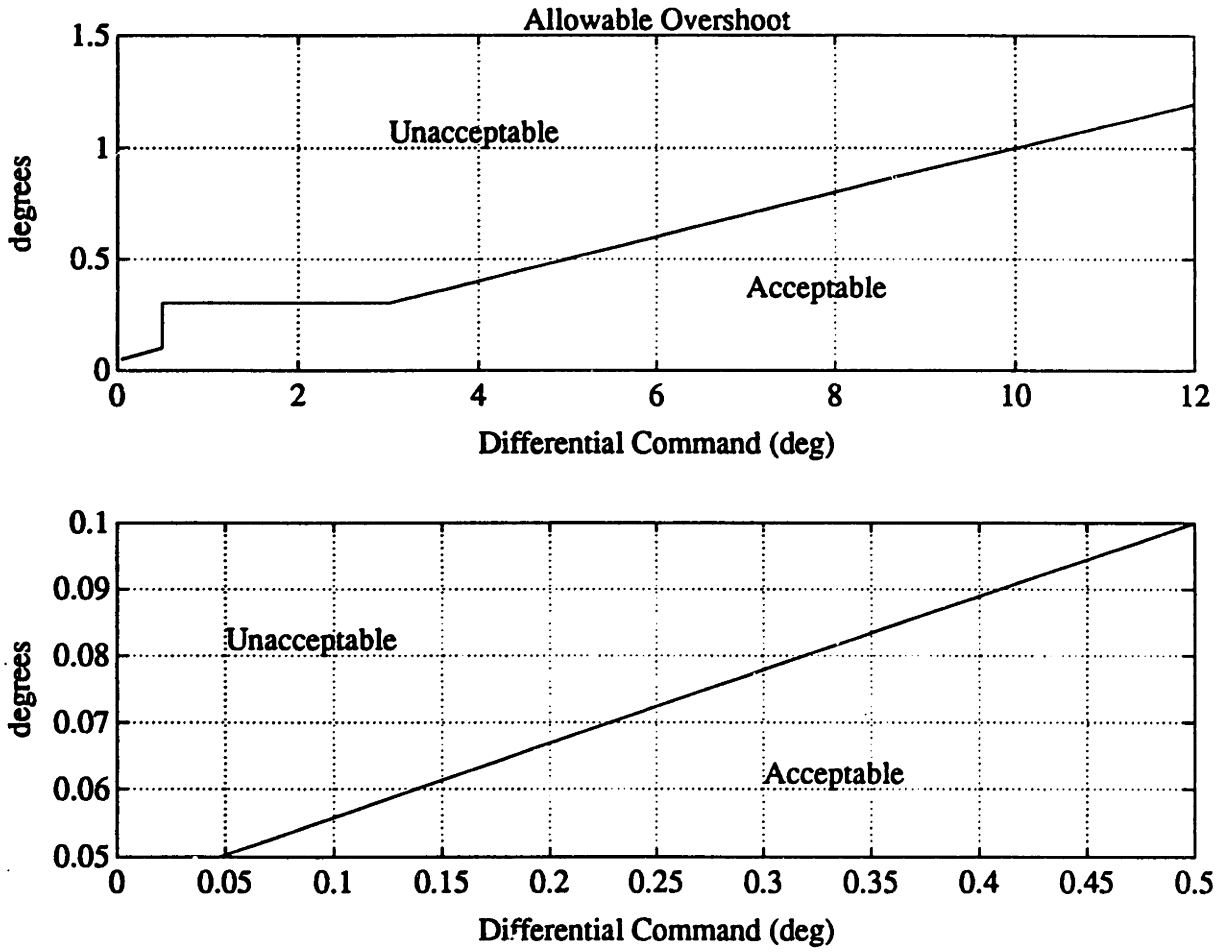

Figure 2-37: Acceptable Amounts of Step Response Overshoot for the TVC System [28]

Chapter 3

Linearization and Classical Control

The development of appropriate linearizing approximations to facilitate classical controller design for the SRMU TVC is the topic of this chapter. Transfer functions are derived, and classical Bode analysis of the current controller design is presented.

3.1 Nozzle Torques

For SRMU test configuration analyses, it is valid to assume zero internal and external aerotorques as well as zero heat shield torque.

The flexseal torque is the only other external torque on the system, and only its stiffness component is included in the linear model. For small nozzle deflections, the effect of the Dahl solid friction model is an apparent increase in stiffness, so this can be taken into consideration in the linearization by increasing the spring constant appropriately. Some attempts at flexseal linearization have used a constant damping coefficient derived from the variable damping coefficient of the alternative flexseal solid friction model used prior to the Dahl model. The analysis of the previous chapter has shown that the alternative model does not adequately describe the flexseal, so no

flexseal damping is included in this linearization.

$$K_o = K_s + K_{fdg} \tag{3.1}$$

$$B_o = 0 \tag{3.2}$$

where:

K_{fdg} = Apparent Increase in Flexseal Stiffness Due to Small Nozzle Deflections

K_o = Linearized External Torque Spring Constant

K_s = Flexseal Spring Constant

B_o = Linearized External Torque Damping Coefficient

3.2 Piston Movement and Pressure

The equation for piston movement, Equation 2.15, is almost linear, except for the coulomb friction, which is neglected. The equations for pressure gradients, Equations 2.16 and 2.17, are almost linear, except for the volumes in the denominator, which are a function of piston position. The assumption that the piston is close to center position is made so the volumes are set constant and equal to half the total displacement of the piston:

$$V_e = \frac{1.1 \cdot \mathrm{XTS} \cdot A_p}{2} \tag{3.3}$$

The two pressure gradient equations are also condensed into a single equation for the change in load pressure, $P_L \equiv P_1 - P_2$. The individual pressures cannot be used in a linearized model because their differential equations require individual flow equations, which require inequalities based on the servovalve spool position. Using the load pressure technique allows the use of the average flow, Q_L, also referred to as the load flow.

$$\frac{dP_L}{dt} = \frac{2 \cdot \mathrm{AE} \cdot \beta_e}{V_e}(Q_L - C_{im}P_L - \frac{C_{em}P_L}{2} - A_p\frac{dX_p}{dt}) \tag{3.4}$$

Note that a differential equation for load force can be obtained simply by multi-

plying Equation 3.4 by the piston area A_p:

$$\frac{dF_L}{dt} = \frac{4 \cdot \mathtt{AE} \cdot \beta_e \cdot A_p}{1.1 \cdot \mathtt{XTS}}\left(\frac{Q_L}{A_p} - \frac{C_{im}P_L}{A_p} - \frac{C_{em}P_L}{2A_p} - \frac{dX_p}{dt}\right) \tag{3.5}$$

The integral of Equation 3.5 is an expression in the form of Hooke's Law. Thus, the approximate equivalent stiffness of the oil in the actuator chambers is:

$$K_2 = \frac{4 \cdot \mathtt{AE} \cdot \beta_e \cdot A_p}{1.1 \cdot \mathtt{XTS}} \tag{3.6}$$

3.3 Fluid Flow

The four equations for flow to/from each piston chamber, Equation 2.28, can be condensed into a single equation [33]. If the load pressure is defined as:

$$P_L \equiv P_1 - P_2 \tag{3.7}$$

and the following assumption (which is true for incompressible fluid) is made:

$$P_s + P_r \approx P_1 + P_2 \tag{3.8}$$

then it follows that:

$$P_1 \approx \frac{P_s + P_r + P_L}{2} \tag{3.9}$$

$$P_2 \approx \frac{P_s + P_r - P_L}{2} \tag{3.10}$$

Defining the load flow as the average flow:

$$Q_L \equiv \frac{Q_1 + Q_2}{2} \tag{3.11}$$

then the four forms of Equation 2.28 can be approximated by the following single equation for load flow:

$$Q_L \approx \frac{\texttt{CO} \cdot \texttt{WS} \cdot x_{sy}\sqrt{P_s - \frac{x_{sy}}{|x_{sy}|}P_L)}}{\sqrt{1 + \texttt{RCW} \cdot x_{sy}^2}} \tag{3.12}$$

Linearization of the hydraulic flow characteristics is completed by the definition of the valve coefficients. The flow gain is defined by:

$$K_q \equiv \frac{\partial Q_L}{\partial x_{sy}} \tag{3.13}$$

while the flow-pressure coefficient is defined by:

$$K_c \equiv -\frac{\partial Q_L}{\partial P_L} \tag{3.14}$$

Therefore,

$$\delta Q_L \approx K_q \delta x_{sy} - K_c \delta P_L \tag{3.15}$$

The linearized analysis of the TVC hydraulic servo must assume perturbations around the equilibrium point $x_{sy} = 0$, $P_L = 0$ where:

$$K_q \approx \texttt{CO} \cdot \texttt{WS}\sqrt{P_s} \tag{3.16}$$

$$K_c \approx 0 \tag{3.17}$$

Linearization around points $x_{sy} = 0$, $P_L \neq 0$ is impossible because Equation 3.12 is discontinuous. Use of the usual linear time-invariant (LTI) stability analysis methods around points $x_{sy} \neq 0$ is invalid because these are not equilibrium points, and linear time-varying systems are derived from such linearizations.

3.4 Supply Pressure

Supply pressure must be assumed constant in order to maintain linearity.

$$P_s = P_o \tag{3.18}$$

3.5 Servovalve

The second-order servovalve model presented in the previous chapter is nearly linear except for three components, which are simply neglected in the linearization. These include first-stage flow saturation, first-stage flow threshold, and spool displacement saturation. The servovalve model then reduces to a second-order system with a natural frequency of $\omega_n/2\pi = 51.7$ Hz, a damping ratio ζ of 0.667, and a steady state gain of 0.00148 inches per milliamp.

$$\frac{x_{sy}(s)}{I(s)} = \frac{0.00148}{\frac{s^2}{\omega_n^2} + \frac{2\zeta s}{\omega_n} + 1} \tag{3.19}$$

Figure 3-1 shows the frequency response of the linearized servovalve.

3.6 Flight Loop Closure Unit

A linear system with constant coefficients is typically described by the standard state-space equations [30, 25]:

$$\dot{X} = A_{plt}X + B_{plt}I_c \tag{3.20}$$

$$Y = C_{plt}X + D_{plt}I_c \tag{3.21}$$

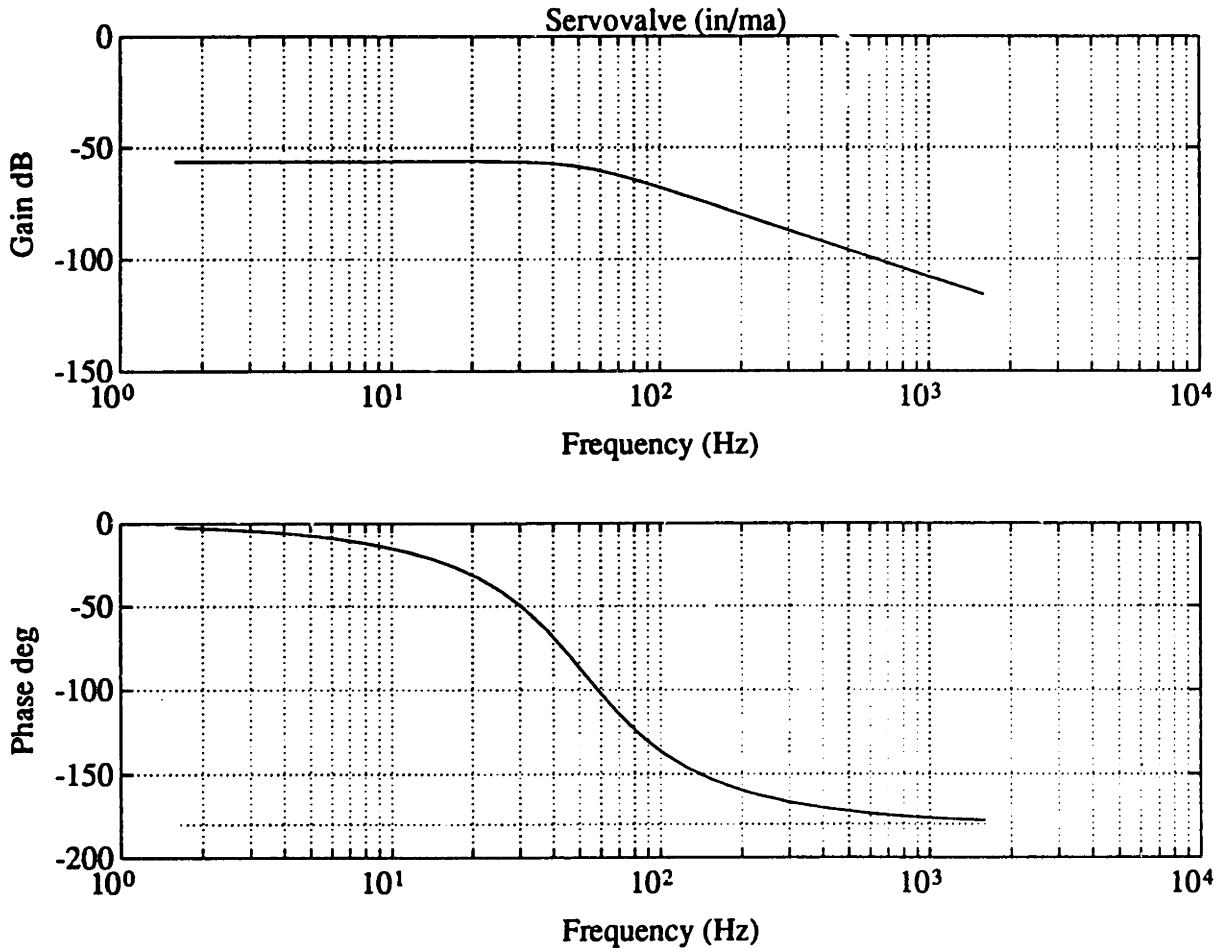

Figure 3-1: Frequency Response of Linearized TVC Jet Deflector Servovalve

The linearized TVC model in this chapter can be represented in standard state-space form with the following substitutions:

$$X = \begin{bmatrix} P_L \\ dX_p \\ X_p \\ d\theta \\ \theta \\ Q_a \\ X_s \end{bmatrix} \tag{3.22}$$

$$A_{plt} = \begin{bmatrix} 0 & \frac{-K_2}{A_p} & 0 & 0 & 0 & 0 & \frac{K_2 K_{qc}}{A_p^2} \\ \frac{A_p}{M_p} & \frac{-B_{fa}}{M_p} & \frac{-K_e}{M_p} & \frac{B_{fa}L}{M_p} & \frac{K_e L}{M_p} & 0 & 0 \\ 0 & 1 & 0 & 0 & 0 & 0 & 0 \\ 0 & \frac{B_{fa}L}{J} & \frac{K_e L}{J} & \frac{-(B_{fa}L^2+B_o)}{J} & \frac{-(K_e L^2+K_o)}{J} & 0 & 0 \\ 0 & 0 & 0 & 1 & 0 & 0 & 0 \\ 0 & 0 & 0 & 0 & 0 & \frac{-1}{\tau} & \frac{-K_{v1}K_q}{\tau} \\ 0 & 0 & 0 & 0 & 0 & \frac{\mathrm{NTM}}{A_1} & \frac{-Q_{xo}}{A_1} \end{bmatrix} \tag{3.23}$$

$$B_{plt} = \begin{bmatrix} 0 \\ 0 \\ 0 \\ 0 \\ 0 \\ \frac{K_q}{\tau} \\ 0 \end{bmatrix} \tag{3.24}$$

$$C_{plt} = \begin{bmatrix} C_{plt1} \\ C_{plt2} \end{bmatrix} = \begin{bmatrix} 0 & 0 & 0 & 0 & \frac{180}{\pi} & 0 & 0 \\ 1 & 0 & 0 & 0 & 0 & 0 & 0 \end{bmatrix} \tag{3.25}$$

$$D_{plt} = 0 \tag{3.26}$$

The FLCU contains two feedback loops, an inner pressure feedback loop, and an outer position feedback loop. Input-output transfer functions for the two loops can be derived from the above state space equations. If the transfer function $H_1(s)$ such that

$$H_1(s) = \frac{P_L(s)}{I_c(s)} \tag{3.27}$$

is desired, it can be easily determined from Equations 3.20 and 3.21 that

$$H_1(s) = C_{plt2}^T \left[sI - A_{plt}\right]^{-1} B_{plt} + D_{plt} \tag{3.28}$$

And similarly, the transfer function for $\theta(s)/I_c(s)$ is:

$$H_2(s) = \frac{\theta(s)}{I_c(s)} = C_{plt1}^T \left[sI - A_{plt}\right]^{-1} B_{plt} + D_{plt} \tag{3.29}$$

The block diagram for the linearized TVC system with appropriate filters and compensation in the FLCU is shown in Figure 3-2 [45]. The frequency response of the dynamic pressure feedback filter, which includes a differentiator and a pole at 3 Hz, is shown in Figure 3-3. The frequency response of the pressure transducer filter, which includes poles at 167 Hz and 169 Hz, is shown in Figure 3-4. The frequency response of the valve driver, which is a second-order low-pass filter with poles at 395 Hz and a damping ratio of 1.581, is shown in Figure 3-5. The frequency response of the open pressure loop with filters is shown in Figure 3-6. Approximately 9 dB of gain margin and 50 degrees of phase margin are evident.

The frequency response of the closed pressure loop with filters is shown in Figure 3-7. The closed pressure loop with filters is appended with the transfer function for $\theta(s)/P_L(s)$ as well as the transfer function for a feedback information demodulation filter. The demodulation filter is a second order low pass filter with poles at 120 Hz and a damping ratio of 0.6. The frequency response of the demodulation filter, which is the same filter used in the ILCU, is shown in Figure 2-26. The outer position loop

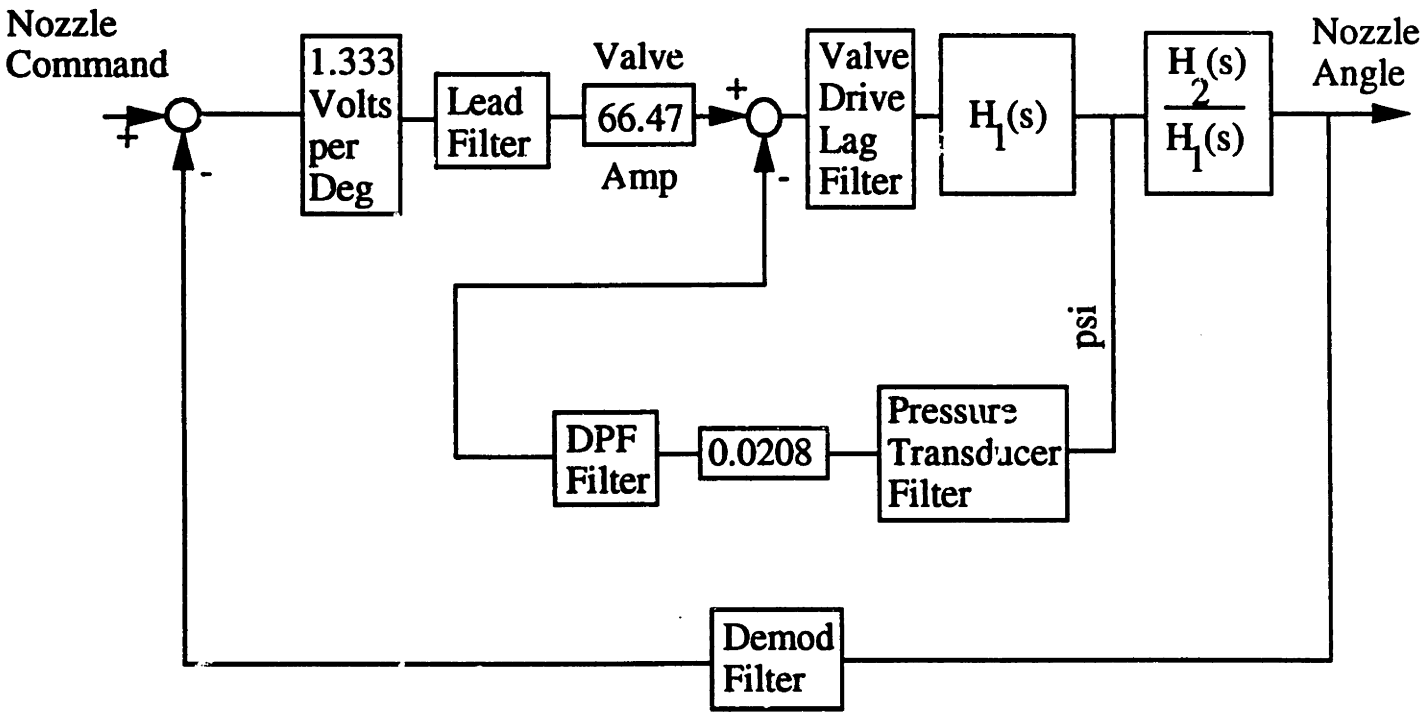

Figure 3-2: Block Diagram of TVC System with FLCU [45]

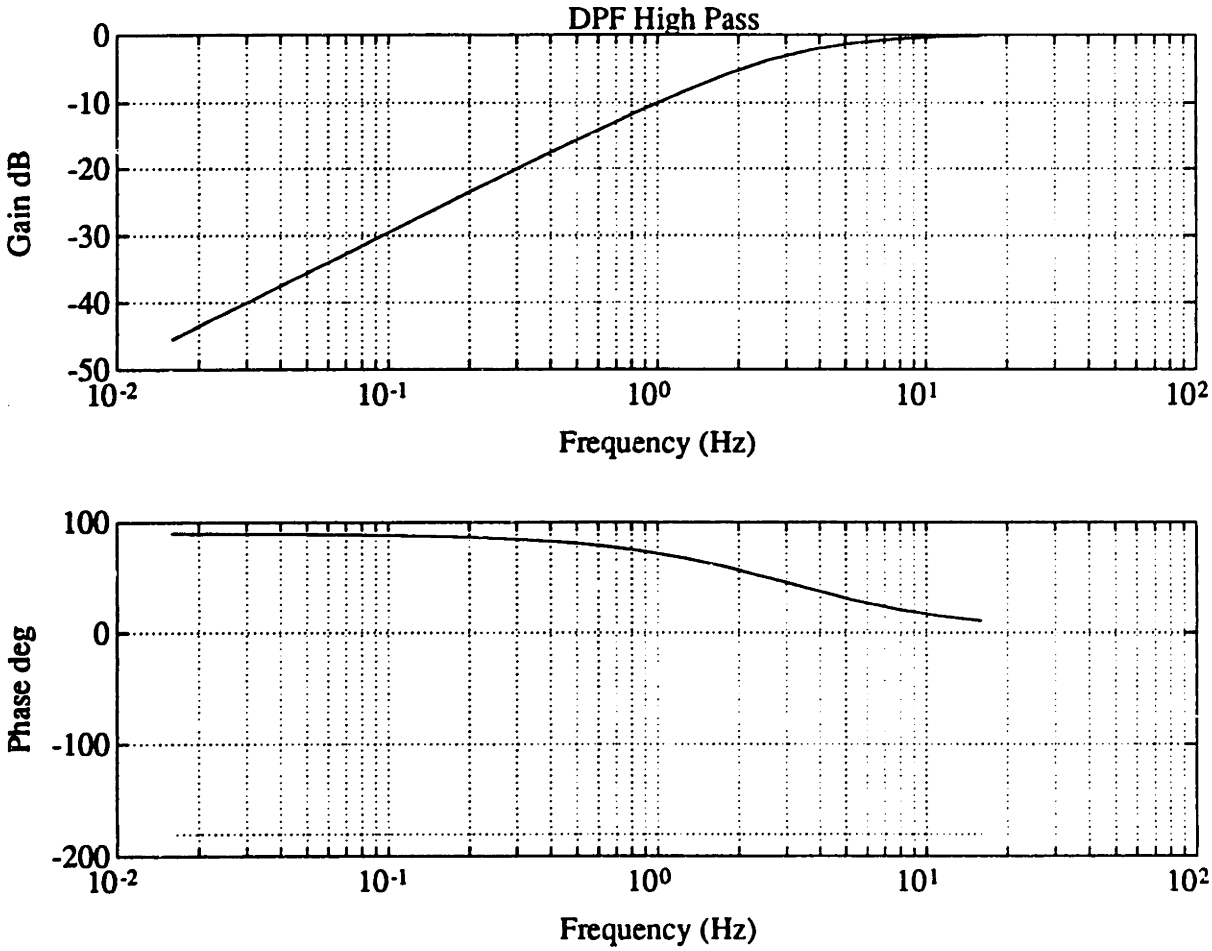

Figure 3-3: Frequency Response of FLCU Dynamic Pressure Feedback High Pass Filter [45]

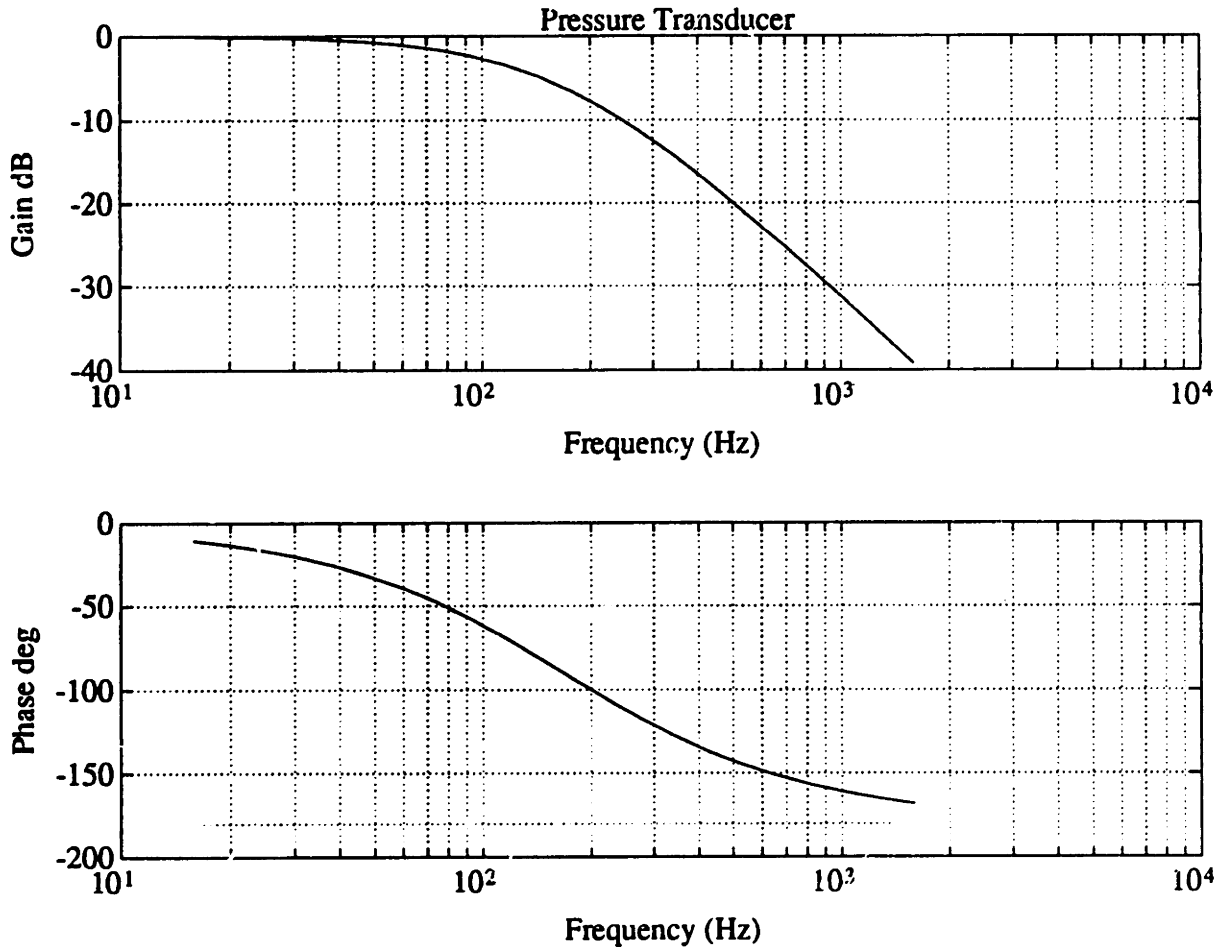

Figure 3-4: Frequency Response of FLCU Pressure Transducer Low-Pass Filter [45]

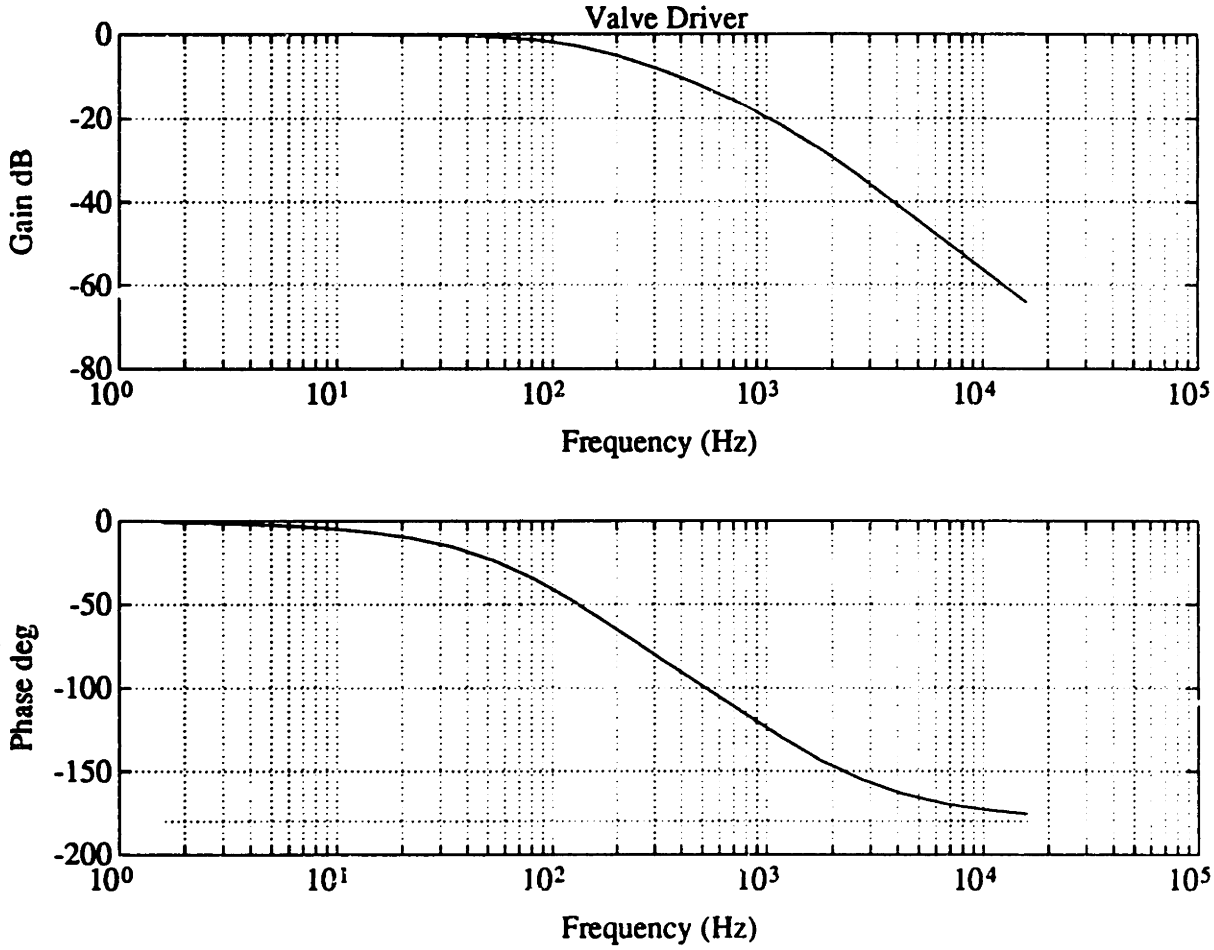

Figure 3-5: Frequency Response of FLCU Valve Driver Low-Pass Filter [45]

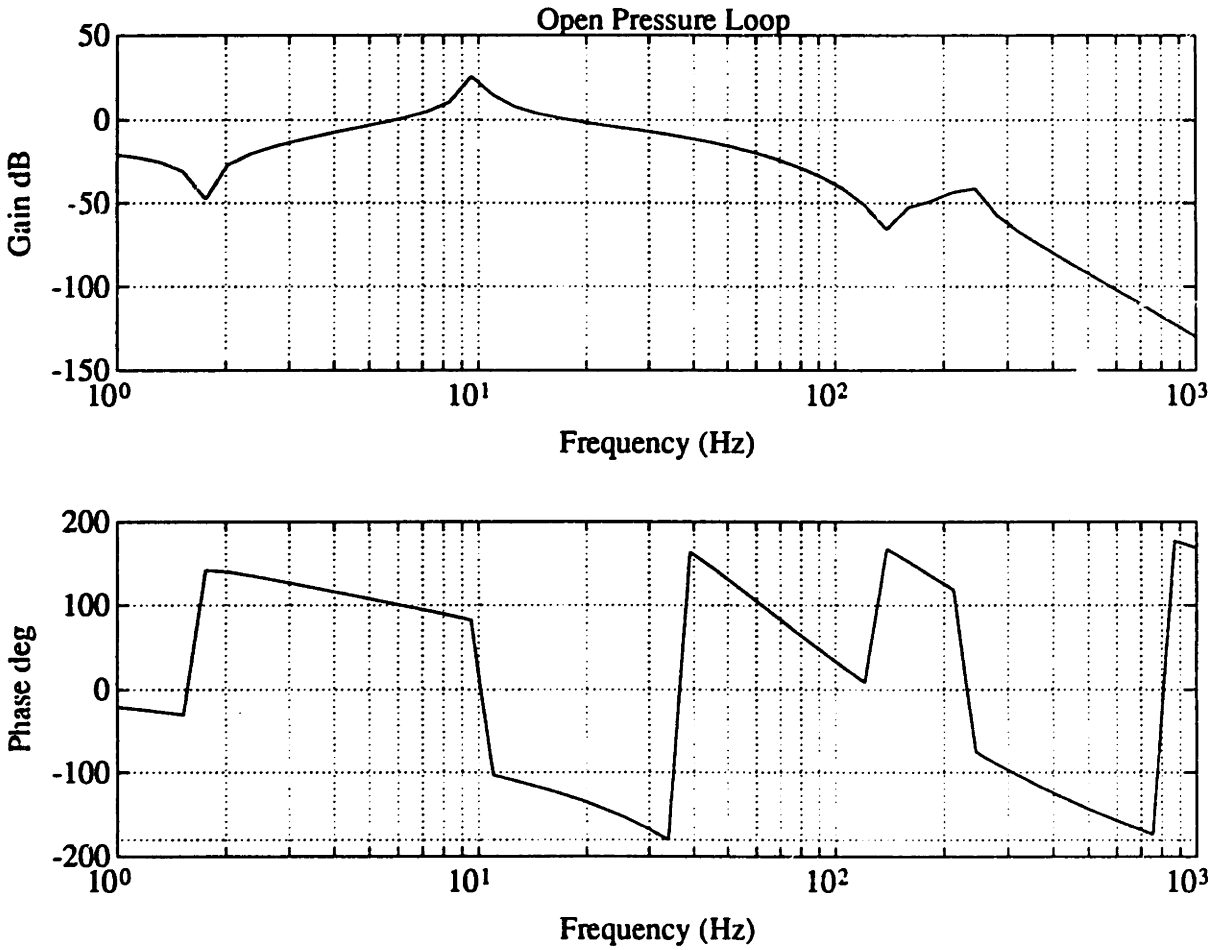

Figure 3-6: Frequency Response of Linearized Open TVC Pressure Loop with FLCU Filters

(with: (1) demodulation filter, and (2) closed inner or pressure loop with filters) is in turn compensated with a second order lead filter. The lead zeros are located at 10.46 Hz with a damping ratio of 0.759. The lead poles are located at 29.77 Hz with a damping ratio of 0.866. The frequency response of the lead compensator is shown in Figure 3-8. The frequency response of the open position loop (with (1) demodulation filter (2) closed inner or pressure loop with filters, and (3) lead compensation) is shown in Figure 3-9. The frequency response without (3) is also shown. Approximately 7 dB of gain margin and 48 degrees of phase margin are evident with compensation. The frequency response of the compensated closed position loop is shown in Figure 3-10. Referring to Figures 3-23 and 3-24, the linearized model demonstrates approximately 7 Hz more bandwidth than the nonlinear model.

3.7 Model Performance with Flight Loop Closure Unit

Figures 3-11 through 3-16 show the correlation between measured data from TVC checkout tests for Preliminary Qualification Motor One Prime (PQM-1') [46] and simulated results using the nonlinear hydraulic equations of Chapter 2 [24]. These tests consisted of a series of TVC vectoring excercises using the idle (not firing) SRMU on the test stand at Phillips Laboratory, Edwards Air Force Base, May 29, 1992. The test configuration included: (1) a nozzle with moment of inertia of close to the nominal 193,000 in $\cdot$ lbs $\cdot$ sec^2; (2) the Ground Hydraulic Unit with an accumulator, providing unknown flow capacity at a pressure of 3800 psi (the model used to match this particular set of test data assumed unlimited flow capacity); (3) the higher bandwidth (as compared to the ILCU) of the FLCU with dynamic pressure feedback. Recall that the ILCU uses a notch filter to cancel the nozzle natural frequency instead of DPF. For the torque equations, the best match with measured data was obtained assuming the maximum value of unpressurized flexseal stiffness, $K_s = 309,000$ in $\cdot$ lbs per degree, and the maximum value for combined compliance for the test configuration, $K_e = 388,000$ lbs per in [44].

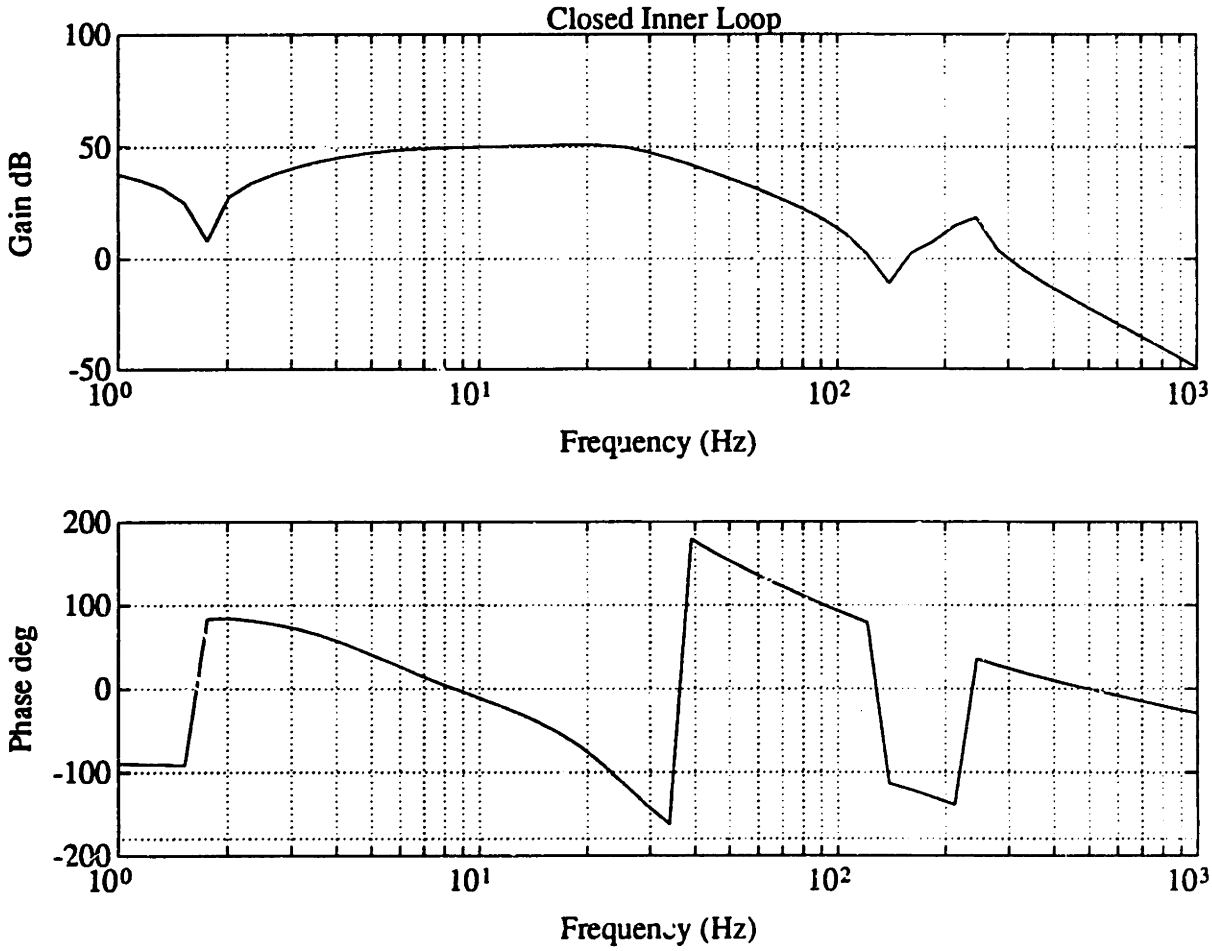

Figure 3-7: Frequency Response of Linearized Closed TVC Pressure Loop with FLCU Filters

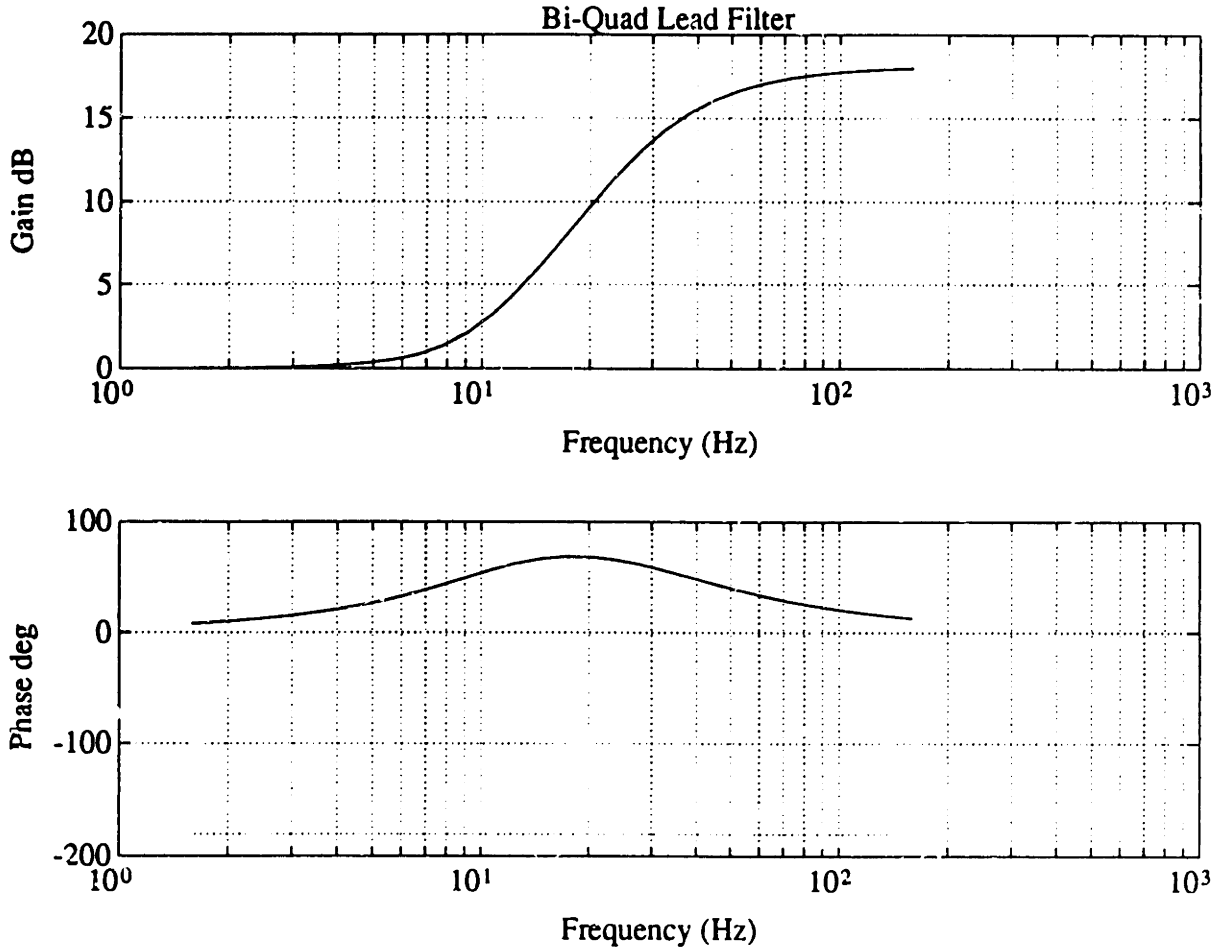

Figure 3-8: Frequency Response of FLCU Lead Filter [45]

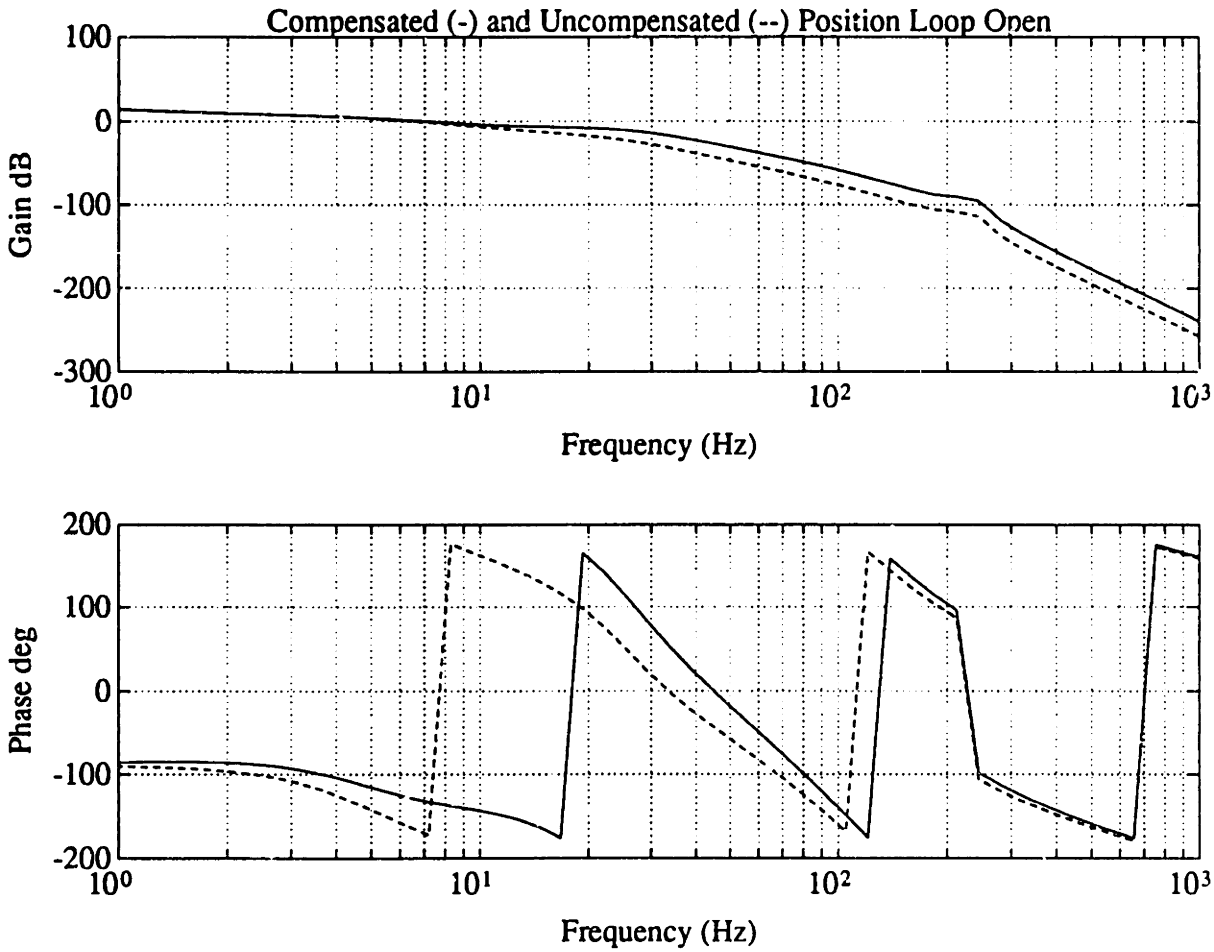

Figure 3-9: Frequency Response of Linearized Open TVC Position Loop with Demodulation Filter and FLCU Compensation As Well As Closed Inner Loop

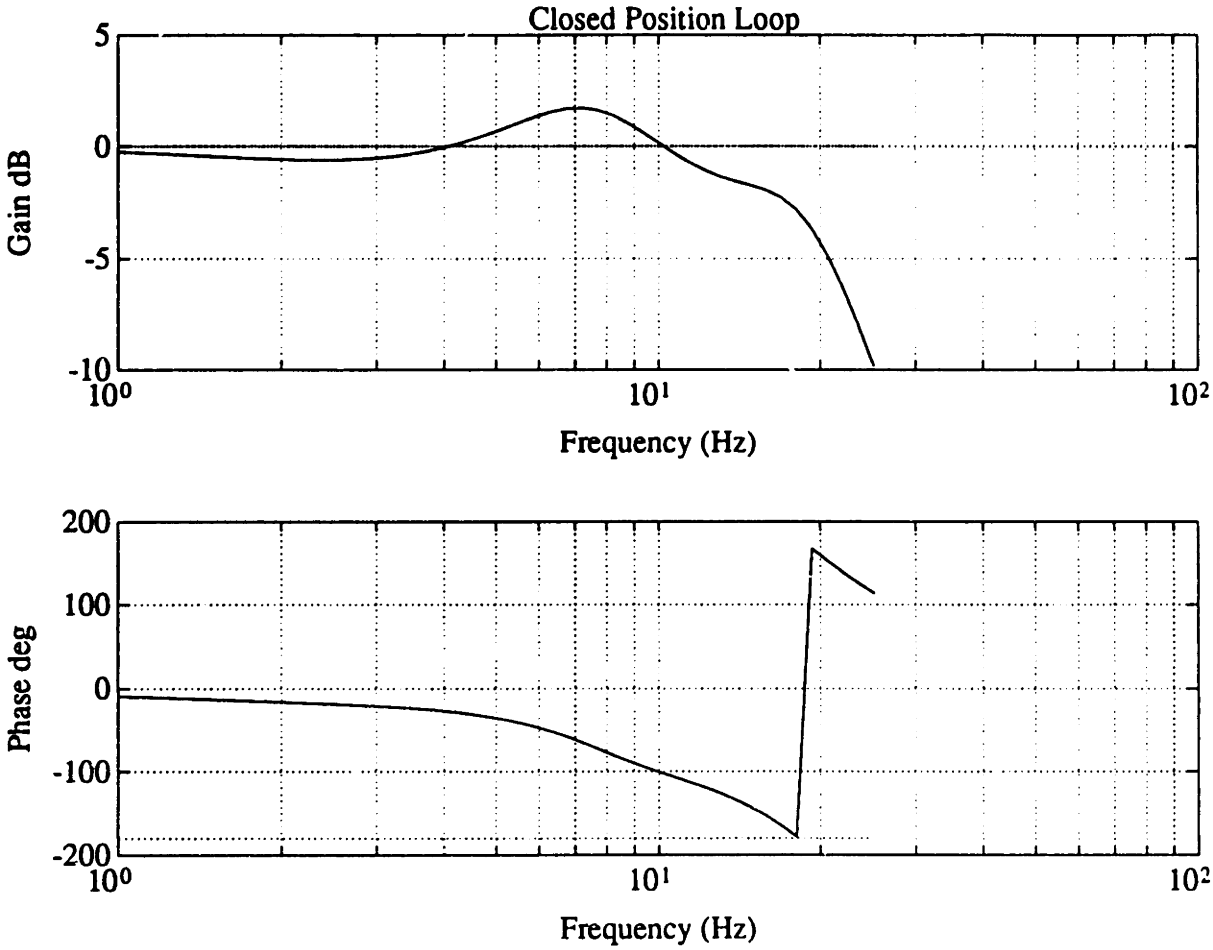

Figure 3-10: Frequency Response of Linearized Closed Loop TVC System with FLCU

Figures 3-11 through 3-16 depict TVC response to a 0.36 degree commanded rock sinusoid at 10 Hz, and a 0.3 degree commanded rock step. Pitch position, rock servovalve current, and rock actuator differential pressure are shown. In general the correlation is good except for some 27 Hz rock actuator current oscillations in the measured data of Figure 3-13 which the simulation was unable to duplicate. Oscillations at 27 Hz were also noticed in recent static firing tests and may indicate a potential SRMU structural/TVC instability in the system which is unmodeled [4, 31]. Measured data also indicates significant variations in the accumulator/GHU supply system between 3100 psi and 4200 psi. Figures 3-17 and 3-18 show the variations in supply pressure for the sinusoid and the step respectively [46]. This may be another source of discrepancies between simulated and measured data.

3.8 System Performance with Flight Loop Closure Unit

The natural frequency of the linearized TVC nozzle assembly is approximately [19]:

$$f_n = \frac{1}{2\pi}\sqrt{\left(\frac{L^2}{\frac{1}{K_2}+\frac{1}{K_e}} + \frac{180K_s}{\pi}\right)\frac{1}{J}} \tag{3.30}$$

The above equation is derived using a second-order approximation with the nozzle inertia and significant stiffness parameters.

The TVC system with the FLCU as defined in this chapter meets all contractors step and frequency response requirements if no external torques other than the flexseal are assumed. The step and frequency response requirements were outlined in Section 2.8. Figures 3-19 through 3-22 show 0.3, 1.0, 4.5, and 6.0 degree simulated step responses. Figures 3-23 and 3-24 show approximated frequency response curves from nonlinear simulations at discrete frequencies at amplitudes of 0.25 degree and 0.5 degree. These frequency response curves show approximately 7 Hz lower closed-loop bandwidth in the nonlinear system than Figure 3-10 shows in the linear system.

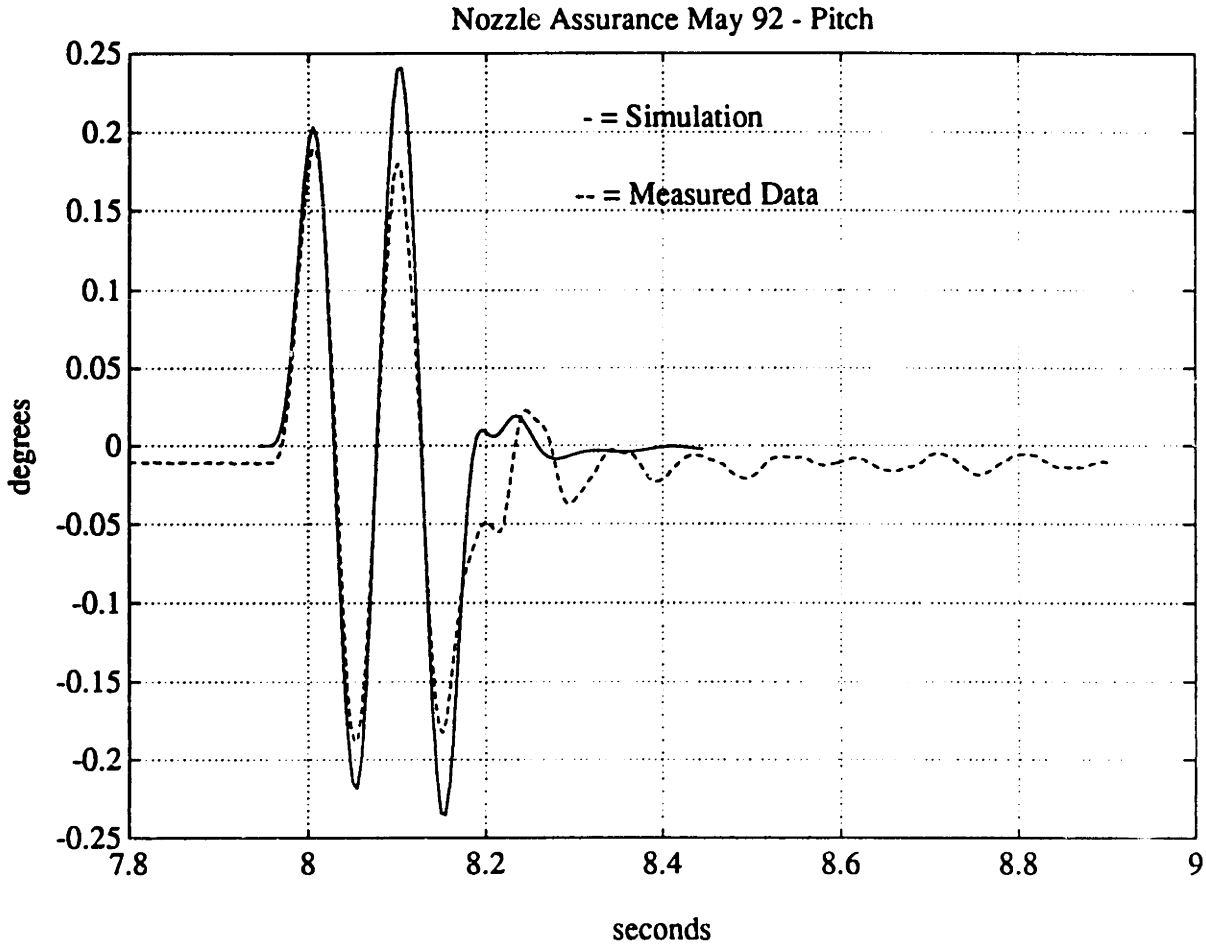

Figure 3-11: Comparison of Simulated [24] and Measured [46] Nozzle Position in Response to 10 Hz, 0.36 Degree Sine Waves in the Rock Direction Using the FLCU

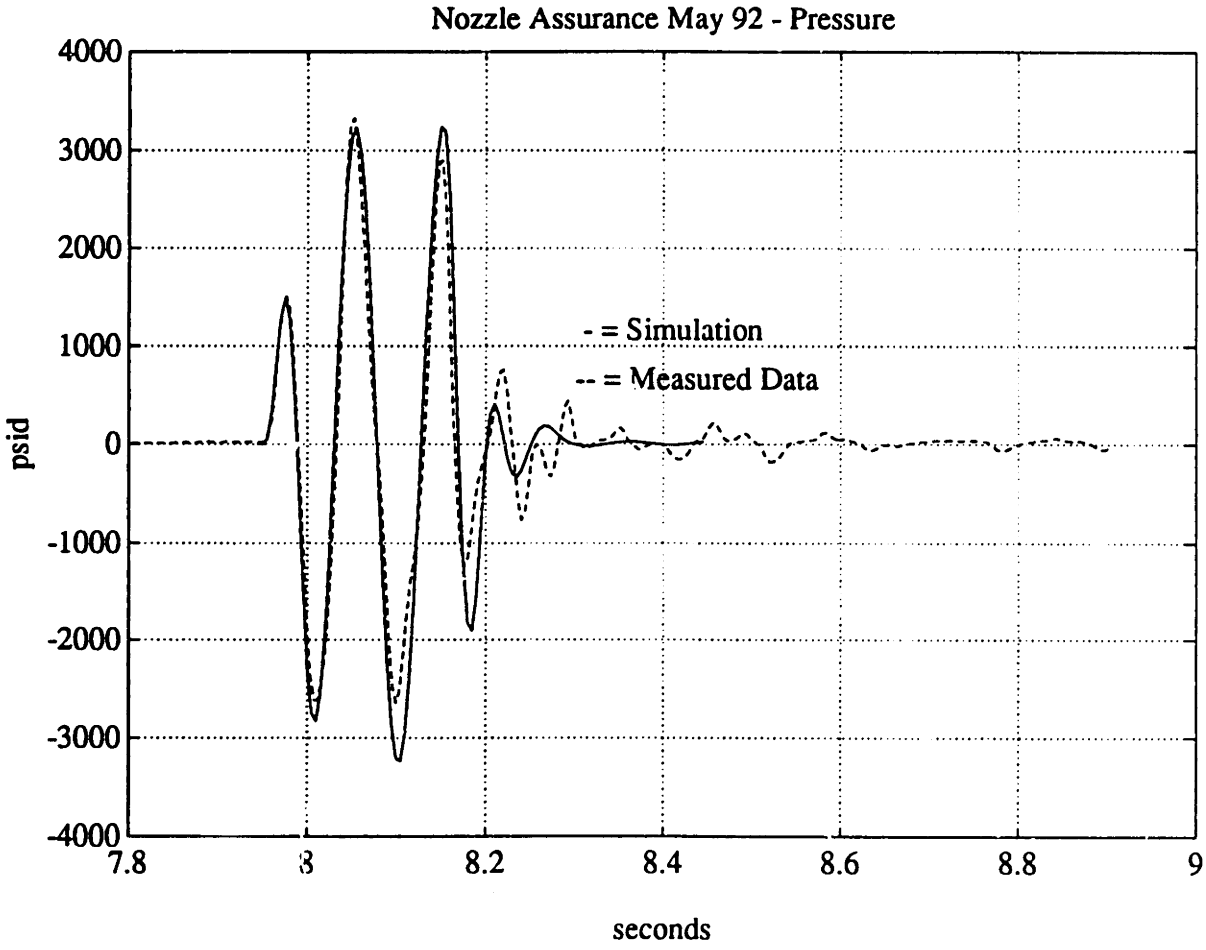

Figure 3-12: Comparison of Simulated [24] and Measured [46] Actuator Differential Pressure in Response to 10 Hz, 0.36 Degree Sine Waves in the Rock Direction Using the FLCU

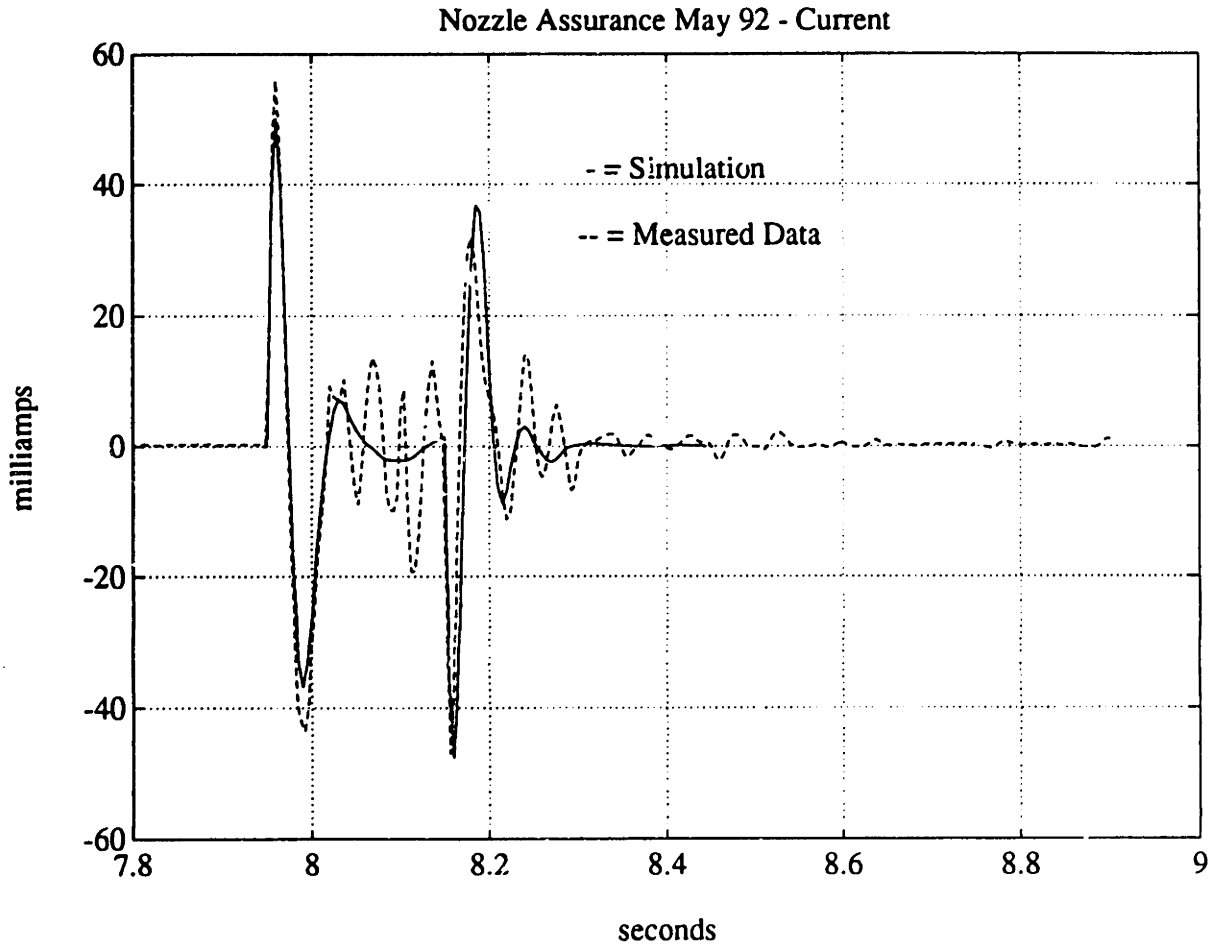

Figure 3-13: Comparison of Simulated [24] and Measured [46] Servovalve Current in Response to 10 Hz, 0.36 Degree Sine Waves in the Rock Direction Using the FLCU

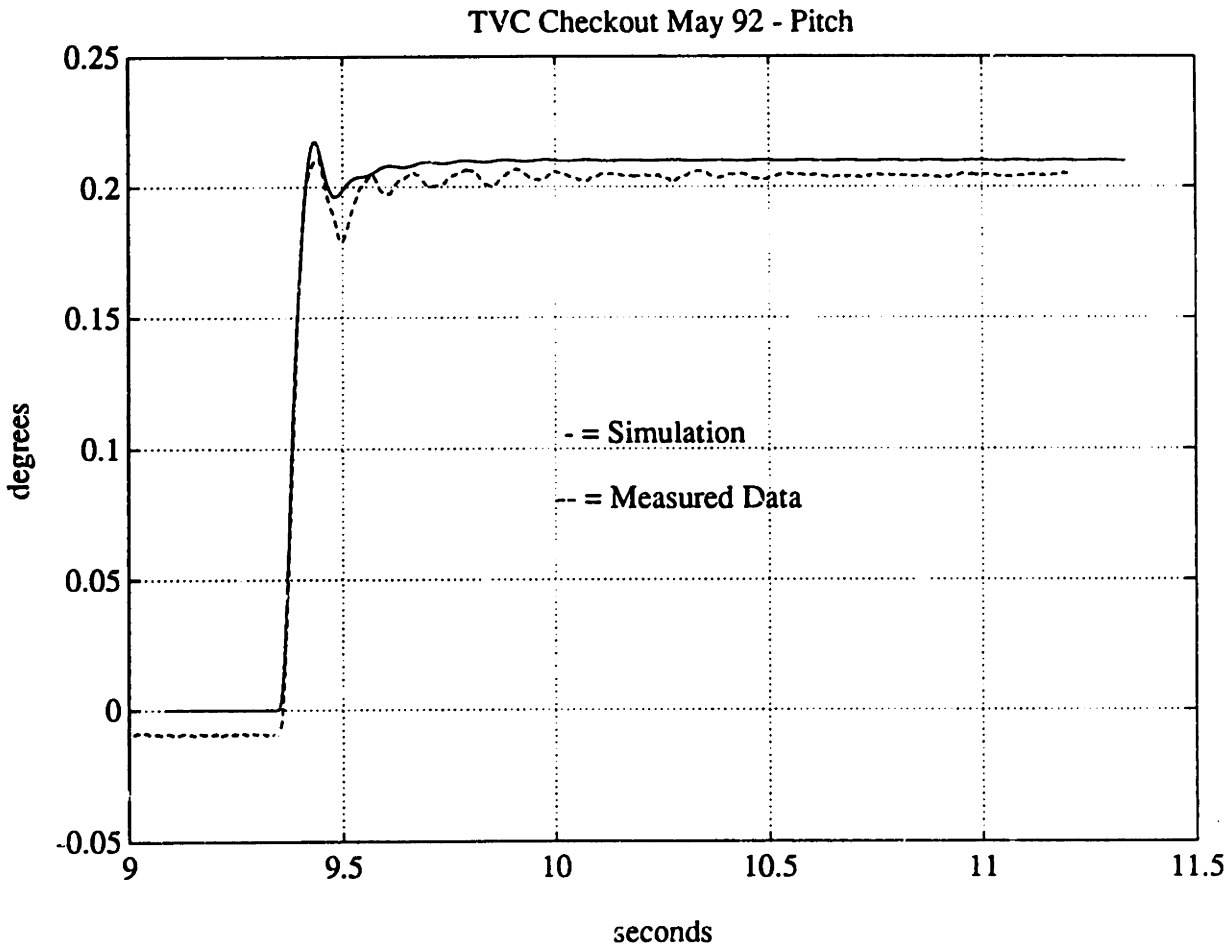

Figure 3-14: Comparison of Simulated [24] and Measured [46] Nozzle Position Response to 0.3 Degree Step in the Rock Direction Using the FLCU

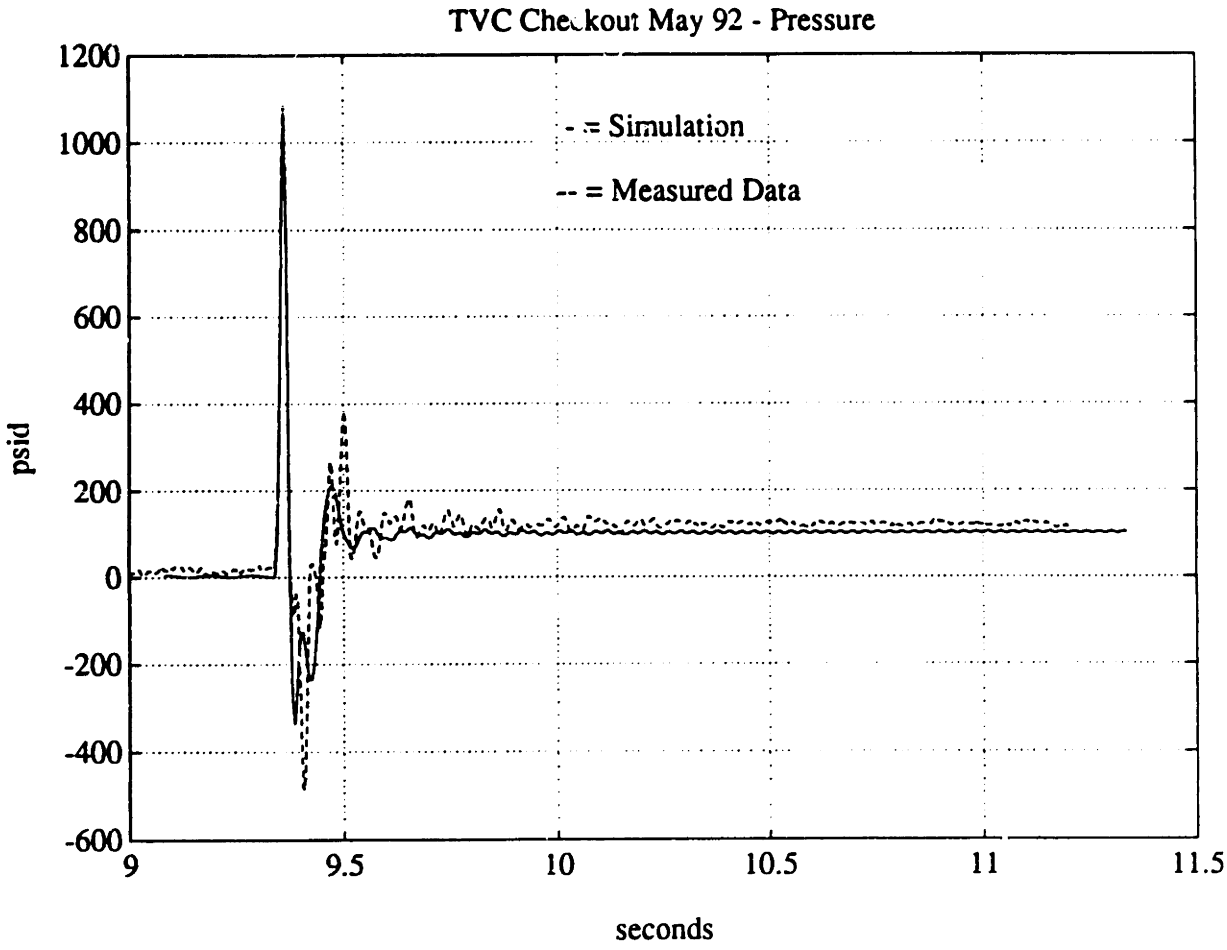

Figure 3-15: Comparison of Simulated [24] and Measured [46] Actuator Differential Pressure in Response to 0.3 Degree Step in the Rock Direction Using the FLCU

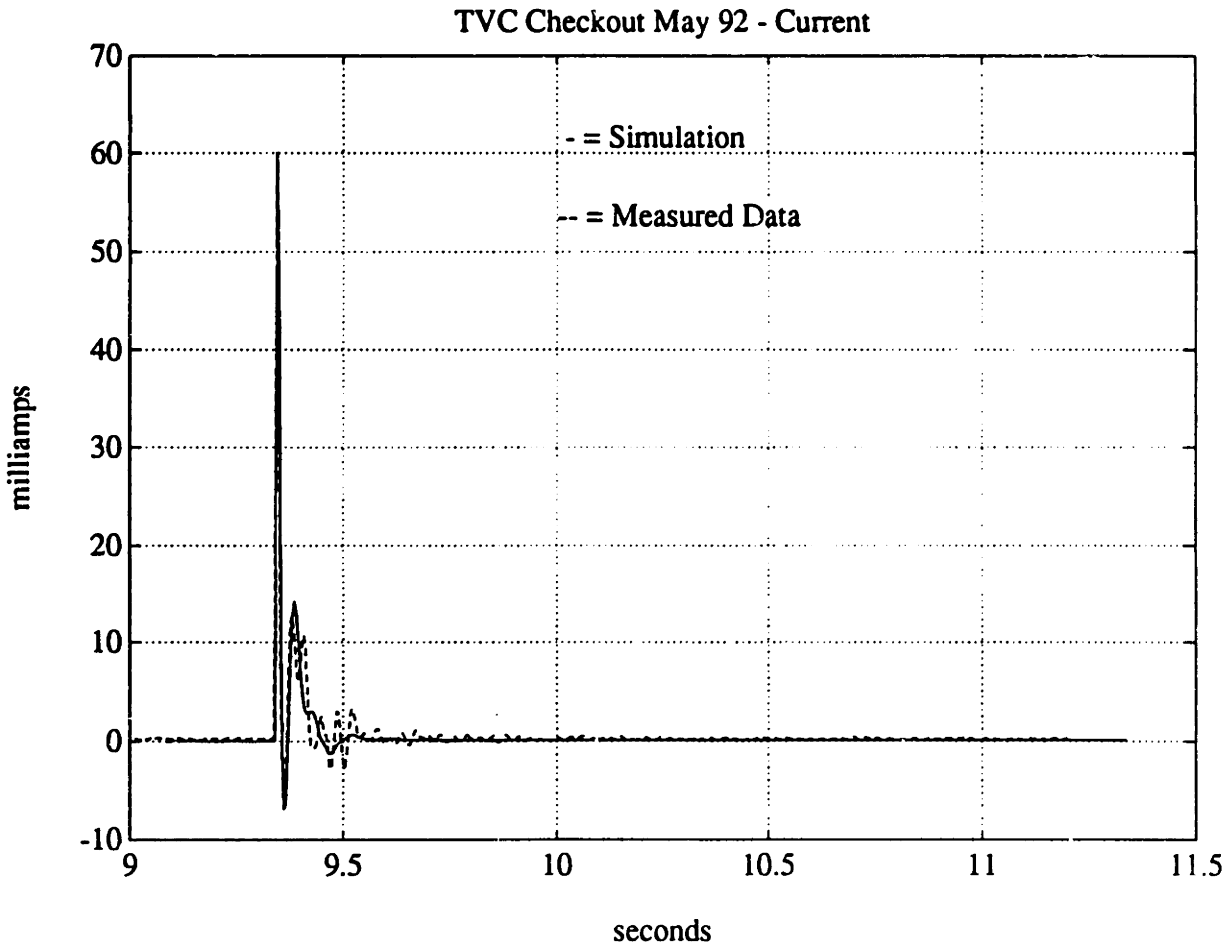

Figure 3-16: Comparison of Simulated [24] and Measured [46] Servovalve Current in Response to 0.3 Degree Step in the Rock Direction Using the FLCU

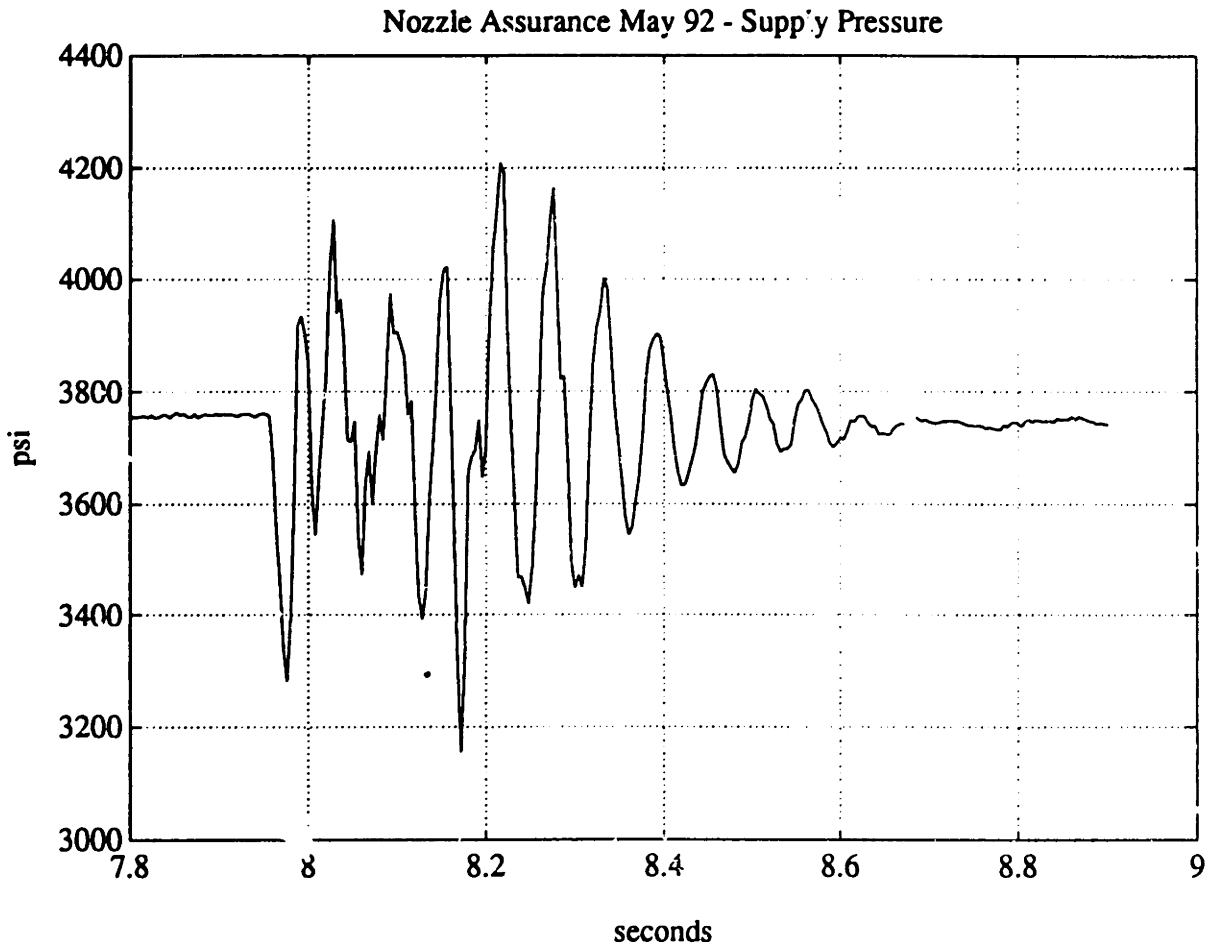

Figure 3-17: Measured Supply Pressure Variations in Response to 10 Hz, 0.36 Degree Sine Waves in the Rock Direction with the FLCU [46]

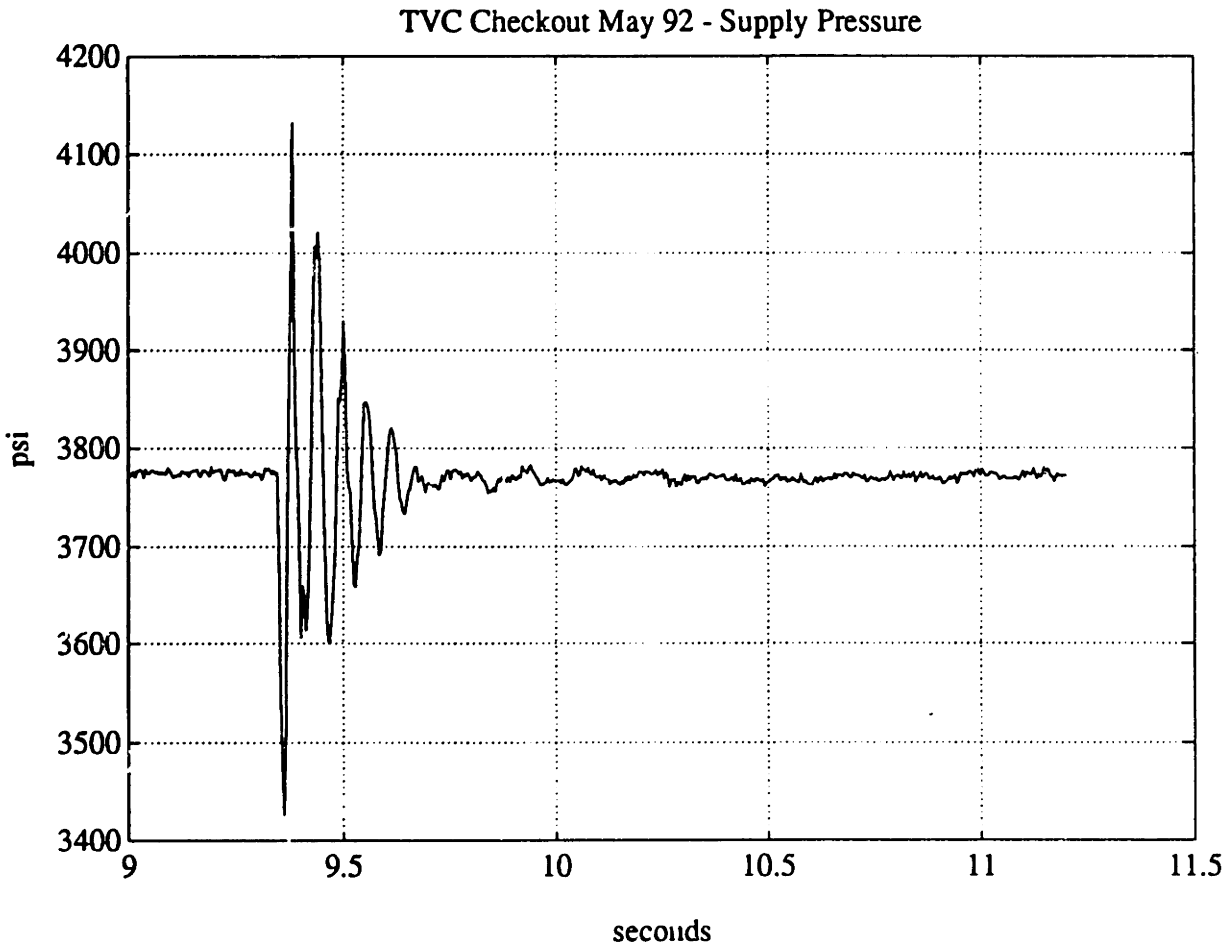

Figure 3-18: Measured Supply Pressure Variations in Response to 0.3 Degree Step in the Rock Direction with the FLCU [46]

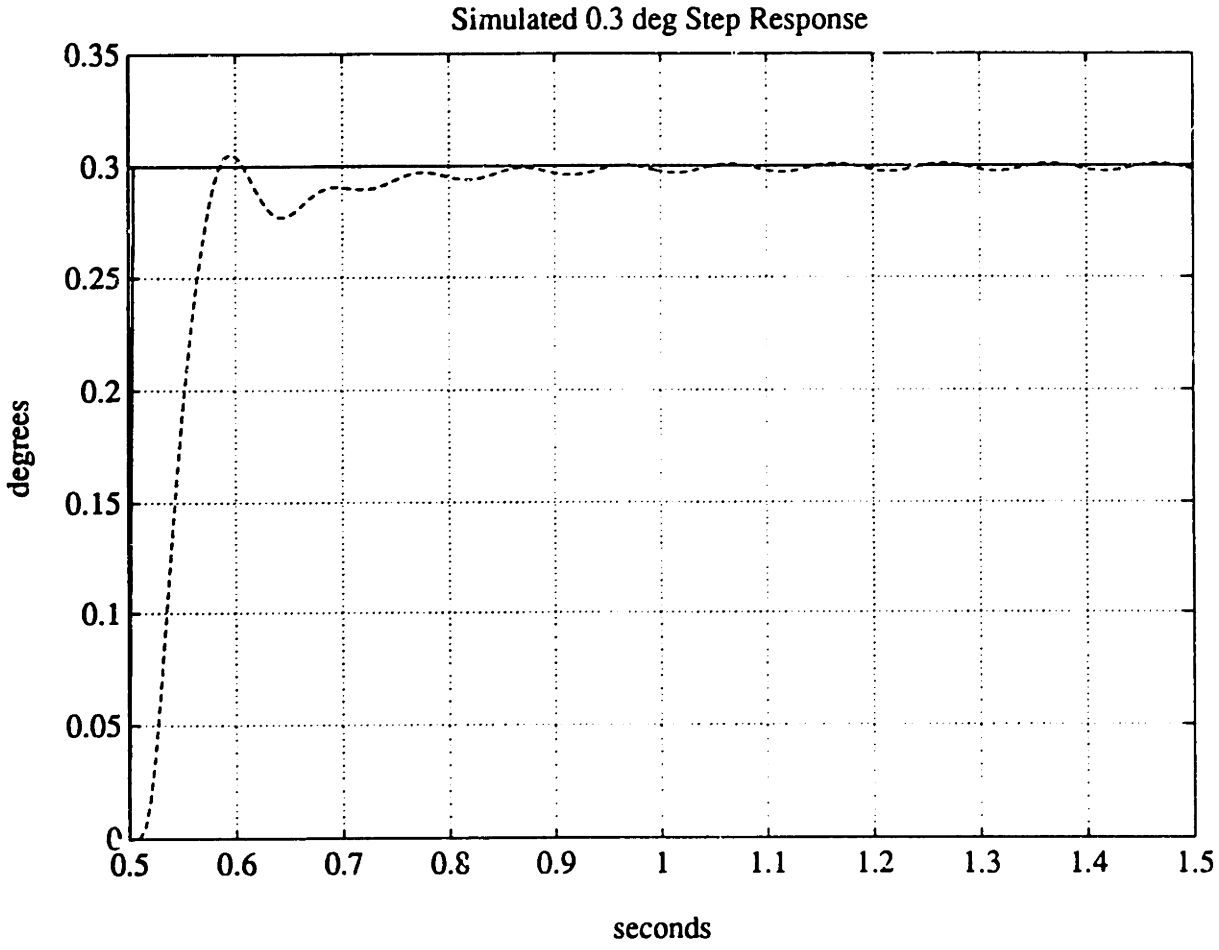

Figure 3-19: Simulated Nozzle Position Response to 0.3 Degree Step in the Rock Direction with FLCU

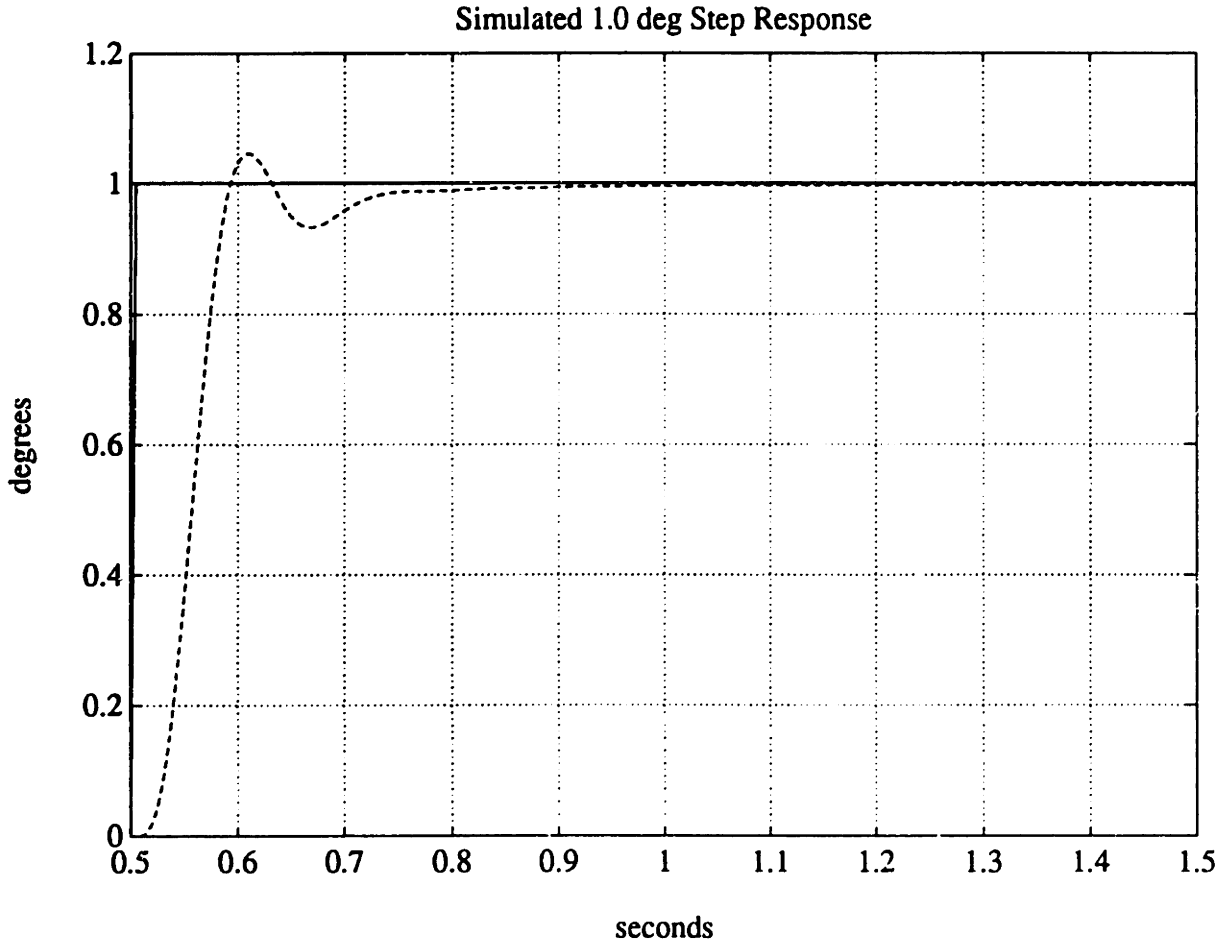

Figure 3-20: Simulated Nozzle Position Response to 1.0 Degree Step in the Rock Direction with FLCU

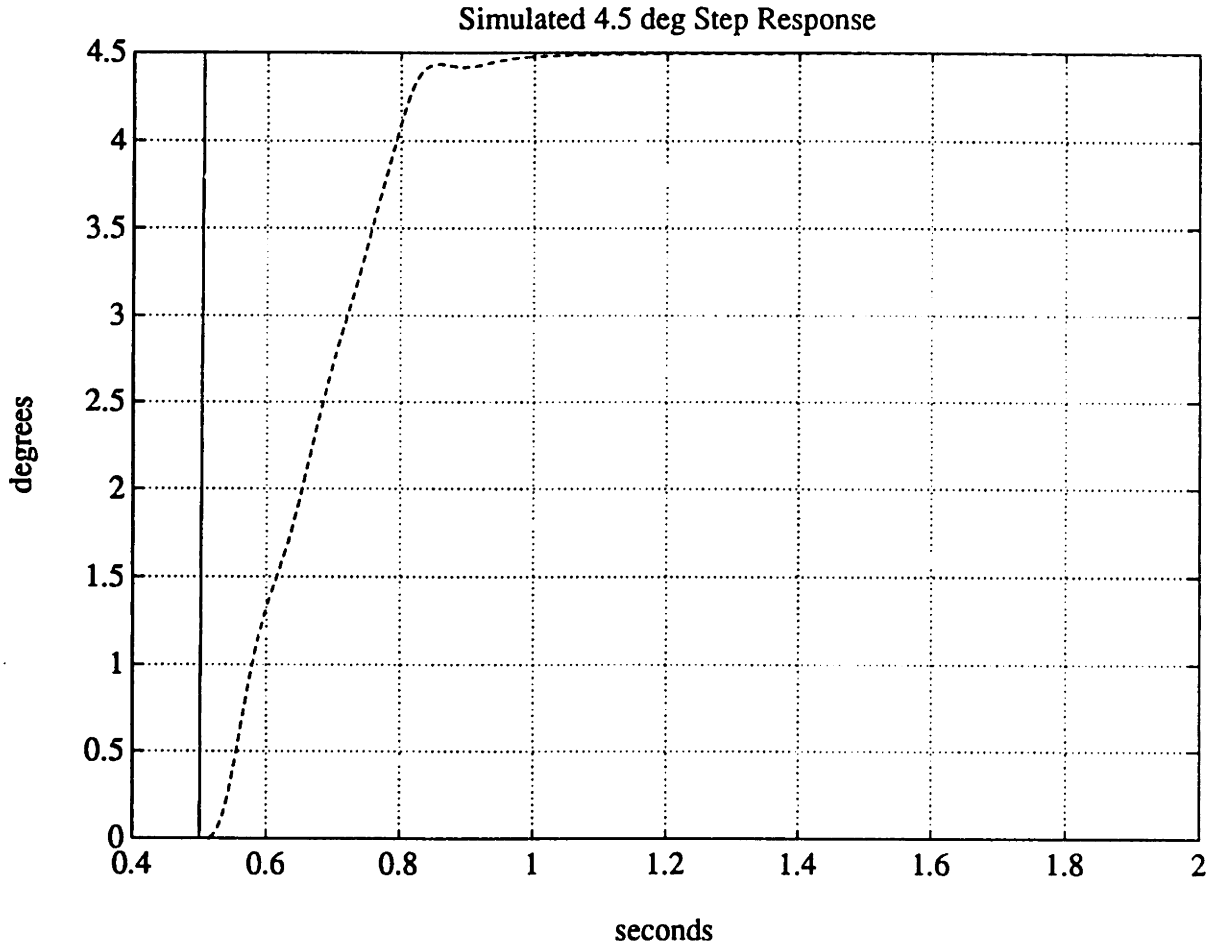

Figure 3-21: Simulated Nozzle Position Response to 4.5 Degree Step in the Rock Direction with FLCU

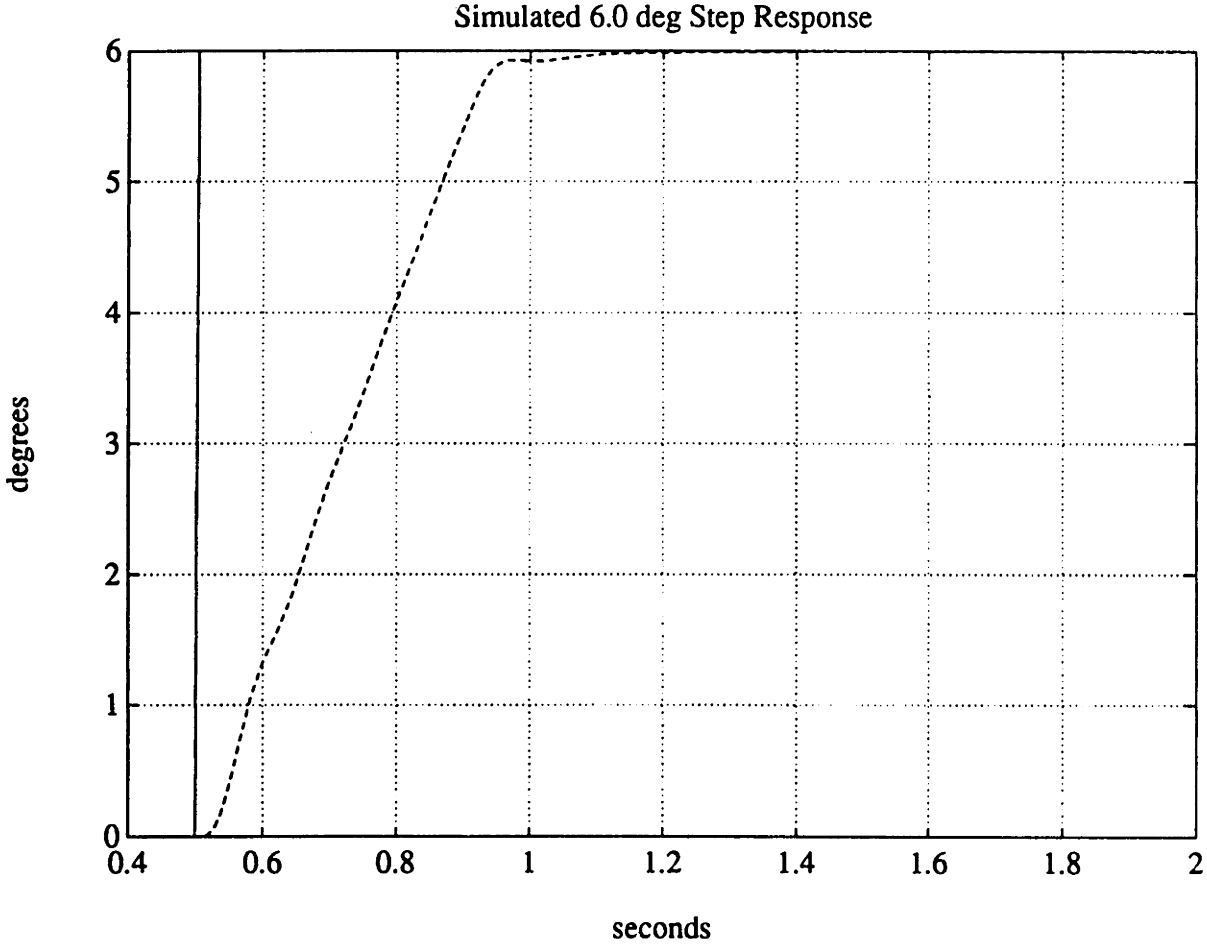

Figure 3-22: Simulated Nozzle Position Response to 6.0 Degree Step in the Rock Direction with FLCU

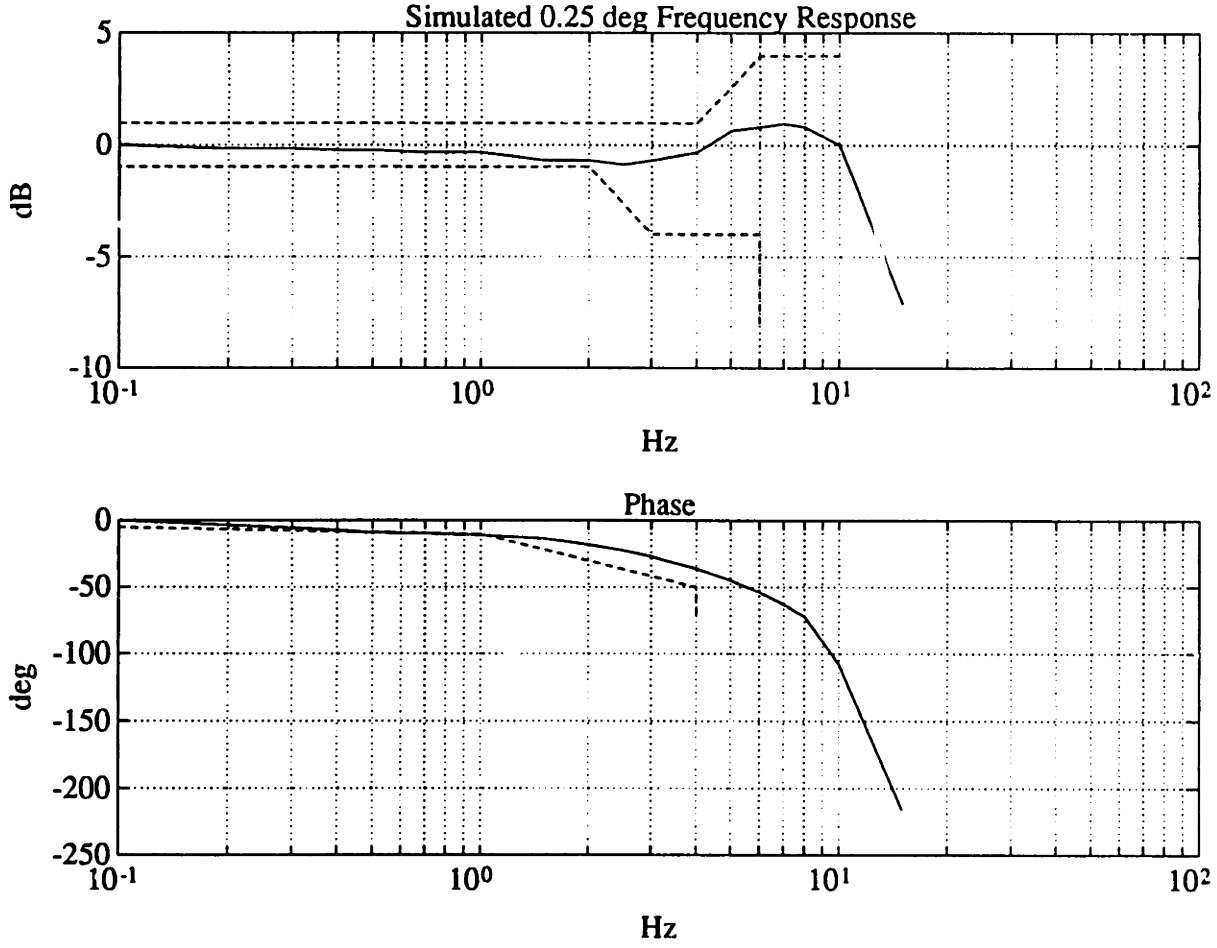

Figure 3-23: Simulated Frequency Response to 0.25 Degree Sinusoids for Closed Loop TVC System with FLCU

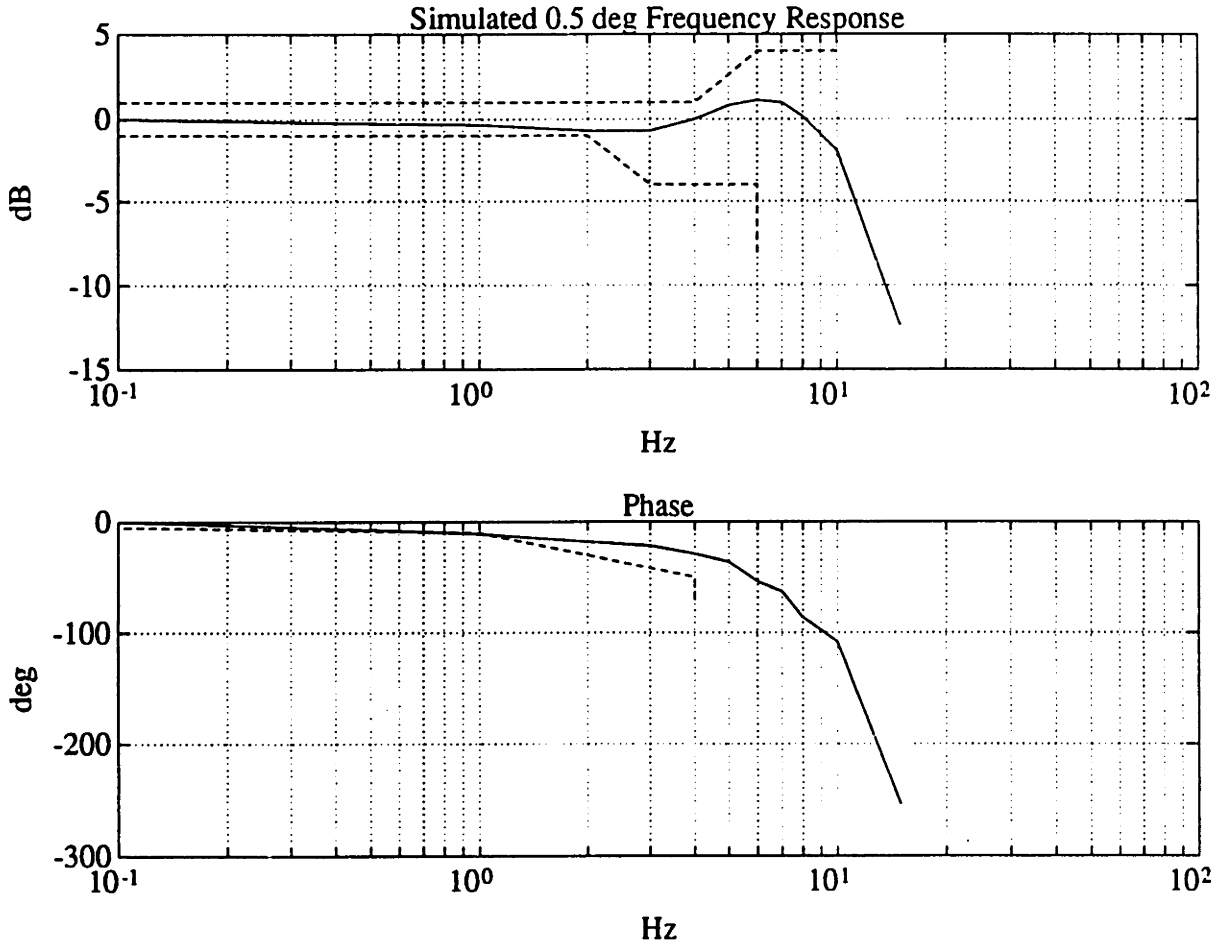

Figure 3-24: Simulated Frequency Response to 0.5 Degree Sinusoids for Closed Loop TVC System with FLCU

Chapter 4

Feedback Linearization

The design of a nonlinear controller for the TVC system using feedback linearization and pole placement techniques is outlined in this chapter. The nonlinear controller has the potential for offering improved performance at the cost of increased complexity. Results comparing the performance of the present classical controller and the author's nonlinear controller are presented.

Feedback linearization is a state-space model transformation technique which allows the design of linear controllers for nonlinear systems [37]. Implementation requires the availability of state measurements, and since the TVC system has only two types of transducers, nozzle position transducers and actuator pressure transducers, the rest of the state vector must be estimated using an observer. The technique also requires the plant to be *linear in control.* The system equations of such a plant, if it is single-input single-output, can be expressed in the following form, called *controllability canonical form:*

$$z_s^{(n)} = f(\underline{Z_s}) + b(\underline{Z_s})I_c \tag{4.1}$$

where:

$$\begin{aligned} I_c &= \text{Input} \\ \underline{Z_s} &= \text{State Vector } [z_s^{(n-1)} \cdots z_s]^T \\ z_s^{(n)} &= \text{nth Derivative of State of Interest} \end{aligned}$$

The goal of feedback linearization is to transform the system model into a simpler

form. Basically, for a controllability canonical system, the control problem can be reduced to that of controlling the linear system $z_s^{(n)} = v_s$ by implementation of the following control law:

$$I_c = \frac{v_s - f(\underline{Z_s})}{b(\underline{Z_s})} \tag{4.2}$$

when $b(\underline{Z_s}) \neq 0$. This, of course, assumes that $f(\underline{Z_s})$ and $b(\underline{Z_s})$ are known.

4.1 Nozzle Torques

For the sake of simplicity, the nozzle torques will be considered linear for the design of the nonlinear controller. The linear pole placement formulation also requires that the external torques have a linear form. Thus the assumptions made in Equations 3.1 and 3.2 are retained.

4.2 Pressure and Fluid Flow

The four forms of Equation 2.28 are restated as the following two equations:

$$Q_1 = F_1(P_1, P_2, P_s)x_{sy} \tag{4.3}$$

$$Q_2 = F_2(P_1, P_2, P_s)x_{sy} \tag{4.4}$$

And Equations 2.16 and 2.17 are rewritten:

$$\frac{dP_1}{dt} = G_1(P_1, P_2, dX_p) + E_1(X_p)Q_1 \tag{4.5}$$

$$\frac{dP_2}{dt} = G_2(P_1, P_2, dX_p) + E_2(X_p)Q_2 \tag{4.6}$$

Subtracting Equation 4.6 from Equation 4.5, and substituting Equations 4.3 and 4.4 yields a differential equation for P_L as a function of $(P_1, P_2, P_s, dX_p, X_p)$ and x_{sy}.

$$\frac{dP_L}{dt} = (G_1 - G_2) + (E_1F_1 - E_2F_2)x_{sy} \tag{4.7}$$

This equation is linear in the control input x_{sy}.

4.3 Supply Pressure

For simplicity, the supply pressure is assumed constant in the derivation of this non-linear controller. The assumption of Equation 3.18 is retained.

4.4 Servovalve

If the servovalve is sufficiently "fast" such that its dynamics can be neglected, then the Equation 4.7 is adequate for feedback linearization. It is then apparent from Equation 3.19 that only the following simple proportional relation needs to be substituted into Equation 4.7.

$$x_{sy} = 0.00148 \cdot I_c \tag{4.8}$$

If the servovalve is "slow" however, there are two choices. The first is to place a lead compensator before the servovalve, to increase high frequency gain, and continue to assume Equation 4.8 is a good enough approximation. This is relatively simple, but may not be sufficient if the servovalve is too slow. In the second method, Equation 4.7 can be differentiated twice to obtain an expression in $\ddot{x}_{sy}$.

$$\frac{d^3 P_L}{dt^3} = (\ddot{G}_1 - \ddot{G}_2) + (x_{sy}\frac{d^2}{dt^2} + 2\dot{x}_{sy}\frac{d}{dt} + \ddot{x}_{sy})(E_1 F_1 - E_2 F_2) \tag{4.9}$$

The servovalve transfer function (Equation 3.19) can then be restated as a second-order differential equation and subsituted into Equation 4.9 to give a description of the third derivative of load pressure which is still linear in control. Unfortunately, the equations for $\ddot{G}_1$ and $\ddot{G}_2$ become very complex. Thus the author chooses to use a first-order lead compensator before the servovalve with a zero at 500 rad/sec ($\approx$ 80 Hz) and a pole at 5000 rad/sec ($\approx$ 800 Hz). Since the servovalve response begins to drop off around the 50 Hz region (see Section 3.5, the lead compensator was designed to begin amplifying servovalve inputs at frequencies just above that region.

4.5 Nonlinear Controller

The TVC controller designed by the author has three major components, including the feedback linearization described above. State feedback of the nozzle angle and its first four derivatives is used to create a pole placement controller in conjunction with the feedback linearization. A reduced order observer is used to construct the feedback states and to calculate the feedback linearization parameters. A block diagram of the controller is shown in Figure 4-1.

The system is now only fifth order because the servovalve with lead compensation has been assumed to be sufficiently fast to be considered a zero-order gain in the system. The input to the system is now considered the derivative of load pressure.

$$\dot{X} = A_{plt2}X + B_{plt2}\frac{dP_L}{dt} \tag{4.10}$$

where:

$$X = \begin{bmatrix} \frac{d^4\theta}{dt} \\ w = \begin{bmatrix} \frac{d^3\theta}{dt} \\ \frac{d^2\theta}{dt} \\ \frac{d\theta}{dt} \end{bmatrix} \\ \theta \end{bmatrix} \tag{4.11}$$

$$A_{plt2} = \begin{bmatrix} A_{m1} & A_{m2} & 0 \\ A_{m3} & 0 & 0 \\ \begin{bmatrix} 0 & 0 & 0 \end{bmatrix} & 1 & 0 \end{bmatrix} \tag{4.12}$$

$$A_{m1} = \begin{bmatrix} \frac{-B_o}{J} & (\frac{-K_o - L^2K_c}{J} - \frac{K_c}{M_p}) & \frac{-K_cB_o}{JM_p} \\ 1 & 0 & 0 \\ 0 & 1 & 0 \end{bmatrix} \tag{4.13}$$

$$A_{m2} = \begin{bmatrix} \frac{-K_cK_o}{JM_p} \\ 0 \\ 0 \end{bmatrix} \tag{4.14}$$

$$A_{m3} = \begin{bmatrix} 0 & 0 & 1 \end{bmatrix} \tag{4.15}$$

$$B_{plt2} = \begin{bmatrix} B_{m1} \\ 0 \end{bmatrix} \tag{4.16}$$

$$B_{m1} = \begin{bmatrix} \frac{LK_eA_p}{JM_p} \\ 0 \\ 0 \end{bmatrix} \tag{4.17}$$

Note that A_{plt2} contains a column of zeros, indicating that a pure integrator is in the system. The system is still controllable in the sense that

$$[B_{plt2},\ A_{plt2}B_{plt2},\ A_{plt2}^2B_{plt2},\ \ldots,\ A_{plt2}^4B_{plt2}]$$

has rank 5 [30]. The reduced order observer requires only three states because nozzle angle and load pressures are directly measured. The design of the observer begins with the definition of a new state vector V:

$$V = w - E\theta \tag{4.18}$$

where E is yet to be specified. Therefore the reduced order plant model can be described as follows:

$$\dot{V} = (A_{m1} - EA_{m3})V + (A_{m1}E - EA_{m3}E + A_{m2})\theta + B_{m1}P_L \tag{4.19}$$

The observer is formed by merely copying this system.

$$\dot{Z} = (A_{m1} - EA_{m3})Z + (A_{m1}E - EA_{m3}E + A_{m2})\theta + B_{m1}P_L \tag{4.20}$$

Subtracting Equation 4.19 from Equation 4.20 yields the following:

$$\dot{Z} - \dot{V} = (A_{m1} - EA_{m3})(Z - V) \tag{4.21}$$

Thus the observer state Z will tend to track the plant state V at a rate determined by the eigenvalues of $(A_{m1} - EA_{m3})$. E is chosen by the author such that the observer poles are real and located at 200, 250, and 300 Hz.

The desired observer output, an estimate of $[d^4\theta, d^3\theta, d^2\theta, d\theta, \theta]^T$, is constructed from the observer state Z as follows. The hat symbol is used in the following text to distinguish the estimated system state from the actual system state. According to Equation 4.18:

$$\hat{w} = \begin{bmatrix} \widehat{d^3\theta} \\ \widehat{d^2\theta} \\ \widehat{d\theta} \end{bmatrix} = Z + E\theta \tag{4.22}$$

The only other state variable required from the observer is $\widehat{d^4\theta}$ because θ is a measurement. $\widehat{d^4\theta}$ is linearly related to the observer inputs P_L and θ, as well as $\hat{w}$. Thus, the coefficient matrices C_{obs} and D_{obs} can be constructed to create an estimate of the system state vector from the observer state Z.

$$\begin{bmatrix} \widehat{d^4\theta} \\ \widehat{d^3\theta} \\ \widehat{d^2\theta} \\ \widehat{d\theta} \\ \theta \end{bmatrix} = C_{obs}Z + D_{obs}\begin{bmatrix} P_L \\ \theta \end{bmatrix} \tag{4.23}$$

$$C_{obs} = \begin{bmatrix} A_{m1} \\ A_{m3} \\ \begin{bmatrix} 0 & 0 & 0 \end{bmatrix} \end{bmatrix} \tag{4.24}$$

$$D_{obs} = \begin{bmatrix} D_{obsm1} & D_{obsm2} \end{bmatrix} \tag{4.25}$$

$$D_{obsm1} = \begin{bmatrix} B_{m1} \\ 0 \\ 0 \end{bmatrix} \tag{4.26}$$

$$D_{obsm2} = \begin{bmatrix} A_{m2} \\ 0 \\ 1 \end{bmatrix} + \begin{bmatrix} A_{m1}F \\ A_{m3}E \\ 0 \end{bmatrix} \tag{4.27}$$

The feedback linearization requires estimates of the parameters P_1, P_2, P_s, dX_p, and X_p. P_1 and P_2 are assumed to be measured directly (although the present hardware configuration measures $P_1 - P_2$), and P_s is assumed constant. $\widehat{dX_p}$ and $\widehat{X_p}$ must be calculated from the observer output as follows:

$$\widehat{X_p} = \frac{J\widehat{d^2\theta} + B_o\widehat{d\theta} + (K_o + L^2K_e)\theta}{LK_e} \tag{4.28}$$

$$\widehat{dX_p} = \frac{J\widehat{d^3\theta} + B_o\widehat{d^2\theta} + (K_o + L^2K_e)d\theta}{LK_e} \tag{4.29}$$

With the feedback linearization and the observer design complete, the final step is to implement the pole placement controller using the output of the observer. The system matrices A_{plt2} and B_{plt2} are defined in Equations 4.12 through 4.17. The input dP_L/dt is set equal to some linear combination C_{place} of the observer output $\hat{X}$ which tracks the actual state X.

$$\dot{X} \approx (A_{plt2} + B_{plt2}C_{place}).X \tag{4.30}$$

Thus the proper choice of C_{place} allows one to place the poles of the closed loop system arbitrarily. The author has chosen a pair of poles at 10 Hz with a damping ratio of 0.707, and the other three poles are real and located at 100, 200, and 500 Hz.

4.6 Nonlinear Controller Performance

Figures 4-2 through 4-5 compare the simulated performance of the feedback linearized pole placement controller with the classical FLCU controller. Shown are simulated nozzle position responses to steps of 0.3, 1.0, 4.5, and 6.0 degrees. The nonlinear hydraulic equations of Chapter 2 were used, including the limited flow capacity of the HPU. As Figures 4-2 and 4-3 show, the feedback linearized controller achieves the desired nozzle position for small angle deflections with greater speed and less overshoot. It is a more efficient nozzle positioning controller. However, for the larger angles, as shown in Figures 4-4 and 4-5, there is a small steady state error, even though the nozzle still reaches its final position with greater speed. The additional stiffness K_{fdg} used to approximate the increased flexseal stiffness at small nozzle angles in Equation 3.1 is no longer valid for the large nozzle angles. Thus the observer does a poor job estimating the state of the system. The steady state error is easily removed by adjusting K_{fdg}, as is also shown in Figures 4-4 and 4-5.

The solution to the problem of small steady state errors for large nozzle angles might be an adaptive controller which can automatically adjust K_{fdg}. Since the TVC system is linear in control, it is conceivable that an adaptation law can be constructed as described in [37]. Nevertheless, the nonlinear controller as described above is more efficient in reaching its final state than is the classical controller. And the steady state error is within the ± 0.23 degree requirement.

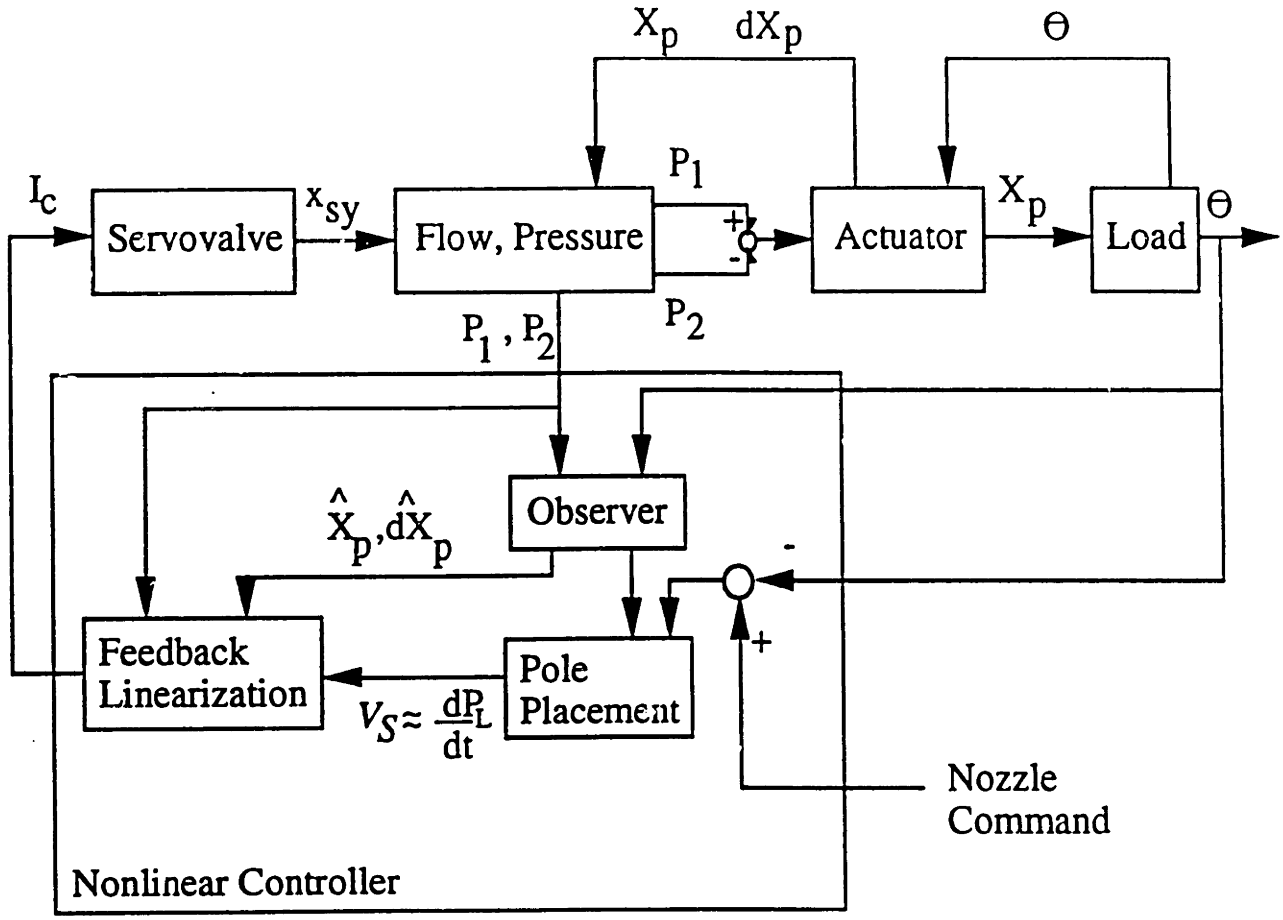

Figure 4-1: Block Diagram of TVC System with Feedback Linearized Pole Placement Controller

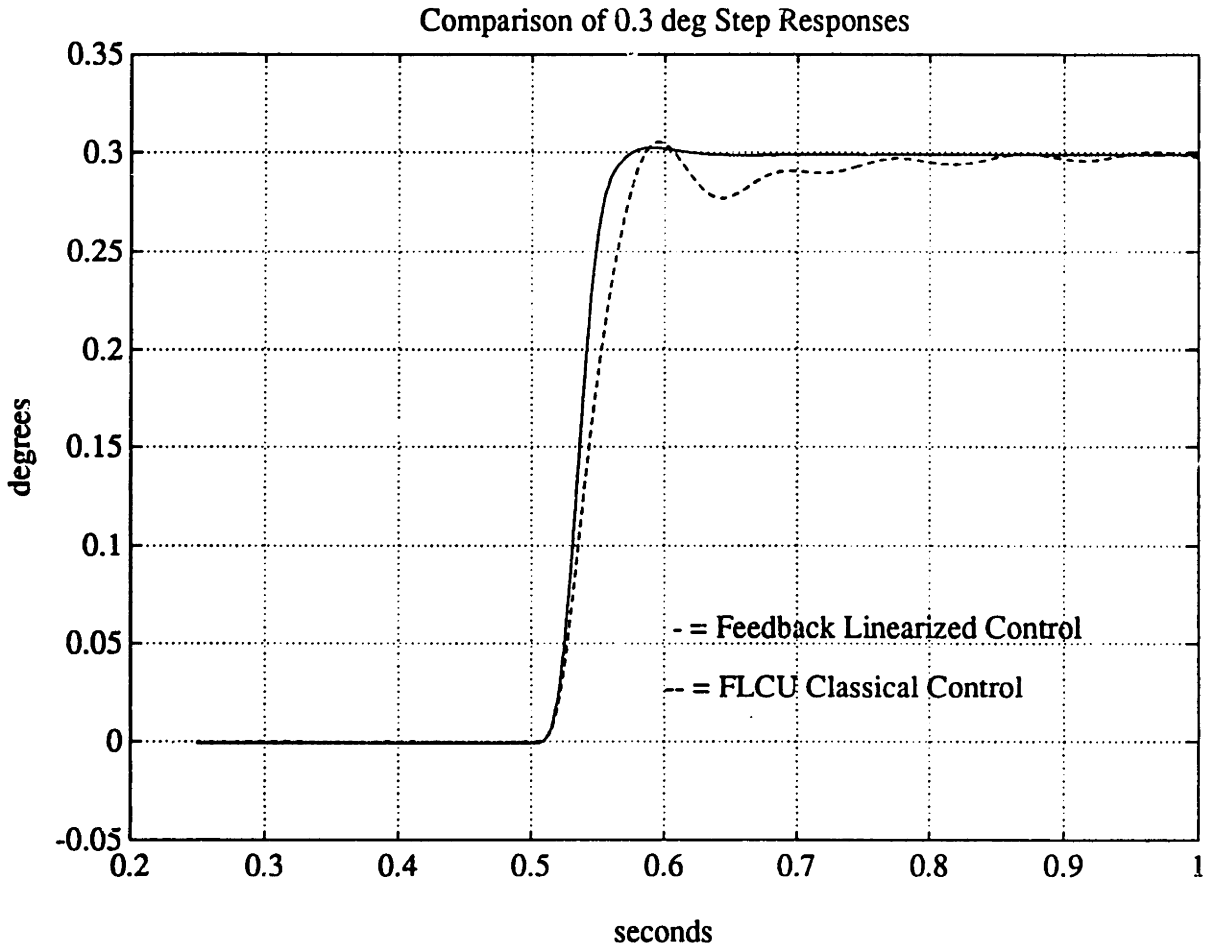

Figure 4-2: Comparison of Simulated Nozzle Position in Response to 0.3 Degree Step Using Feedback Linearized Controller and FLCU Classical Controller

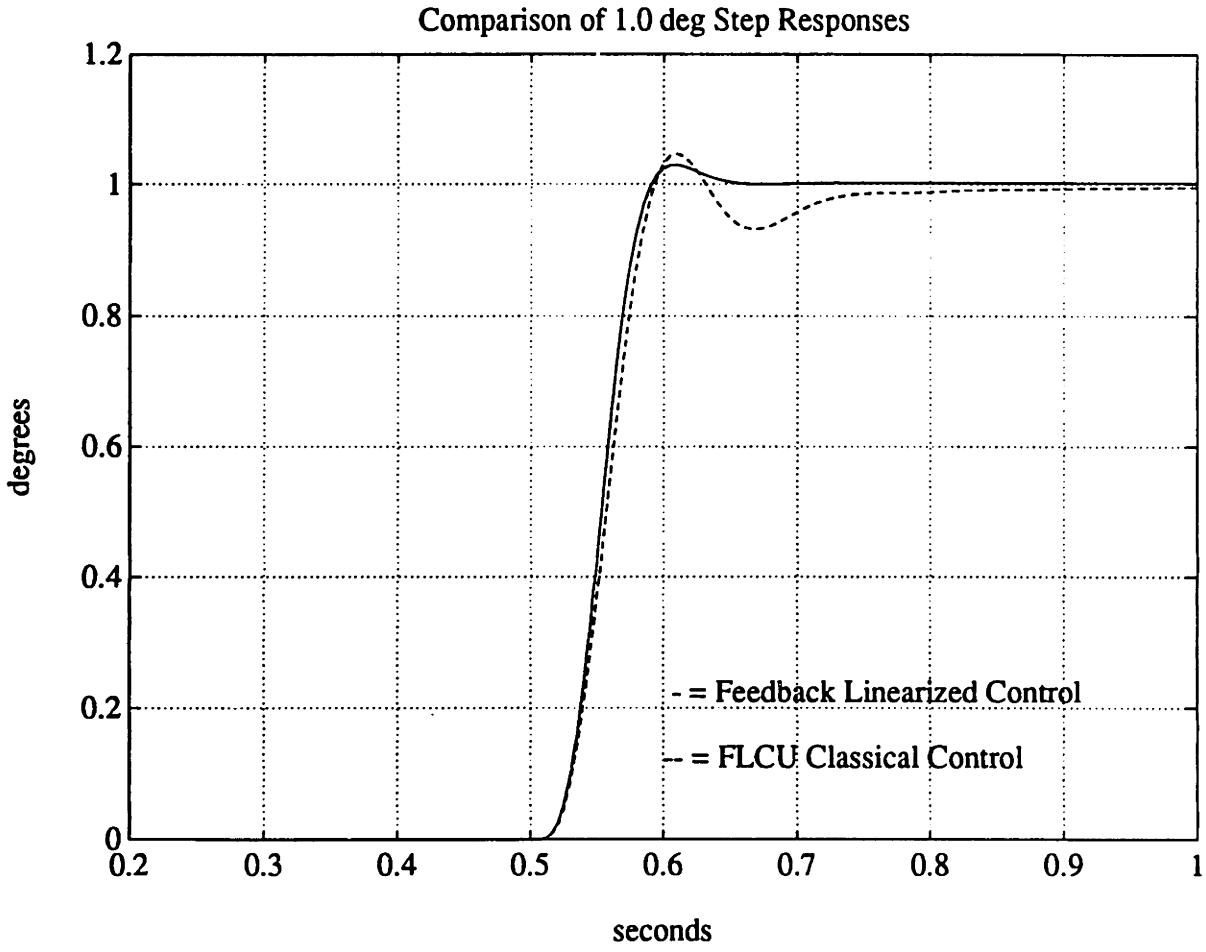

Figure 4-3: Comparison of Simulated Nozzle Position in Response to 1.0 Degree Step Using Feedback Linearized Controller and FLCU Classical Controller

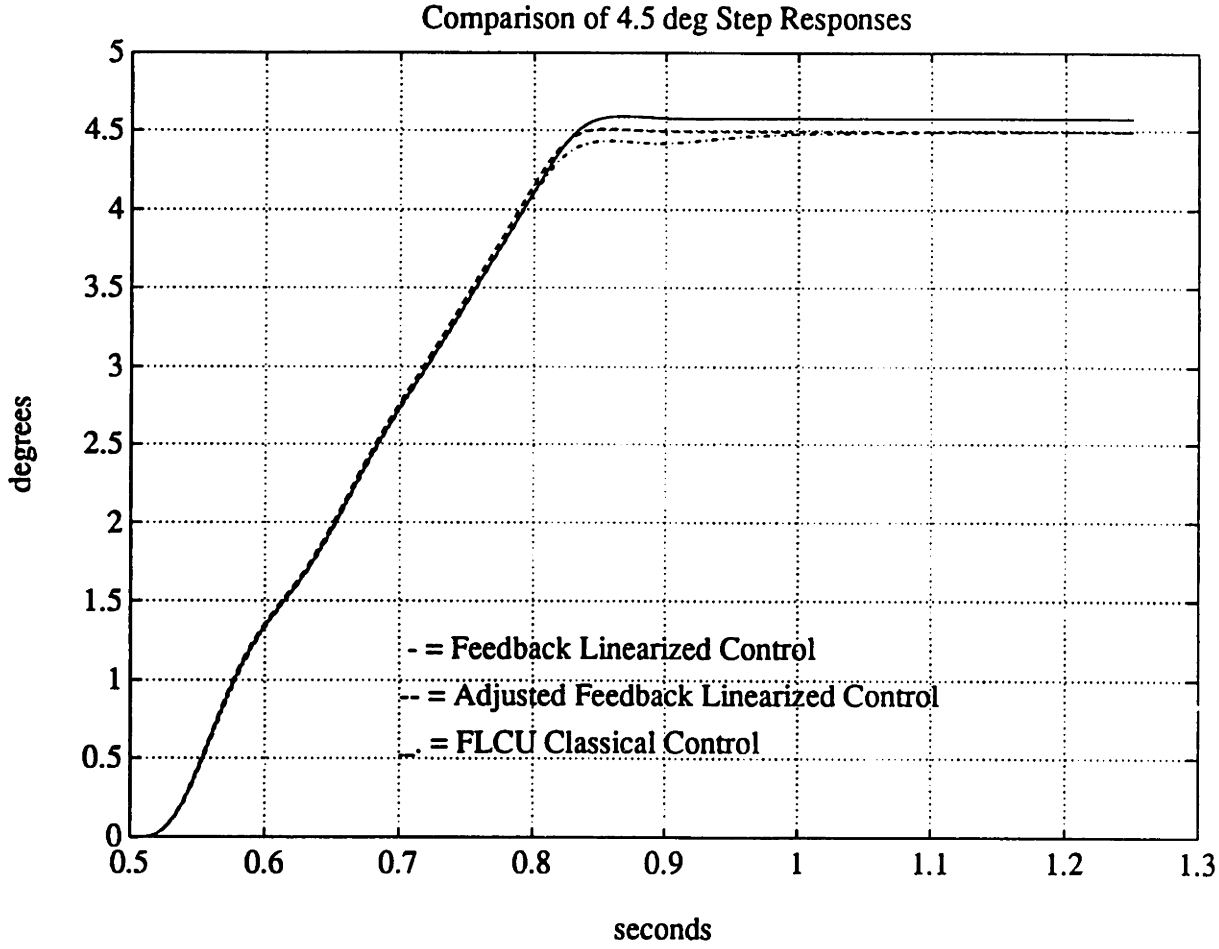

Figure 4-4: Comparison of Simulated Nozzle Position in Response to 4.5 Degree Step Using Feedback Linearized Controller and FLCU Classical Controller.

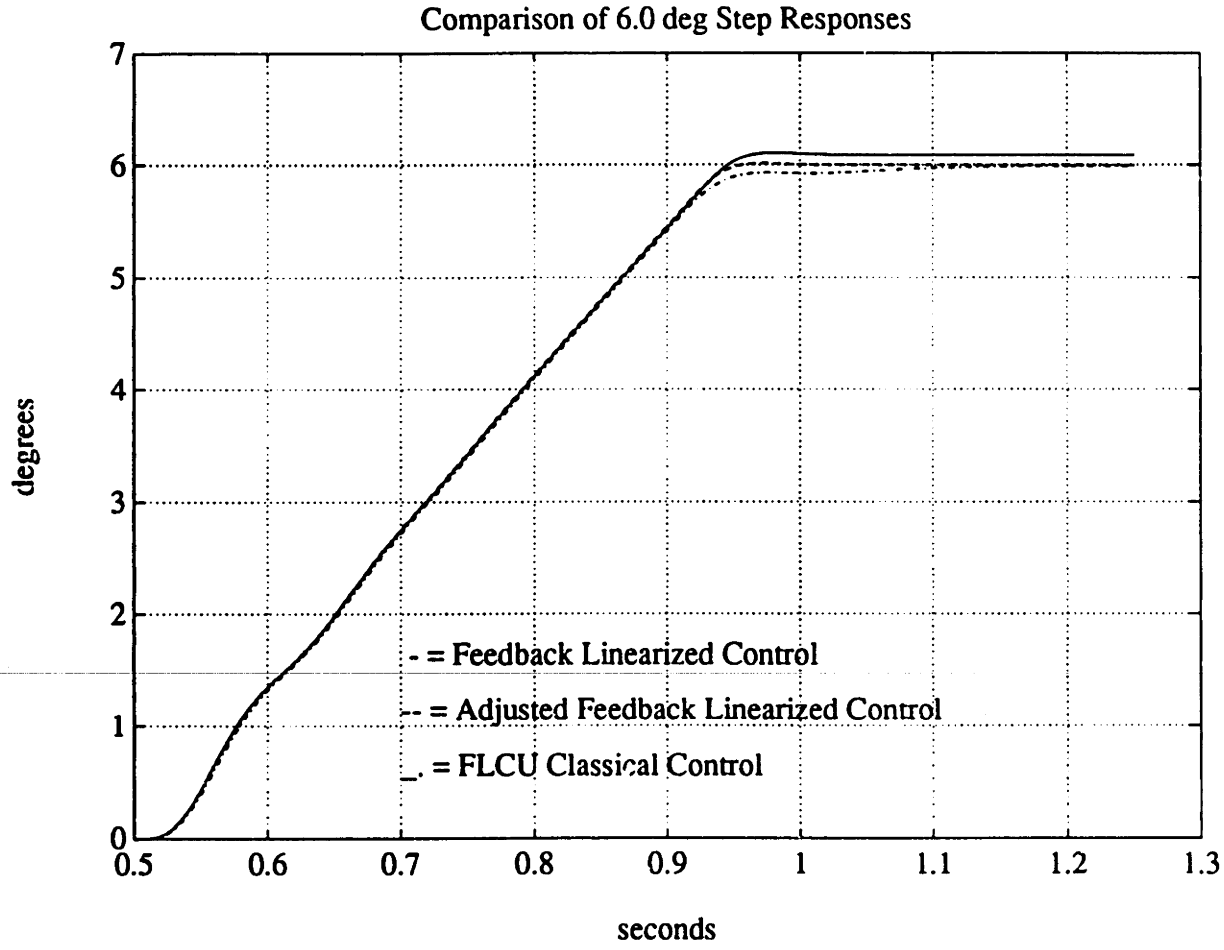

Figure 4-5: Comparison of Simulated Nozzle Position in Response to 6.0 Degree Step Using Feedback Linearized Controller and FLCU Classical Controller.

Chapter 5

Conclusion

As an excercise in the modeling and design of an electrohydraulic rocket TVC system, this thesis demonstrates the following results. (1) The nonlinear hydraulic equations developed in Chapter 2 describe the performance of the overall TVC system quite well. It is suspected that structural bending characteristics of the nozzle need to be included in the model in order to match some of the higher frequency components of the measured data. (2) The linearization of the hydraulic model presented in Chapter 3 does not describe the performance of the overall TVC system well. In particular, while the frequency response of the closed-loop nonlinear system rolls off sharply after 10 Hz, the closed-loop linear system remains close to 0 dB, resulting in approximately 7 Hz more bandwidth. Still, the analysis showed that the linearization is a useful design tool for compensation for the TVC system. This compensation, however, cannot be optimal because it is based upon a loose model. (3) The feedback linearization and pole placement methods used in Chapter 4 can successfully mitigate the controller design problems associated with the traditional methods of Chapter 3. The nonlinear controller developed in this thesis performs more efficiently than the TVC system's present classical controller. The steady state accuracy of the nonlinear controller could be improved, but it does perform within specification limits.

Appendix A

Titan IV SRMU TVC Parameters

This appendix lists parameter values for the Titan IV SRMU TVC system [45, 44, 9]. English units are used.

cis	=	Cubic Inches Per Second
deg	=	Degrees
ft	=	Foot
in	=	Inches
ma	=	Milliamperes
lbs	=	Pounds
psi	=	Pounds Per Square Inch
sec	=	Seconds

A.1 Nozzle Torques

$$\sigma = 198{,}000 \text{ in} \cdot \text{lbs} \cdot \text{sec/deg}$$

$$K_s = 147{,}000 \text{ in} \cdot \text{lbs/deg}$$

Unpressurized, Maximum

$$= 309{,}000 \text{ in} \cdot \text{lbs/deg}$$

Unpressurized, Minimum

$$= 261{,}000 \text{ in} \cdot \text{lbs/deg}$$

Pressurized, Maximum

$$= 195{,}000 \text{ in} \cdot \text{lbs/deg}$$

Pressurized, Nominal

$$= 128{,}000 \text{ in} \cdot \text{lbs/deg}$$

Pressurized, Minimum

$$T_c = 202{,}000 \text{ in} \cdot \text{lbs}$$

$$J = 193{,}000 \text{ in} \cdot \text{lbs} \cdot \text{sec}^2$$

$$K_1 = 500{,}000 \text{ lbs/in}$$

$$K_3 = 2{,}690{,}000 \text{ lbs/in}$$

$$K_4 = 3{,}085{,}000 \text{ lbs/in}$$

$$L = 53.82 \text{ in, average}$$

A.2 Piston and Flow

β_e = 112,840 psi at 350 Fahrenheit

A_p = 24.6 in^2

AE = 0.983

B_{fa} = 60 lbs · sec/deg

C_{em} = 0 cis/psi

C_{im} = 0.000695 cis/psi

CO = 73.9 in/sec · $\sqrt{psi}$

F_{ca} = 4 lbs

FQ = 1

M_p = 0.5208 slug · ft/in

RF = 0.0028 psi/cis^2

WS = 1.569 in

XTS = 13.358 in

A.3 Servovalve

τ = 0.0025 sec

A_1 = 0.3068 in^2

K_{v1} = 590 ma/in

K_q = 0.04 cis/ma

NTM = 3;

Q_{sl} = 0.475 cis

Q_{st} = 0.004 cis

Q_{xo} = 10.68 cis/in

XSL = 0.063 in

Bibliography

[1] Karl J. Åström and Björn Wittenmark. *Computer Controlled Systems: Theory and Design.* Prentice-Hall Information and System Sciences Series. Prentice-Hall, Inc., 1984.

[2] Unknown Author. LCU System Interim Design. Facsimile Transmittal, Hercules Missiles, Ordnance and Space Group Bacchus Works, Magna, UT, March 7 1991. to R. A. Thelander, The Aerospace Corp., El Segundo, CA.

[3] Edward Beltrami. *Mathematics for Dynamic Modeling.* Academic Press, Inc., 1987.

[4] G. H. Bergman, B. V. See, and E. T. Hikida. Titan IV PQM-1' Solid Rocket Motor Upgrade Full Scale Static Firing. Twenty Four Hour Report SR-T05-003-2, Hercules Missiles, Ordnance and Space Group Bacchus Works, Magna, UT, June 13 1992.

[5] R. J. Bywater. An End Effects Model for SRMU Flow Separation Nozzle Side Forces. Aerospace Technical Memorandum 92(2530-03)-31. The Aerospace Corporation, El Segundo, CA, June 19 1992. to Morgan W. Tam.

[6] P. R. Dahl. Solid Friction Damping of Spacecraft Oscillations. In *AIAA Guidance and Control Conference*, Boston, MA, August 20-22 1975. American Institute of Aeronautics and Astronautics. AIAA Paper No. 75-1104.

[7] John J. Dazzo and Constantine H. Houpis. *Linear Control System Analysis and Design: Conventional and Modern.* McGraw-Hill Book Company, third edition, 1988.

[8] The Deflector Jet Servovalve. Technical Bulletin 121, Moog Inc., East Aurora, NY.

[9] K. J. Dickerson. Titan IV SRMU Thrust Vector Control . Delta Preliminary Design Review, Hercules Aerospace Bacchus Works, Magna, UT, October 3 1989. Volume I.

[10] K. J. Dickerson. Titan IV SRMU Thrust Vector Control . Delta Preliminary Design Review, Hercules Aerospace Bacchus Works, Magna, UT, October 4 1989. Volume II.

[11] Joseph A. Dworak. *Digital Control of the Hydraulic Actuators of an Adaptive Suspension Vehicle.* PhD thesis, Ohio State University, 1985.

[12] Joseph A. Dworak and Jackson H. Jung. Modeling and Control Analysis of the Electrohydraulic Thrust Vector Control System for the Solid Rocket Motor Upgrade. The Aerospace Corporation, Vehicle and Control Systems Division, Internal Review Briefing, October 28, 1990.

[13] R. Ewel. Design Analysis Report for Thrust Vector Control System for Titan IV Solid Rocket Motor Upgrade. Technical Report MR E-5394, Moog Inc., Aerospace Group, Missile Systems Division, East Aurora, NY, February 28 1990.

[14] Philip M. Gerhart and Richard J. Gross. *Fundamentals of Fluid Mechanics.* Addison-Wesley Publishing Co., 1985.

[15] L. H. Geyer. Controlled Damping Through Dynamic Pressure Feedback. Technical Bulletin 101, Moog Inc., Controls Division, East Aurora, NY, April 1972.

[16] Organization M760 Test Operations Group. Titan IV Static Firing of PQM-1. Specific Test Plan DRD SR-T05, Hercules Missiles, Ordnance and Space Group Bacchus Works, Magna, UT, September 7 1990.

[17] Walter L. Johnstun. PQM-1' Nozzle Properties. Request for Information ITRR-4-8, Hercules Missiles, Ordnance and Space Group Bacchus Works, Magna, UT,

September 14 1990. from R. A. Thelander, The Aerospace Corp., El Segundo, CA.

[18] Jackson H. Jung. Titan IV SRMU Thrust Vector Control Simulation. The Aerospace Corporation, Vehicle and Control Systems Division, Internal Review Briefing, July 14, 1992.

[19] Jackson H. Jung. Contractor's Titan IV SRMU TVC Modeling and Simulation. Interoffice Correspondence A92-5414.JHJ.02, The Aerospace Corporation, El Segundo, CA, November 5 1991. to Roger. A. Thelander.

[20] Jackson H. Jung. Comparisons of Aerospace TVC Simulation and PQM-1 Pathfinder Data. Interoffice Correspondence A92-5414.JHJ.05, The Aerospace Corporation, El Segundo, CA, February 28 1992. to Roger. A. Thelander.

[21] Jackson H. Jung. Development of TVC Actuator Forces from Excitement at 8.0 Hz. Interoffice Correspondence A92-5414.JHJ.06, The Aerospace Corporation, El Segundo, CA, February 28 1992. to Wayne. H. Goodman.

[22] Jackson H. Jung. Status of Titan IV SRMU TVC Modeling Efforts. Interoffice Correspondence A92-5414.JHJ.04, The Aerospace Corporation, El Segundo, CA, January 16 1992. to Roger. A. Thelander.

[23] Jackson H. Jung and Joseph A. Dworak. Effect of Internal Aerotorque Transient on Titan IV SRMU TVC. Interoffice Correspondence A92-5414.JHJ.01, The Aerospace Corporation, El Segundo, CA, October 24 1991. to Roger. A. Thelander.

[24] Jackson H. Jung and Joseph A. Dworak. Comparisons Between Aeropsace Simulation and Nozzle Assurance Test. Interoffice Correspondence A92-5414.JHJ.08, The Aerospace Corporation, El Segundo, CA, July 7 1992. to Roger. A. Thelander.

[25] Thomas Kailath. *Linear Systems.* Prentice-Hall Information and System Sciences Series. Prentice-Hall, Inc., 1980.

[26] E. C. Kyed. EHPU Pressure vs. Flow Characteristics. Request for Information ITRR-3-4, Hercules Missiles, Ordnance and Space Group Bacchus Works, Magna, UT, July 27 1990. from R. A. Thelander, The Aerospace Corp., El Segundo, CA.

[27] E. C. Kyed. Phase III TVC Checkouts. Hardcopy Data Package, Hercules Missiles, Ordnance and Space Group Bacchus Works, Magna, UT, September 5 1990. Pathfinder Tests for PQM-1 at Edwards Air Force Base, CA.

[28] G. L. Laughlin. Thrust Vector Control System. Critical Item Development Specification S283003 Rev. F. Part 1., Hercules Aerospace Bacchus Works, Magna, UT, May 1990.

[29] J. E. Lodman. Heat Shield Induced Nozzle Vectoring Loads. Interoffice Memo, Hercules Aerospace Bacchus Works, Magna, UT, February 4 1992. to Mark A. Anderson.

[30] David G. Luenberger. *Introduction to Dynamic Systems: Theory, Models, and Applications.* John Wiley and Sons, 1979.

[31] Frank S. Mango. Booster/Nozzle Flexibility Effects on SRMU TVC Stability. Martin Marietta Space Launch Systems, Titan IV Flight Controls Briefing, September 15, 1992.

[32] D. McCloy and H. R. Martin. *Control of Fluid Power: Analysis and Design.* Ellis Horwood Ltd., 2nd edition, 1980.

[33] Herbert E. Merritt. *Hydraulic Control Systems.* John Wiley and Sons, 1967.

[34] James K. Roberge. *Operational Amplifiers: Theory and Practice.* John Wiley and Sons, 1975.

[35] Michael K. Sain, Joseph L. Peczkowski, and James L. Melsa. *Alternatives for Multivariable Control.* National Engineering Consortium, 1978.

[36] William McC. Siebert. *Circuits, Signals, and Systems.* The MIT Press, 1986.

[37] Jean-Jacques E. Slotine and Weiping Li. *Applied Nonlinear Control.* Prentice-Hall, Inc., 1991.

[38] T. J. Staniewicz. Titan IV Nozzle Flexseal SN TFS-002 (For PQM-1). Acceptance Test Report DRD SR-T01-010, Hercules Missiles, Ordnance and Space Group Bacchus Works, Magna, UT, August 10 1992.

[39] Gilbert Strang. *Linear Algebra and Its Applications.* Academic Press, Inc., second edition, 1980.

[40] Roger A. Thelander. Titan Flexseal Review, October 25 1989. Notes from Technical Meeting.

[41] Taco J. Viersma. *Analysis, Synthesis, and Design of Hydraulic Servosystems and Pipelines*, volume 1 of *Studies in Mechanical Engineering.* Elsevier Scientific Publishing Co., 1980.

[42] C. Wang. Titan IV SRMU Hinge Moment Budget. Aerospace Technical Memorandum 91(6530-11)-20, The Aerospace Corporation, El Segundo, CA, February 19 1991. to M. K. Fukuda.

[43] Robert Winn. Contract Number F04701-85-C-0019, PQM-1 Pathfinder Performance Test Data. Sun SPARC Station Digital Computer Tape SLS-91-40353, Martin Marietta Space Launch Systems, Denver, CO, January 21 1991. to Joseph A. Dworak, The Aerospace Corp., El Segundo, CA.

[44] Robert Winn. PQM-1 Data. Facsimile Transmittal, Martin Marietta Astronautics Group, Denver, CO, February 26 1991. to R. A. Thelander, The Aerospace Corp. El Segundo, CA.

[45] Robert Winn. Update to IFS-TIV-16001; TVC Model Update. Facsimile Transmittal, Martin Marietta Astonautics Group, Denver Colorado, October 3 1991. to Roger. A. Thelander, The Aerospace Corp., El Segundo, CA.

[46] Robert Winn. Contract Number F04701-85-C-0019, Flight Controls Data Transmittal of SRMU PQM-1' TVC Checkout Quick Look Data. IBM Personal Computer Compatible Data Disk SLS-92-41938, Martin Marietta Space Launch Systems, Denver, CO, June 1 1992. to Joseph A. Dworak, The Aerospace Corp., El Segundo, CA.

[47] J. Zaborszky and H. J. Harrington. A Describing Function for Multiple Nonlinearities Present in Electrohydraulic Control Valves. *Trans. AIEE Pt.I*, 76:183–198, 1957.

[48] Advanced Continuous Simulation Language, Mitchell and Gauthier Associates, 73 Junction Square Dr. Concord, MA 07142-3096.

[49] MATRIX-X, Integrated Systems Inc. 2500 Mission College Blvd. Santa Clara, CA 95954-1215.

[50] Matlab, The MathWorks, Inc., 21 Eliot St. South Natick, MA 01760.